



UNIVERSITAT POLITÈCNICA  
DE CATALUNYA  
BARCELONATECH

## *Nanophotonic antennas for enhanced single-molecule fluorescence detection and nanospectroscopy in living cell membranes*

**Raju Regmi**

**ADVERTIMENT** La consulta d'aquesta tesi queda condicionada a l'acceptació de les següents condicions d'ús: La difusió d'aquesta tesi per mitjà del repositori institucional UPCommons (<http://upcommons.upc.edu/tesis>) i el repositori cooperatiu TDX (<http://www.tdx.cat/>) ha estat autoritzada pels titulars dels drets de propietat intel·lectual **únicament per a usos privats** emmarcats en activitats d'investigació i docència. No s'autoritza la seva reproducció amb finalitats de lucre ni la seva difusió i posada a disposició des d'un lloc aliè al servei UPCommons o TDX. No s'autoritza la presentació del seu contingut en una finestra o marc aliè a UPCommons (*framing*). Aquesta reserva de drets afecta tant al resum de presentació de la tesi com als seus continguts. En la utilització o cita de parts de la tesi és obligat indicar el nom de la persona autora.

**ADVERTENCIA** La consulta de esta tesis queda condicionada a la aceptación de las siguientes condiciones de uso: La difusión de esta tesis por medio del repositorio institucional UPCommons (<http://upcommons.upc.edu/tesis>) y el repositorio cooperativo TDR (<http://www.tdx.cat/?locale-attribute=es>) ha sido autorizada por los titulares de los derechos de propiedad intelectual **únicamente para usos privados enmarcados** en actividades de investigación y docencia. No se autoriza su reproducción con finalidades de lucro ni su difusión y puesta a disposición desde un sitio ajeno al servicio UPCommons. No se autoriza la presentación de su contenido en una ventana o marco ajeno a UPCommons (*framing*). Esta reserva de derechos afecta tanto al resumen de presentación de la tesis como a sus contenidos. En la utilización o cita de partes de la tesis es obligado indicar el nombre de la persona autora.

**WARNING** On having consulted this thesis you're accepting the following use conditions: Spreading this thesis by the institutional repository UPCommons (<http://upcommons.upc.edu/tesis>) and the cooperative repository TDX (<http://www.tdx.cat/?locale-attribute=en>) has been authorized by the titular of the intellectual property rights **only for private uses** placed in investigation and teaching activities. Reproduction with lucrative aims is not authorized neither its spreading nor availability from a site foreign to the UPCommons service. Introducing its content in a window or frame foreign to the UPCommons service is not authorized (*framing*). These rights affect to the presentation summary of the thesis as well as to its contents. In the using or citation of parts of the thesis it's obliged to indicate the name of the author.



Nanophotonic antennas for enhanced  
single-molecule fluorescence detection and  
nanospectroscopy in living cell membranes

RAJU REGMI

under the supervision of

JÉRÔME WENGER

and

MARÍA F. GARCÍA-PARAJO

submitted this thesis in partial fulfillment  
of the requirements for the degree of

DOCTOR

by

Aix-Marseille Université, France

and

Universitat Politècnica de Catalunya, Espagne

October 2017



UNIVERSITAT POLITÈCNICA  
DE CATALUNYA  
BARCELONATECH

## Chapter 5

# Surface nanogaps for giant fluorescence enhancement

The use of nanoantennas for biological applications, such as dynamic sensing and molecular spectroscopy in plasma membranes of cells require large-scale availability of narrow accessible gaps. Not only should the nanogaps with sub 20 nm dimensions be reproducibly fabricated, but also the gap region (electromagnetic hotspot) must remain accessible to the target molecules. In this chapter, we introduce the concept of surface nanogaps achieved with a new nanofabrication technique that applies planarization, etch back and template stripping to expose the excitation hotspot at the top surface of the nanostructure. We will then discuss the optical performance of these “planar nanoantennas” for enhanced single-molecule fluorescence detection and demonstrate their superior performance over conventional electron beam lithography methods.

This project was carried out in collaboration with the teams of Prof. Jürgen Brugger (EFPL, Switzerland) and Prof. Niek F. van Hulst (Molecular Nanophotonics, ICFO, Barcelona).

### 5.1 Nanoantennas with surface nanogaps: Motivation

Optical nanoantenna can efficiently confine light energy into nanoscale dimensions breaching the classical diffraction limit. This leads to enhanced light-matter interactions at

---

The contents of this chapter have been published in:

V. Flauraud, **R. Regmi**, P. Winkler, D. T. L. Alexander, H. Rigneault, N. F. van Hust, M. F. García-Parajó, J. Wenger & J. Brugger, “*In-plane plasmonic antenna arrays with surface nanogaps for giant fluorescence enhancement*,” **Nano Letters**, 17 (3), 1703-1710 (2017).

the nanoscale, and thus making nanoantenna a powerful tool for investigating single-molecule dynamics that requires both high spatial and temporal resolution [10, 11]. However, in most nanoantenna designs, the region of maximum field localization and enhancement (*i.e.*, electromagnetic hotspot) is not readily accessible to the sample since it is buried in the nanostructure. For example, solution based single-molecule measurements at biologically-relevant high micromolar concentrations and investigation nanoscale membrane architecture in plasma membranes of living cells, requires large availability of narrow gaps with the smallest gap region (hotspot) at the top of the nanostructure. Exposing the narrowest region of the gap towards the sample proximity ensures that probe molecules experience only the “brighter side” of the nanoantenna while simultaneously providing a near flat substrate favored for live-cell research. Despite impressive recent progress using electron beam [144], focused ion beam [145] or stencil lithographies [146, 147], the challenges of reliable narrow gap fabrication and hotspot accessibility remain major hurdles limiting the impact and performance of optical nanoantennas.

As the current large-scale fabrication techniques lack reproducible geometrical control below 20 nm, limiting the applicability of these efficient platforms for bio-inspired applications, we propose a new nanofabrication technique that applies planarization, etch back and template stripping resulting a large scale production of surface nanogaps (normally at the bottom, now at the top of the structure). We demonstrate large scale arrays of planar nanoantennas (fabricated at EPFL, Switzerland), featuring gaps as small as 10 nm with sharp edges and full surface accessibility of the confined hotspot region for enhanced single-molecule fluorescence detection. The novel fabrication approach drastically improves the optical performance of plasmonic nanoantennas to yield giant fluorescence enhancement factors, together with zeptoliter range detection volumes. This fabrication method achieves excellent geometric control in the nanometer range over large areas, and is fully adaptable to different antenna designs providing direct access to the enhanced field at the gap region. As we will demonstrate, this fabrication approach will significantly improve the effectiveness of plasmonic antennas for various applications, including ultra-sensitive biosensing and live cell research.

In the next section, we will detail on how the current limitations in fabrication accuracy (specially for gaps smaller than 20 nm) and scalability can be addressed using planarization, etch back and template stripping. The burst analysis, FCS and TCSPC measurements will be then discussed in detail to demonstrate the superior performance over conventional electron beam lithography methods. After the discussions on the optical performance of these in-plane nanoantennas at very high fluorophore concentrations

for enhanced single-molecule fluorescence detection, in the next Chapter 6, we will exploit the extreme planarity of these structure to investigate the dynamics of membrane lipids in living cells.

## 5.2 Large scale in-plane nanoantennas: Fabrication

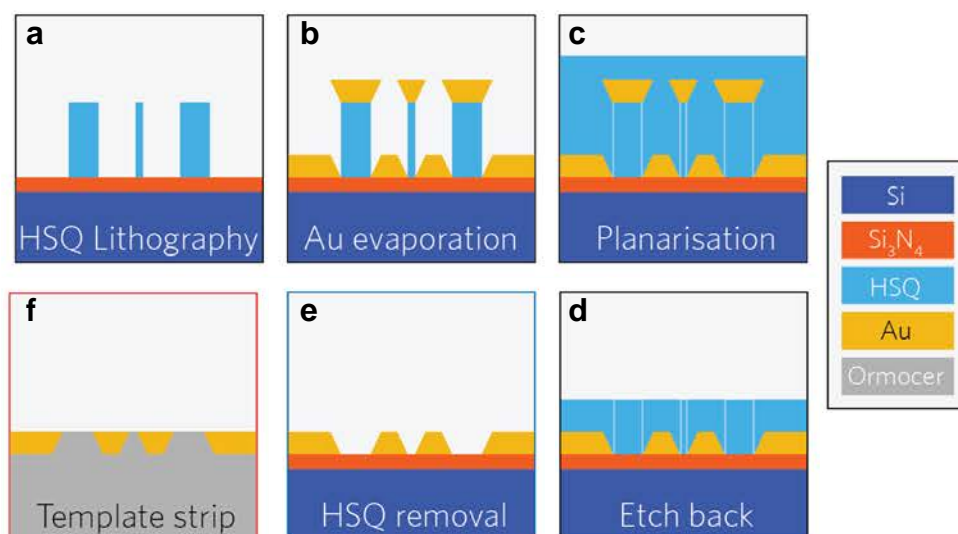
The antenna design is based on the “antenna-in-box” platform featuring a nanogap dimer antenna inside a rectangular box aperture. The central nanogap antenna between two 80 nm gold half-spheres creates the hotspot for fluorescence experiments and the cladding  $300 \times 140 \text{ nm}^2$  box, essentially screens the background signal by preventing direct excitation of molecules diffusing away from the hotspot [89, 148]. This design is tailored for optimal enhanced single molecule analysis in solutions at high  $\mu\text{M}$  concentrations.

Figure 5.1 summarizes the different steps of the nanofabrication procedure. The nanoantenna fabrication is performed on a 100 nm-thick silicon nitride deposited over silicon wafers (100 mm diameter, prime grade). Negative tone hydrogen-silsesquioxane (HSQ) resist is spun at 1500 rpm for 240 seconds yielding an approximately 100 nm-thick coating. The samples are then exposed by electron-beam lithography using a 1 nm grid and a 2 nA beam (5 nm FWHM) (a). After exposure, the samples are developed at room temperature in 25% tetramethylammonium hydroxide for 2 minutes, rinsed in deionized water and isopropanol prior to drying in order to avoid any possible collapse of the narrowest features induced by capillary force. A 50 nm-thick gold film is then evaporated ( $10 \text{ \AA/s}$ ) by electron beam heating at a pressure of  $8 \times 10^{-7} \text{ mBar}$  on static substrates (b). The stage temperature is maintained at  $-50^\circ \text{ C}$  to reduce the gold grain size by approximately a factor of two as compared to room temperature evaporation, allowing for low edge roughness and improved shape accuracy.

Planarization is then carried out by spinning flowable oxide (Dow Corning FOX-16) at 1000 rpm for 240 seconds (c). This yields 1  $\mu\text{m}$  thick film with a residual topography above the structures of interest below 10 nm. Broad argon ion beam milling (Veeco Nexus IBE350) is then performed at  $-45^\circ$  sample tilt to etch back the flowable oxide until the top gold caps were fully removed (d). End point detection is performed by monitoring the signal from gold on a secondary ion mass spectrometer. A 30 s etch with hydrofluoric acid diluted 1:10 in deionized water is then used to clear out the residual HSQ in the antenna apertures (e). The 100 mm silicon wafer is then cleaved into individual dies each of which contains nanoantennas with various gap sizes.

---

*Nanofabrication procedure was performed by Dr. Valentin Flauraud (EPFL, Switzerland) at the Center of Micro/ Nanotechnology (CMI) of EPFL, Switzerland.*



**FIGURE 5.1: Fabrication of planar nanoantenna arrays.** The nanoantenna fabrication process flow is performed over a silicon nitride layer deposited in silicon thin-film. The HSQ resist is patterned by electron-beam lithography (a) followed by a 50 nm thick gold layer evaporation (b). Flowable oxide is then spun for planarization (c) which is then etched back by Ar ion beam (d) to remove the top metal capping. Wet etching of the remaining HSQ (e) clears out the antenna geometry and then finally template stripping is done using UV curable adhesive (f).

As sketched in Figure 5.1e, the gold sidewalls bear a tapering angle due to metal diffusion during the evaporation. Therefore the narrowest gap region lies at the bottom of the structure close to the substrate interface. This hotspot position is impractical for biosensing and fluorescence enhancement applications, where the narrowest gap position should be on the top surface of the structure in order to maximize the contact with the probe solution. Thus the template stripping approach is implemented by using UV curable adhesive (f) in which the gold structures are transferred, and flipped over, onto a microscope coverslip to facilitate access to the narrowest and brightest region of the nanogap.

For template stripping procedure, a 150  $\mu\text{m}$  thick microscope coverslip (30 mm diameter) is cleaned in piranha solution and then surface activated by oxygen plasma treatment (Tepla Gigabatch 1000 W, 500 SCCM  $\text{O}_2$ ). The plasma exposed surface of the coverslip is then brought in contact with the gold substrates in silicon wafer dice with a drop of UV curable OrmoComp (microresist technology GMBH) and is cross-linked under UV and light pressure (ESCO EUN-4200 375 nm, 2.5  $\text{mW}/\text{cm}^2$ ) for 3 minutes followed by separation of the glass from the silicon with a razor blade. It is important to note that the last template stripping step can be performed just before the final fluorescence measurements, so the antenna hotspot is protected from surface contaminants during long term storage.

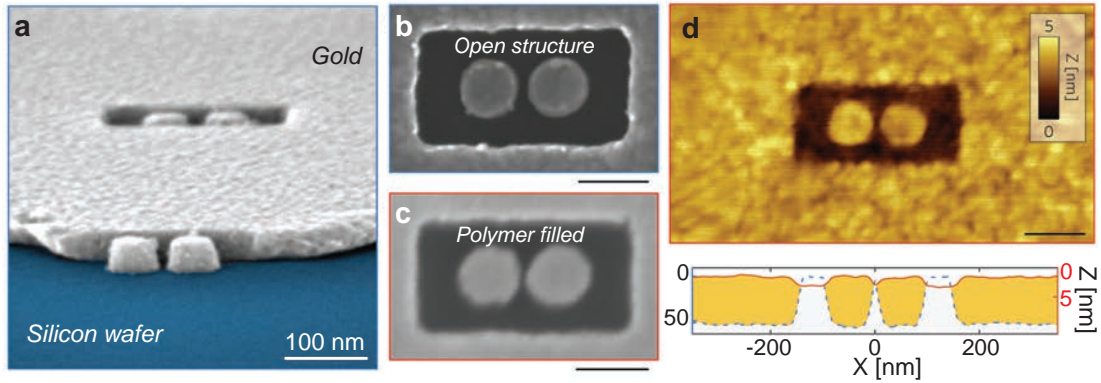


**FIGURE 5.2: SEM and AFM images of planar “antenna-in-box” devices.** (a) Tilted SEM view of an opened “antenna-in-box” before template stripping. The smallest part of the gap ( $\sim 12$  nm in this case) lies at the surface level. A similar structure is imaged from the top before (b) and after (c) template stripping. Dimensions are preserved and the space surrounding the antenna is filled by the UV curable polymer as seen in the AFM image (d) and shows less than 5 nm residual topography. Lower panel in d shows two AFM profiles averaged over 20 line scans before (dashed blue) and after (red) template stripping of the 50 nm-thick gold structure. All scale bars are 100 nm.

Figure 5.2a shows the tilted SEM view of an open antenna-in-box before template stripping (as sketched in Figure 5.1e). The smallest part of the gap, here 12 nm, lies at the surface level, closer to the silicon wafer interface. A similar structure is imaged from the top before (b) and after (c) template stripping. This comparison before and after template stripping, clearly shows that the narrowest gap region emerges on a flat top surface enabling maximum fluorescence enhancement in a minimal near-field probe volume. Figure 5.2d is a representative AFM image of the template-stripped nanoantenna showing less than 5 nm residual topography. These AFM analysis further confirm that the dimensions are preserved after template stripping procedure and the space surrounding the nanoantenna is filled by the UV curable polymer (see lower panel in Figure 5.2d). As all these fabrication processes are performed on conductive silicon substrates, the final structures can be easily transferred to microscope coverslips, avoiding the need for a supplementary adhesion layer that can damp the plasmonic performance [149].

Moreover, we use transmission electron microscopy (TEM) to accurately quantify the dispersion in the nanoantenna dimensions and to test the accuracy of the production process. The same fabrication process, excluding template stripping, is carried out on a 30 nm thick silicon nitride membranes for accurate TEM metrology on prototypical arrays of nanoantennas. Figure 5.3a shows a representative image of a  $5 \times 5$  antenna array with 10 nm nominal gap width used for metrology purposes with no template stripping performed. Various gap separations (from 10 nm to 45 nm) are achieved with narrow dispersion and the results are summarized in Figure 5.3b,c. It should be noted that

although the resist HSQ is patterned at dimensions in the range of 5 nm for the central nanogap region, the effective gap separation of the gold dimer appears systematically larger. This effect is due to a combination of metal diffusion and aperture clogging during evaporation, as well as metal wetting and diffusion onto the substrate.

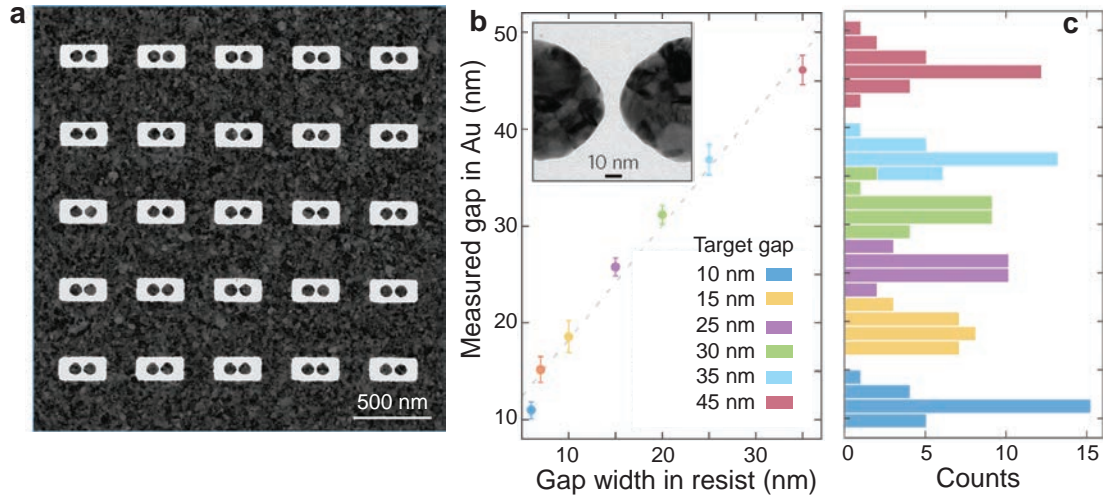


**FIGURE 5.3: TEM metrology and nominal gap size.** (a) TEM image of a  $5 \times 5$  antenna array with a 10 nm nominal gap width used for metrology purposes with no template stripping performed. The scale bar is 500 nm. The rectangular apertures have  $300 \times 140 \text{ nm}^2$  dimensions with each nanosphere being 80 nm in diameter. (b) Measured gap width of the Au dimers as a function of HSQ structure design width. Average gap width and associated standard deviation error bars are displayed. (c) Corresponding distribution histogram with 1.5 nm bin width. The gap size variations are due to the finite grain size in the Au film.

### 5.3 Near field enhancement and nanoantenna resonance

We perform numerical modeling based on FDTD method using Rsoft Fullwave 6.0 software for nanoantenna with 10 nm (Figure 5.4a-c) and 30 nm (Figure 5.4d-f) gap sizes and access excitation intensity enhancement at 633 nm with polarization along the dimer axis. The computation considers the mesh size of 0.5 nm for 10 nm gap antenna and 1 nm for 30 nm gap antenna and uses 214 temporal steps of  $8.1 \times 10^{-19}$  s. The permittivity of gold is modeled according to the data in Ref. [150].

The intensity recorded at the antenna surface for 10 nm gap (a) shows excitation intensity enhancement up to  $600\times$ , while a 30 nm gap antenna yields nearly  $160\times$  near field enhancement (d). We perform a series of such modeling to study the evolution of the peak intensity enhancement as a function of the antenna nanogap separation (g), and then estimate the detection volume for each case (h). The estimation of the detection

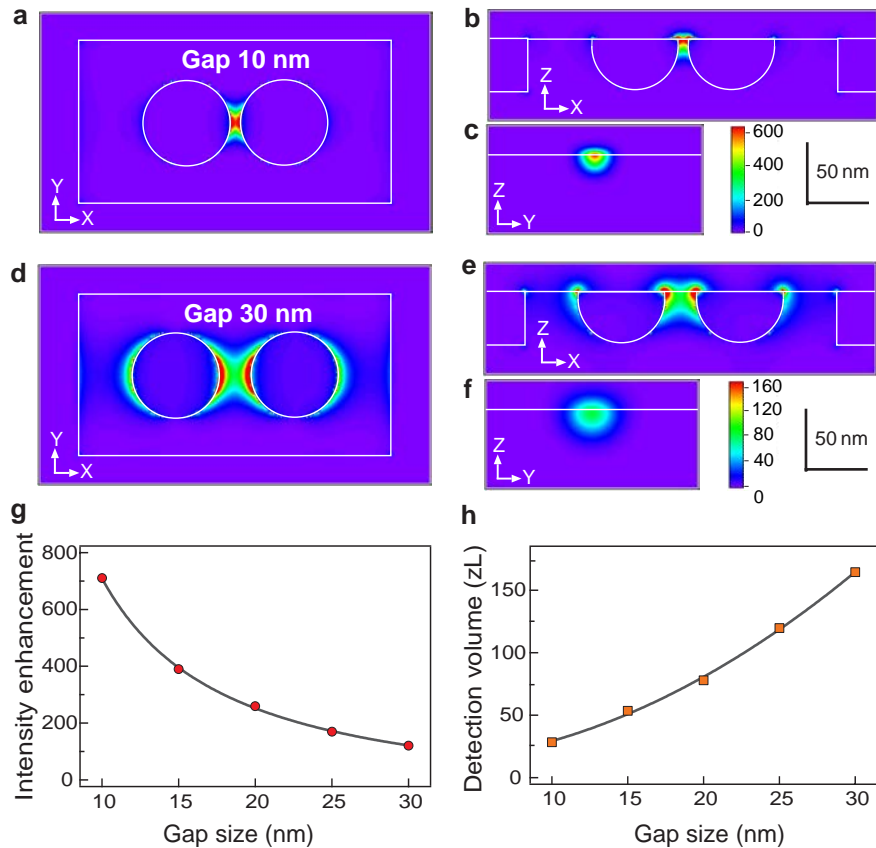


**FIGURE 5.4: Numerical simulations of excitation intensity enhancement and estimation of detection volume.** Excitation intensity enhancement at 633 nm are computed using finite-difference time-domain method for a nanoantenna of 10 nm gap size (a-c) and 30 nm gap (d-f). FDTD modeling is performed using mesh size 0.5 nm for (a-c) and 1 nm for (d-f). The intensity is recorded at the antenna surface for (a,d) and along planes crossing the antenna's center for (b,c) and (e,f). (g) Evolution of the peak intensity enhancement at 633 nm computed in the gap region as a function of the antenna gap size. (h) Evolution of the detection volume as a function of the nanoantenna gap size.

volumes, considers the product of the typical decay distances along X, Y and Z axis obtained from the intensity maps. To accurately model the experimental data, for the X axis we take the gap size plus the nanoparticle radius, while for the Y axis, we take the full width at  $1/e^2$ . For the Z axis, we take the decay length at  $1/e^2$ , taking only into account the zone accessible to the solution sample. As we will discuss later in the upcoming Section 5.5.1 (FCS to quantify near field detection volume), these empirical estimation of the detection volumes stand in excellent agreement with those acquired from fluorescence experimental data.

Figure 5.5 shows the experimental dark-field scattering spectra measured for 10 nm (a) and 35 nm (b) gap sizes and both polarization configurations of the illumination light. The polarization sensitivity, and gap size influence is further confirmed by these dark-field spectra. Figure 5.5 displays the fluorescence spectra of Alexa Fluor 647 (c)

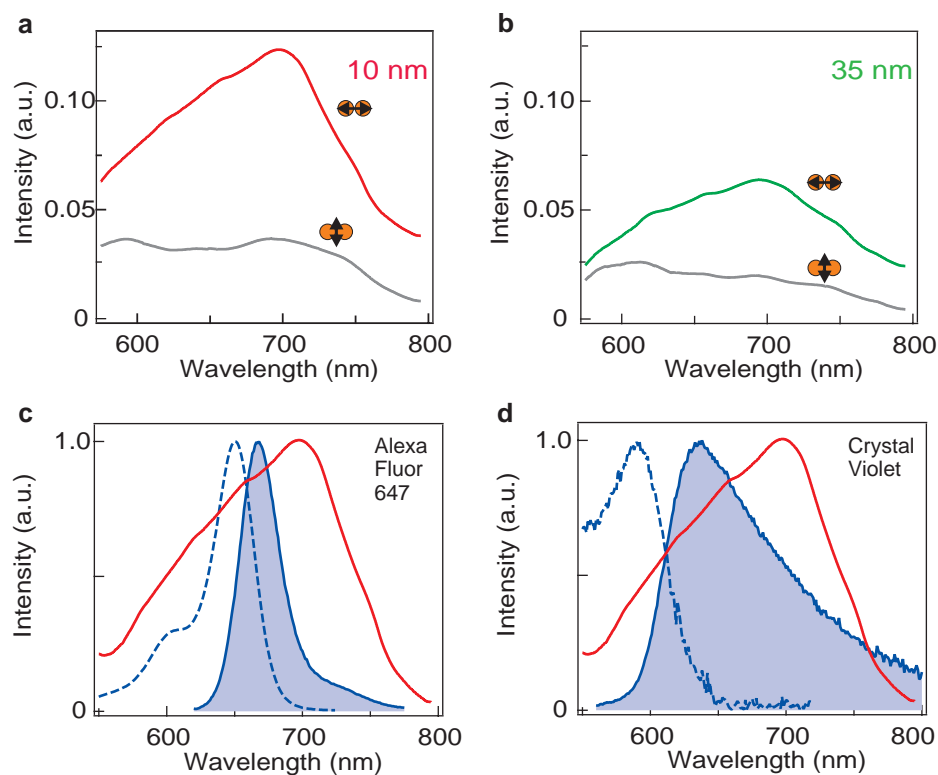


**FIGURE 5.5: Overlap between antenna's resonance and fluorescence spectra.** (a,b) Dark-field scattering spectra for 10 nm (a) and 35 nm (b) gap sizes and two orientations of the illumination polarization. (c,d) Spectral overlap of the 10 nm antenna's response (red lines) with parallel orientation compared to the fluorescence spectra for Alexa Fluor 647 (c) and Crystal Violet (d). Excitation spectra are shown with dashed lines, emission spectra with solid shaded lines.

and Crystal Violet (d) fluorophore and indicates the excellent overlap with the spectral response of 10 nm antenna (red lines) excited in parallel configuration. The dashed lines represent the excitation spectra, while the solid shaded lines being the emission spectra.

## 5.4 Experiment and results: Burst analysis of single-diffusing fluorophores

The fluorescence experiment setup is based on an inverted confocal microscope with a high NA water-immersion objective and is the same as used in earlier experiments (double nanohole and silicon dimers). The details on each optical component is presented in Chapter 2. Fluorescence burst analysis with these planar “antenna-in-box” devices are performed using two different dyes: Alexa 647 molecules with 200 mM methylviologen (8% quantum yield) and Crystal Violet molecules (2% quantum yield), both of which have similar excitation spectra.

Fluorescence experiments are performed by covering the nanoantenna substrate with a solution containing  $1 \mu\text{M}$  Alexa Fluor 647 with 200 mM methylviologen in water-glycerol solution (1:1 ratio). Use of glycerol essentially slows down the diffusion of molecules through the confined nanoantenna hotspot eventually making the single-molecule events stand out more prominently on top of a near constant background. The experiments are carried out for different gap separations (10, 25 and 35 nm gaps), the fluorescence enhancement factors are then quantified in each case.

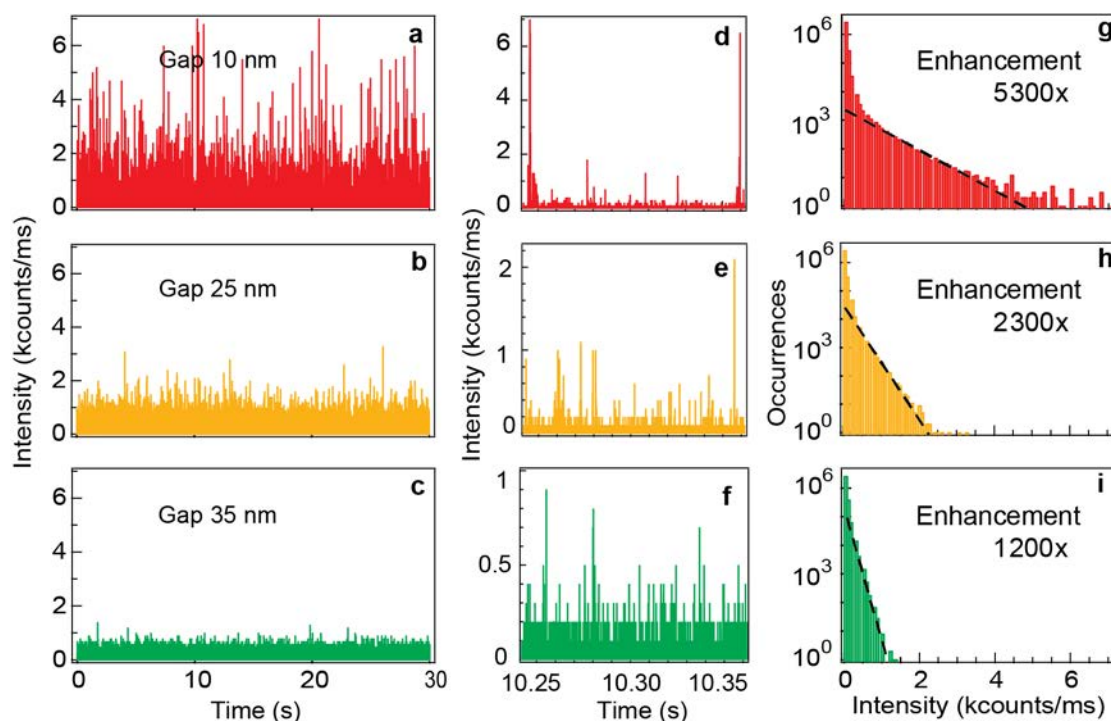


**FIGURE 5.6: Fluorescence bursts analysis on Alexa Fluor 647 molecules.** Fluorescence bursts analysis to determine the enhancement factors for Alexa Fluor 647 molecules with 200 mM methylviologen. (a-c) Fluorescence time traces recorded on nanoantennas with increasing gap sizes using  $1 \mu\text{M}$  Alexa Fluor 647 in water-glycerol 1:1 solution with  $2.3 \text{ kW/cm}^2$  excitation intensity at 633 nm. The binning time is  $10 \mu\text{s}$ . (d-f) Enlarged temporal windows showing discrete bursts that correspond to individual molecules crossing the antenna detection volume. (g-i) Photon count rate histograms deduced from the traces in (a-c). The dashed lines are fits by exponentially decaying probability distributions. A reference of 0.85 counts/ms for Alexa Fluor 647 (with 200 mM methylviologen as chemical quencher) is used to compute the fluorescence enhancement factors.

Figure 5.6a-c shows the single molecule fluorescence time trace for Alexa Fluor 647 probed with planar “antenna-in-box” devices with increasing gap sizes: 10 nm (a), 25 nm (b) and 35 nm (c). Enlarged temporal windows (d-f) display discrete bursts that correspond to individual molecules crossing the nanoantenna detection volume. Intense fluorescence bursts are clearly detected on the fluorescence time traces, with their amplitude decreasing as the gap size is enlarged. This feature confirms that the fluorescence

bursts stem from the confined nanoantenna gap region (hotspot). All the time traces are recorded with  $2.3 \text{ kW/cm}^2$  excitation intensity at 633 nm, binned at  $10 \mu\text{s}$  and finally collected in the photon count histograms (g-i). These histograms are then fitted using exponentially decaying probability distributions represented by the dashed lines. The recorded maximum peak amplitude is then used to calculate the fluorescence enhancement factors for each gap size.

For a 10 nm gap antenna, we record a peak amplitude with intensity 4.5 kcounts/ms. Using the reference of 0.85 counts/ms for Alexa Fluor 647 (with 200 mM methylviologen as chemical quencher), we derived  $4.5\text{k}/0.85 = 5300\times$  fluorescence enhancement for a nanoantenna with 10 nm nominal gap. The calculation of 0.85 counts/ms brightness per molecules in the case of confocal reference is summarized in Figure 5.7. Alexa Fluor 647 molecules fluorescence bursts events recorded with confocal configuration (without nanoantenna) with very diluted  $\sim 10 \text{ pM}$  fluorophore concentration. This low fluorophore concentrations ensures that the fluorescence bursts (a,b) stem from individual molecules crossing the 0.5 fL confocal detection volume. No methylviologen is used to reach  $\sim 30\%$  quantum yield and the excitation intensity is increased by  $4\times$  to reach  $9.2 \text{ kW/cm}^2$ . Thus to compute the reference count rate per molecule for the experiments in Figure 5.6, we take the highest intensity in the confocal photon count rate histogram (Figure 5.7c), correct for the  $4\times$  lower excitation intensity and  $4\times$  lower quantum yield in the presence of methylviologen, to reach a value of  $13/(4*4) = 0.85 \text{ counts/ms}$ .

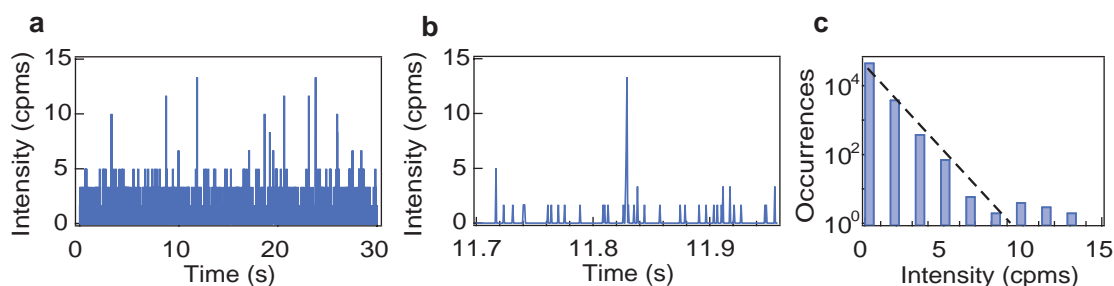


**FIGURE 5.7: Reference fluorescence bursts analysis for Alexa Fluor 647.** (a) Fluorescence time trace for Alexa Fluor 647 in confocal setup (detection volume 0.5 fL). A concentration of 10 pM ensures that the fluorescence bursts stem from individual molecules (b). No methylviologen is used to reach a quantum yield  $\sim 30\%$ . The excitation intensity is increased here by  $4\times$  to reach  $9.2 \text{ kW/cm}^2$ . The binning time is 0.6 ms to optimize the signal-to-noise ratio. (c) Photon count rate histogram deduced from the trace in (a). The dashed line is a fit by an exponentially decaying probability distribution. To compute the reference count rate per molecule for the experiments in Figure 5.6, we take the highest intensity, correct for the  $4\times$  lower excitation intensity and  $4\times$  lower quantum yield in the presence of methylviologen, to reach a value of  $13/(4*4) = 0.85 \text{ counts/ms}$ .

Emitters with low quantum yields allow reaching higher fluorescence enhancement factors, as the nanoantenna benefits from a larger increase in the emission quantum yield of the dye [151, 152]. To experimentally demonstrate this effect, we perform similar fluorescence burst analysis measurements with Crystal Violet molecules which have a weaker 2% quantum yield as compared to 8% in case of Alexa647 with 200 mM methylviologen. As in the case of Alexa 647, Crystal Violet fluorophore is set to a concentration of  $1 \mu\text{M}$  in a water-glycerol 1:1 solution to slow down the diffusion of fluorophore crossing the nanoantenna hotspot, and thereby allowing direct analysis of the fluorescence bursts for individual molecules.

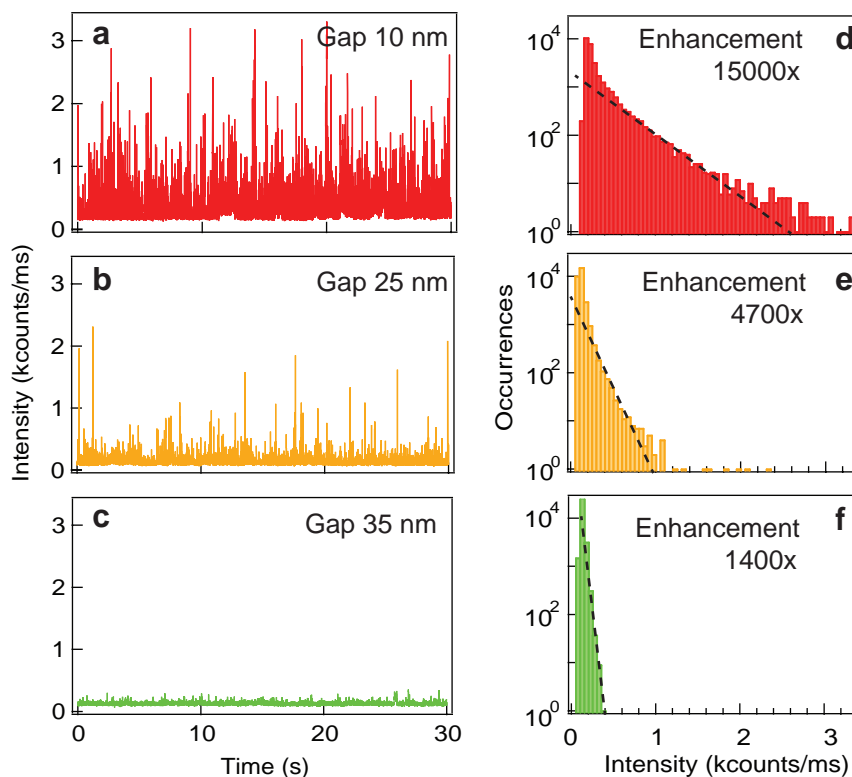


**FIGURE 5.8: Fluorescence enhancement on Crystal Violet molecules measured with fluorescence bursts analysis.** (a-c) Fluorescence time traces recorded on nanoantennas with increasing gap sizes using  $1 \mu\text{M}$  of crystal violet in water-glycerol 1:1 solution with  $2.3 \text{ kW}/\text{cm}^2$  excitation intensity at 633 nm. The binning time is 1 ms. (d-f) Photon count rate histograms deduced from the traces in (a-c). The dashed lines are fits by exponentially decaying probability distributions.

Figure 5.8 summarizes the fluorescence burst analysis for Crystal Violet molecules as probed by the planar antenna-in-box platforms with increasing gap separations. Intense fluorescence bursts are detected on the fluorescence time traces (a-c), with their amplitude decreasing as the gap size is enlarged from 10 nm to 35 nm. This feature is consistent with the burst analysis for Alexa647 molecules and confirms that the fluorescence bursts stem from the confined nanoantenna hotspot region. To measure the fluorescence

enhancement factors for the case of diffusing CV molecules, we fit the photon count histograms in Figure 5.8d-f with exponentially decaying probability distributions and record the maximum peak amplitude in the fitted distribution. The estimation of the peak fluorescence count per CV molecule for confocal reference is shown in Figure 5.9. As the CV molecules have a very low  $\sim 2\%$  quantum yield, detecting individual burst and estimating their count rates for confocal reference need extra care. We perform burst analysis at  $\sim \text{pM}$  concentration with higher excitation powers followed by a confocal FCS analysis (at  $\sim \text{nM}$  concentration) to accurately estimate the confocal count rates for CV molecules.

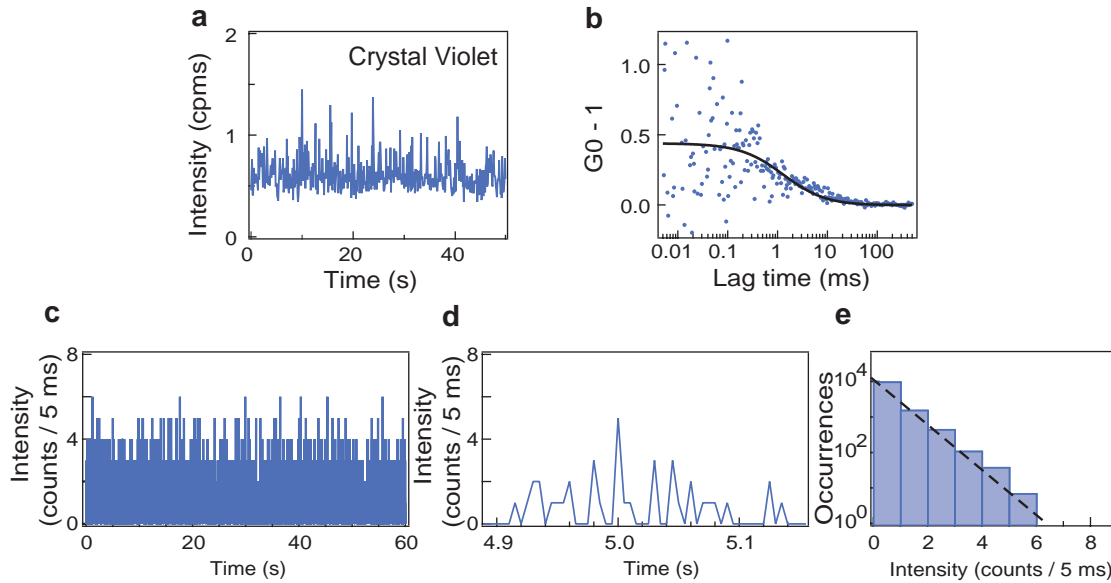


**FIGURE 5.9: Confocal reference data for Crystal Violet molecules.** (a) Intensity time trace and (b) correlation curve for Crystal Violet molecules diffusing in confocal volume. The excitation intensity at 633 nm is raised to  $6\times$  to  $13.8 \text{ kW/cm}^2$  to provide enough signal to noise ratio. For the FCS analysis on this experiment, we take into account the  $0.15 \text{ counts/ms}$  dark count noise of our APDs to quantify an average number of 1.3 molecules with  $0.36 \text{ counts/ms}$  as brightness per molecule. The concentration is further diluted by  $5\times$  to ensure that the fluorescence bursts stem from individual molecules (c,d), and the photon count rate histogram deduced from the time trace in (c) is displayed in (e). The dashed line is a fit by an exponentially decaying probability distribution. The excitation intensity is  $13.8 \text{ kW/cm}^2$ , and is  $6\times$  higher than the intensity used for the antenna experiments of Figure 5.8. The binning time is 5 ms. To compute the reference count rate per molecule for the experiments in Figure 5.8, we take the highest intensity above the noise level, correct for the  $6\times$  lower excitation intensity and 5 ms binning time to reach a value of  $5.5/(6*5) = 0.18 \text{ counts/ms}$ .

Figure 5.9 shows the fluorescence time trace (a) of the diluted Crystal Violet molecules diffusing through the confocal volume and recorded at a higher excitation powers  $6\times$  to  $13.8 \text{ kW/cm}^2$  to provide enough signal to noise ratio, and the corresponding correlation curve (b). For FCS analysis on this experiment, we take into account the  $0.15 \text{ counts/ms}$  dark count noise of our APDs to quantify an average number of 1.3

molecules with brightness per emitter being 0.36 counts/ms. Now we further dilute the solution by  $5\times$  to visualize single diffusing fluorophore in confocal volume (c,d). Photon count rate histogram is then deduced from the confocal time trace and is displayed in (e). The excitation intensity is  $13.8 \text{ kW/cm}^2$  and is  $6\times$  higher than the intensity used for the nanoantenna experiments of Figure 5.8. The dashed line is a fit by an exponentially decaying probability distribution indicating a peak intensity amplitude being 5.5 counts/bin time. Thus using this peak intensity value above the noise level, correcting for the  $6\times$  lower excitation intensity and 5 ms binning time, we reach the value of  $5.5/(6*5) = 0.18 \text{ counts/ms}$ . This value of confocal reference is then used to estimate the fluorescence enhancement factors for time traces acquired with antenna-in-box devices. The confocal reference fluorescence counts per CV molecule estimated at 0.18 counts/ms at  $2.30 \text{ kW/cm}^2$  excitation power is in agreement with values reported independently in Refs. [16, 17].

From the photon counts histogram for 10 nm gap antenna (Figure 5.8a), the maximum count is 2750 counts/ms with a background of 100 counts/ms set by the fluorescence from the CV molecules diffusing away from the hotspot region and the residual photoluminescence from the metal. This quantifies to an impressive fluorescence enhancement of  $2750/0.18 = 15,000\times$  for CV molecules diffusing through the nanogaps. The same procedure for 25 nm and 35 nm gap separations yields fluorescence enhancement of  $4700\times$  and  $1400\times$  respectively. It is worth recalling that the same procedure performed on Alexa Fluor 647 with 200 mM methylviologen (8% quantum yield) indicated a fluorescence enhancement of  $5300\times$  for a 10 nm gap antenna. The relative change in the enhancement factors results from the differences in the quantum yield between CV (2%) and Alexa 647 (8%) and further confirms that our measurements are not influenced by artifacts.

## 5.5 Optical performance at high molecular concentration

After discussion on the fluorescence burst analysis (experiments performed at  $1 \mu\text{M}$  concentration), we now elaborate the optical performance of these nanoantennas with FCS experiments at very high  $26 \mu\text{M}$  concentrations of Alexa 647 molecules along with 200 mM methylviologen as the chemical quencher.

### 5.5.1 FCS: Planar nanoantennas at 26 $\mu\text{M}$ Alexa Fluor concentration

FCS determines the average number of detected molecules from which the fluorescence brightness per emitter and the detection volume can be deduced. This gives an alternative validation to the fluorescence enhancement factors from burst analysis and also provides an estimation on the antenna's near field detection volume. Figure 5.10a,b displays the raw fluorescence intensity time traces and corresponding correlation curves with excitation polarization parallel (colored dots) and perpendicular (gray dots) to the antenna dimer axis for two different 10 nm and 35 nm gap separations. Larger fluctuations in fluorescence time trace and higher correlation amplitudes are clearly observed when the incident electric field is parallel to the dimer axis and when the gap size is reduced. This directly evidences the presence of an electromagnetic hotspot in the nanoantenna gap region. In contrast to the parallel excitation, all the relevant observables, nanoscale volume confinement and fluorescence enhancement disappear when the laser polarization is oriented perpendicular to the main antenna axis or when the gap size is increased to 35 nm gap. We performed control experiments with an extra 8 nm thick silica layer deposited on top of the nanoantennas to prevent the molecules from accessing the hotspot region. In this case, the FCS signal is lost (see Figure 5.10c,d) confirming the crucial role of the few nanometer region surrounding the antenna gap.

All the FCS experiments are performed at 26  $\mu\text{M}$  concentration of Alexa Fluor 647, corresponding to about 7630 molecules in the 0.5 fL confocal detection volume. Figure 5.11 shows the confocal FCS analysis for Alexa 647 with 200 mM methylviologen with experimental condition exactly similar to those for Nanoantenna-FCS measurements displayed in Figure 5.10. The correlation amplitude scales as the inverse of the number of fluorescent molecules in the detection volume, so for the confocal reference without the nanoantenna, the FCS amplitude is barely detectable at  $1.31e^{-4}$ , which amount to 7630 molecules in the 0.5 fL confocal volume. The average fluorescence brightness per molecule is then derived as  $1800/7630 = 0.24$  counts/ms.

However the correlation amplitudes of 3.9 are detected with the nanoantennas of 10 nm gap size, representing 0.26 number of molecules on average diffusing through the hotspot region. This corresponds to  $N_{antenna}/N_{conf} = 30,000\times$  volume reduction than the diffraction-limited confocal volume. Using the known 26  $\mu\text{M}$  fluorophore concentration and the 0.5 fL confocal volume, the antenna detection volume is then quantified to be 17 zL ( $1 \text{ zL} = 10^{-21} \text{ L} = 1000 \mu\text{m}^3$ ). This represents the smallest antenna detection volume reported so far for FCS applications on nanoantennas. The reduction of the detection volume is further confirmed by the shortening of the diffusion time, from 64  $\mu\text{s}$  in the diffraction-limited confocal volume to 0.9  $\mu\text{s}$  in the nanoantenna case.

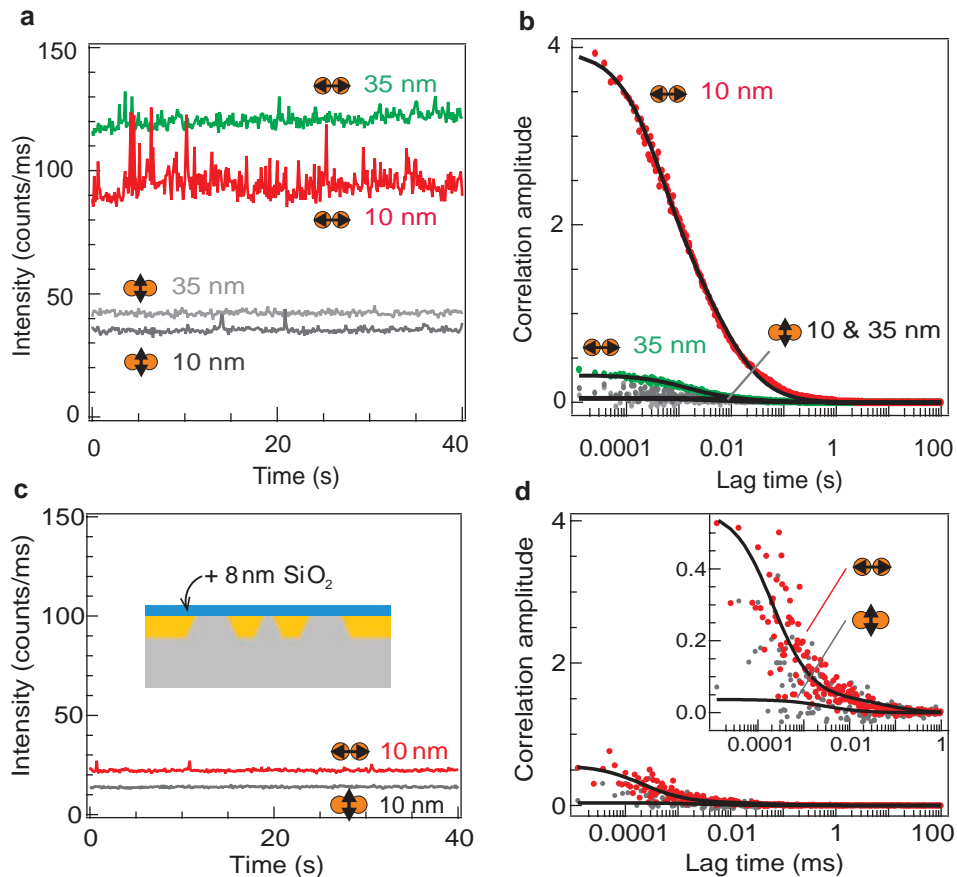


**FIGURE 5.10: Nanoantennas enhance the fluorescence detection of Alexa Fluor 647 molecules in solution.** (a) Fluorescence time traces and (b) corresponding FCS correlation functions (dots, raw data; lines, numerical fits) for nanoantennas with 10 and 35 nm gap sizes with the excitation polarization set parallel or perpendicular to the antenna's main axis. The experimental conditions correspond to 26  $\mu\text{M}$  of Alexa Fluor 647 with 200 mM of methylviologen as chemical quencher under 2.3  $\text{kW}/\text{cm}^2$  excitation intensity at 633 nm wavelength. (c) Control experiment with 8 nm SiO<sub>2</sub> deposited on top of the nanoantenna. Adding an extra 8 nm layer of silica on top of the nanoantenna blocks most of the fluorescence by preventing the molecules from accessing the hot spot region. To enable a direct comparison, the experimental conditions and figure scales in c, d are identical to the ones used in a, b, and confirm that the nanoscale detection volume is located at the antenna surface.

For our earlier experiments (double nanoholes and silicon dimer antennas), the background fluorescence from molecules diffusing away from the hotspot had a significant contribution in the total fluorescence signal, thereby complicating the FCS analysis. In our earlier chapters, we used a two-species model (incorporating hotspot and background contribution) for FCS analysis to estimate count rate per molecule only from the hotspot region. However, in the case of planar antenna-in-box devices, we find that the signal from the hotspot always largely dominates the background, so that the previously used corrections are no longer needed. The number of detected molecules is simply the inverse of the correlation amplitude at zero lag time, and the fluorescence brightness

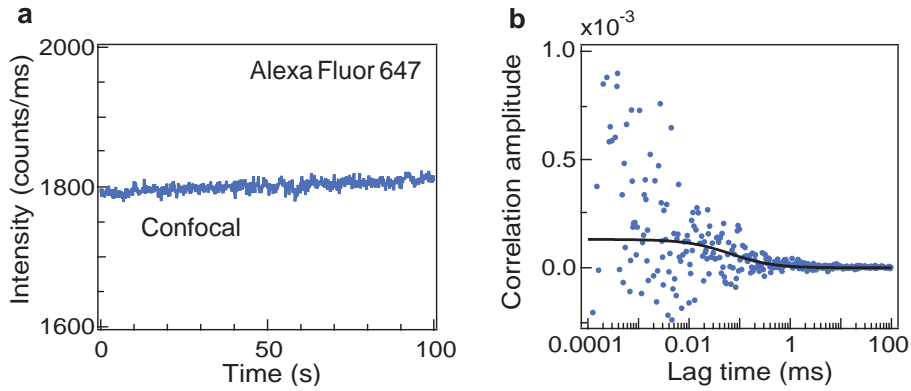


**FIGURE 5.11: Confocal reference for FCS experiments on Alexa Fluor 647**(a) Intensity trace and (b) FCS correlation function. The experimental conditions are identical to the measurements on nanoantennas: the concentration of Alexa Fluor 647 is  $26 \mu\text{M}$ , with  $200 \text{ mM}$  of methylviologen as chemical quencher. The excitation intensity is  $2.3 \text{ kW/cm}^2$  at  $633 \text{ nm}$  wavelength. The FCS correlation amplitude is  $1.31e^{-4}$ , which amount to  $7630$  molecules in the  $0.5 \text{ fL}$  confocal detection volume. The average fluorescence brightness per molecule is  $1800/7630 = 0.24 \text{ counts/ms}$ .

per emitter can be computed by normalizing the average fluorescence intensity by this number of detected molecules. For the antenna with  $10 \text{ nm}$  gap size, we find a brightness of  $370 \text{ counts/ms}$ . This value is  $1600\times$  higher than the  $0.24 \text{ counts/ms}$  estimated for the dye in the confocal reference. The polarization sensitive correlation curves with amplitudes confirms the occurrence of large fluorescence enhancement in the nanogaps.

It should be noted that the fluorescence enhancement factors for Alexa 647 estimated from the burst peak intensity ( $5300\times$  for  $10 \text{ nm}$  gap antenna as shown in Figure 5.6) is about  $3\times$  higher than the one measured with FCS ( $1600\times$  for same gap separation as shown in Figure 5.14). This is expected as the burst analysis favors the best event where the emitter's position and orientation lead to the highest fluorescence intensity.

We carried out similar FCS experiments with  $10 \text{ nm}$  gap nanoantenna (excitation parallel to the dimer axis) to study the excitation power dependence on the optical performance. Figure 5.12 shows the raw fluorescence trace of  $26 \mu\text{M}$  Alexa647 with  $200 \text{ mM}$  of methylviologen as chemical quencher (a), the evolution of the average fluorescence intensity as the function of excitation intensity (b) and the corresponding normalized correlation curves (c). The average fluorescence intensity count rate shows limited saturation for excitation intensity exceeding  $3.4 \text{ kW/cm}^2$ . As all of our fluorescence experiments are carried out at  $2.3 \text{ kW/cm}^2$  excitation intensity, our results are not affected by any photophysical artifacts. Moreover, as the shapes of the correlation curves at short lag times appear similar with different excitation powers, the influence of triplet blinking is avoided in the FCS analysis. As a final control experiment, in Figure 5.13 we show that in the absence of fluorescent molecules, the residual background luminescence from the

gold nanoantenna (a) remains negligible and thereby exhibiting no temporal correlation (b).

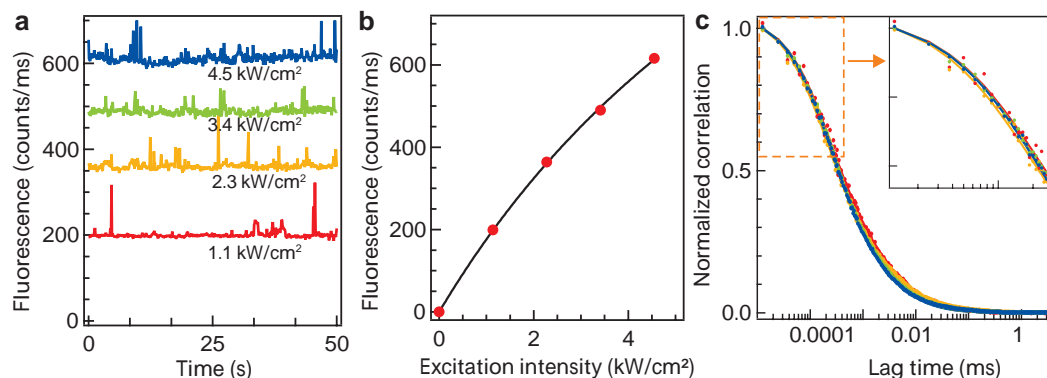


**FIGURE 5.12: Power dependence study shows limited saturation and no triplet blinking effects.** (a) Fluorescence time trace recorded on a 10 nm gap antenna with increasing illumination intensities. (b) Evolution of the average fluorescence intensity as function of the excitation intensity showing that the 2.3 kW/cm<sup>2</sup> used in this study is well within the linear fluorescence regime. (c) Normalized FCS correlation functions of the traces in (a) with same color code. The similar shapes at short lag times reveal a negligible influence of triplet state blinking in the FCS data.

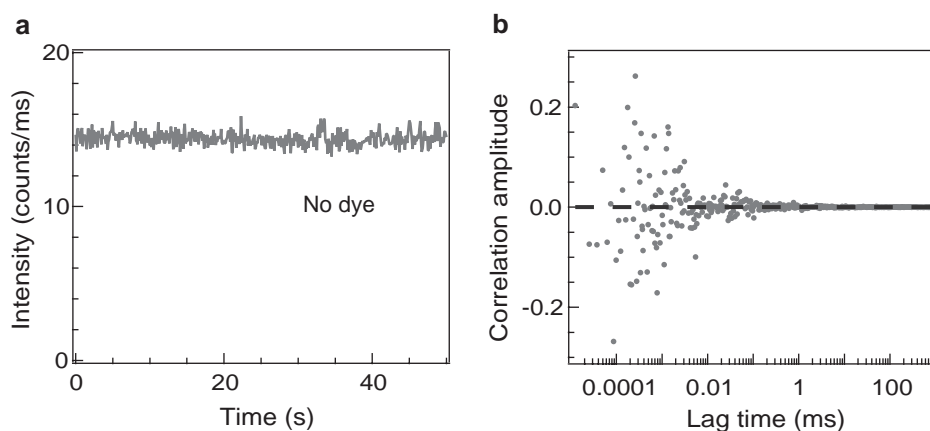


**FIGURE 5.13: Nanoantenna luminescence background in the presence of 200 mM methylviologen and no fluorescent dye.** (a) Intensity trace and (b) FCS correlation function on a 10 nm gap antenna. The 2.3 kW/cm<sup>2</sup> excitation intensity at 633 nm is similar to all experiments.

For bio-inspired applications of nanoantennas, it is desired to have arrays of structures having sharp edges with reproducible optical performances. As shown in TEM metrology (see Figure 5.3), using the described procedure, mass fabrication of sub 20 nm gap antenna is possible. To assess the statistical reproducibility of the antenna performance, we repeat the FCS experiments on a set of more than 80 different antennas and measure for each antenna its fluorescence enhancement and the near field detection volume. Scatter plot displayed in Figure 5.14a, clearly indicates a correlation between the fluorescence enhancement and the detection volume following an empirical power law with

-2/3 exponent: the volume scales as cube power of the typical near field size, while the fluorescence enhancement is dominated by the gain in local excitation intensity which scales as the square of the typical near-field size.

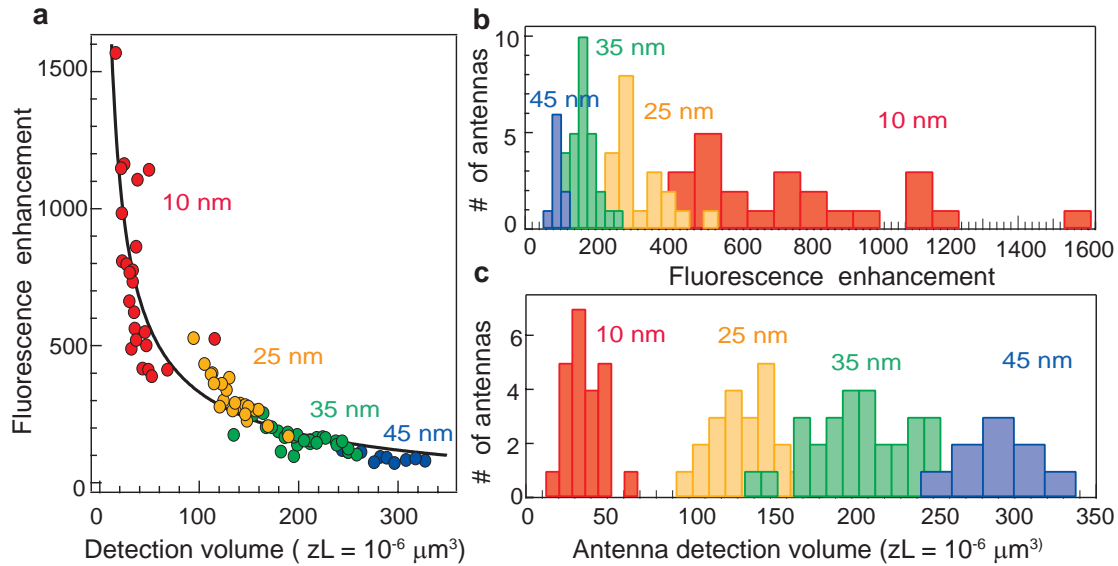


**FIGURE 5.14: Statistical reproducibility of the nanoantennas measured by FCS** (a) Scatter plot of the fluorescence enhancement versus the nanoantenna’s detection volume as deduced from FCS analysis on 83 different nanoantennas. The black line fit follows a power law dependence with a fixed -2/3 exponent. (b) Distribution of fluorescence enhancement factors deduced from the data in (a) for different gap sizes. (c) Distribution of the nanoantenna detection volume.

Figure 5.14 shows the histograms of the fluorescence enhancement (b) and detection volume (c) illustrating the statistical dispersion of the data around the average for each value of the desired nominal gap size. The variability of the gap sizes as characterized by TEM (see Figure 5.3), influences this dispersion. This is more prominent for the smaller gaps where a nanometric variation in the gap size can have a large influence on the antenna’s performance and the measured enhancement factor.

We now compare the performance of these planar nanoantennas with the FCS results achieved previously using focused ion beam milling [89]. Figure 5.15 compares the average values of fluorescence enhancement (a) and detection volume (b) obtained for nanoantennas fabricated with conventional FIB milling and template-stripped E-beam lithography. The nanoantennas are tested under similar conditions for FCS experiments to ensure a consistent benchmarking. As demonstrated in Figure 5.15, template-stripped E-beam lithography provides higher fluorescence enhancement factors in smaller detection volumes. The improvement over FIB milling is especially significant for gap sizes above 25 nm, where the new fabrication technique can lead to a  $10\times$  increase for the fluorescence enhancement factor together with a  $5\times$  reduction for the detection volume.

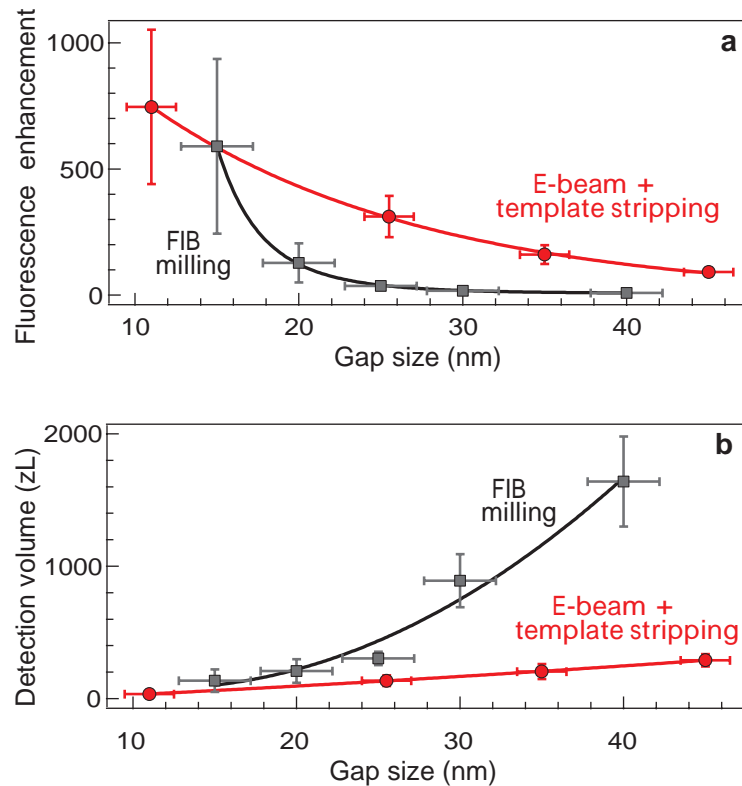


**FIGURE 5.15: Improved nanoantenna’s performance with template-stripped electron beam lithography as compared to focused ion beam milling (FIB).** Average values of fluorescence enhancement (a) and detection volume (b) as a function of the gap size. The data for focused ion beam (FIB) milling is taken from Ref. [89]. The experimental conditions are similar for both fabrication methods (Alexa 647 fluorophores with 200 mM methylviologen). Error bars correspond to one standard deviation. The performance of these new optical nanoantennas significantly outperforms the values achieved previously using focused ion beam lithography providing higher fluorescence enhancement factors in smaller detection volumes.

### 5.5.2 Fluorescence lifetime reduction and LDOS enhancement

The presence of a nanoantenna in the vicinity of the fluorophore accelerates the decay rates as compared to the free space de-excitation. We now study this increased LDOS (Purcell effect) in case of planar “antenna-in-box” platforms and discuss different rates and the evolution with gap sizes. The experimental setup is the same as used in earlier projects (double nanohole and silicon dimers), and the description of the optical setup is already presented in Chapter 2.

The TCSPC experiment for planar antenna-in-box is carried out with Alexa647 fluorophore with 200 mM methylviologen. The experimental conditions are similar to those used for FCS (Figure 5.10), with only difference being the pulsed excitation. Figure 5.16a shows the normalized time-resolved decay traces for three cases: confocal (blue dots),

35 nm gap (green dots) and 10 nm (red) gap separation for antenna in box with parallel excitation. The inset summarizes the fluorescence lifetime for all gap separations together with confocal and box-only configuration. As expected, the decay kinetics are comparable for the confocal reference and the box-only geometry. In contrast, excitation along the gap induces a clear acceleration of the decay dynamics for all gap separations: fast acceleration with smallest gap size. The fluorescence lifetime is significantly reduced from  $380 \pm 15$  ps in confocal illumination to  $45 \pm 10$  ps for the 10 nm gap antenna.

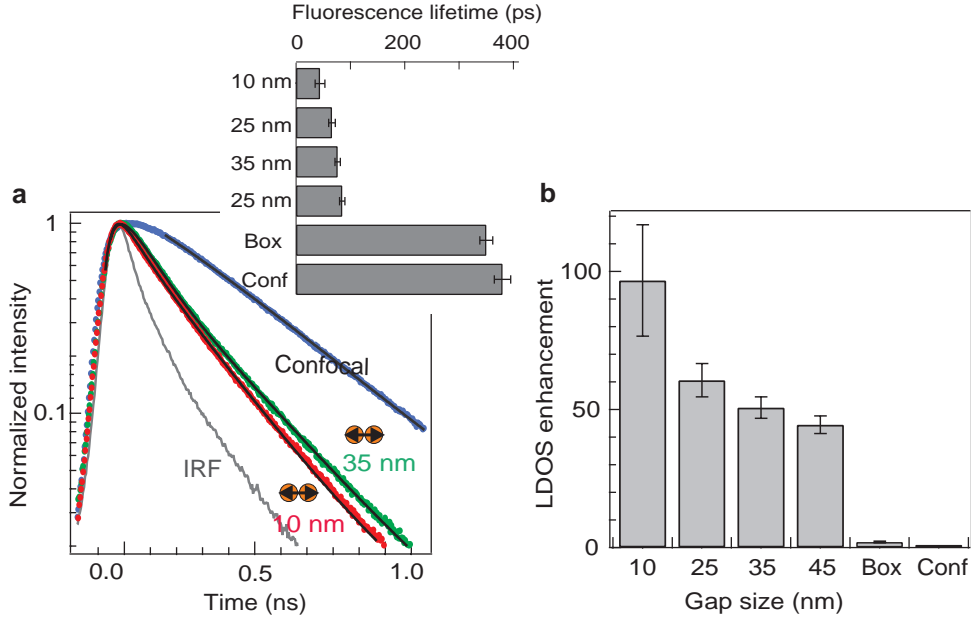


**FIGURE 5.16: Fluorescence lifetime reduction and LDOS enhancement.** (a) Normalized time-resolved decay traces show Alexa Fluor 647 fluorescence lifetime reduction as the gap size is reduced. Black lines are numerical fits convoluted by the instrument response function (IRF). The inset shows the fluorescence lifetime of Alexa Fluor 647 in presence of 200 mM of methylviologen as function of the nanoantenna gap size. (b) Local density of optical states (LDOS) enhancement deduced from the lifetimes in (a), after correction of the methylviologen quenching rate and Alexa Fluor 647 natural non-radiative decay rate, following the procedure in Chapter 3 and 4.

Figure 5.16b summarizes the evolution of the local density of optical states (LDOS) enhancement as the function of nanoantenna gap size. LDOS is computed by removing the internal non-radiative rate contribution  $\Gamma_{nr} = 0.67 \text{ ns}^{-1}$  of Alexa Fluor 647 and the quenching rate  $\Gamma_q = 1.9 \text{ ns}^{-1}$  contribution set by methylviologen from the lifetime data measured from TCSPC experiments (see inset of Figure 5.16a).

The total decay rate (inverse of fluorescence lifetime) for 10 nm antenna,  $\Gamma_{tot}$  is  $22.22 \text{ ns}^{-1}$ . The contribution set only by the photonic environment is estimated to be  $\Gamma_{rad}^* + \Gamma_{loss}^* = \Gamma_{tot} - \Gamma_{nr} - \Gamma_q = 19.7 \text{ ns}^{-1}$ . The LDOS enhancement is then computed as  $(\Gamma_{rad}^* + \Gamma_{loss}^*)/\Gamma_{rad} = 19.7/0.21 = 100\times$  keeping only the rate influenced by the photonic environment. This correction procedure is consistently used throughout the thesis, as the

internal non-radiative rate of Alexa and the quenching rate from the methylviologen are not influenced by the presence of nanoantenna.

Finally the measured fluorescence enhancement factor is modeled using the equation [93]:

$$\eta_F = \frac{I_{exc}^*}{I_{exc}} \frac{\Gamma_{rad}^*}{\Gamma_{rad}} \frac{1}{1 - \phi_0 + \phi_0 (\Gamma_{rad}^* + \Gamma_{loss}^*)/\Gamma_{rad}} \quad (5.1)$$

This equation follows that the fluorescence enhancement  $\eta_F$  is the consequence of the excitation intensity enhancement  $I_{exc}^*/I_{exc}$ , enhancement of the radiative decay rates  $\Gamma_{rad}^*/\Gamma_{rad}$ , and together with the influence of initial quantum yield  $\phi_0$  of the fluorescent molecule modified within the nanogap. The third term in the above Equation 5.1 incorporates an additional decay rate  $\Gamma_{loss}^*$  describing the non-radiative energy transfer to the antenna's material induced by ohmic losses. For the smallest 10 nm gap and a dipole emitter located in the gap center, the FDTD simulations estimate the different contributions to be  $I_{exc}^*/I_{exc} = 600$ ,  $\Gamma_{rad}^*/\Gamma_{rad} = 700$  and  $(\Gamma_{rad}^* + \Gamma_{loss}^*)/\Gamma_{rad} = 1100$  (see near field simulations in Figure 5.4). Neglecting the collection efficiency improvement brought by the nanoantenna, the fluorescence enhancement values can be predicted to be  $18,000\times$  for crystal violet and  $4700$  for Alexa 647, which come in excellent agreement with the experimental results. The 1000-fold LDOS enhancement used in numerical estimation should be compared with the 100-fold LDOS enhancement observed experimentally by the lifetime measurements. This mismatch can partially be explained because of the spatial and orientation averaging during the experiments, and also due to the limited resolution of the TCSPC electronics.

## Figure of merit

Using FCS and fluorescence burst analysis, we demonstrated the superior optical performance of these planar “antenna-in-box” devices reaching giant fluorescence enhancement factors up to  $10^4$ - $10^5$  times, together with nanoscale detection volumes in the 20 zL range. Fluorescence enhancement factors displayed strong dependence in the initial quantum yield of the dye (2% for crystal violet and 8% for Alexa 647 with 200 mM methylviologen). To avoid this dependence of the fluorescence enhancement on the intrinsic quantum yield of the fluorescent reporter, the fluorescence enhancement figure of merit is defined as the product of the enhancement factor by the reference quantum yield of the emitter in homogeneous medium [60]. Thus, for crystal violet and Alexa Fluor 647, the fluorescence enhancement figures of merit amount to 300 and 420 respectively, and are among the highest reported values to date [16, 17, 18, 60, 89].

## 5.6 Polymer stability and nanoantenna durability

As described in the fabrication procedure, the semi-spheres gold dimers are embedded into an optically transparent polymer (ormocer) during the template-stripping step. This is important in order to bring the narrowest gap region at the top of the structure making it efficiently accessible to the probe sample. We demonstrated that these new class of optical antennas hold great interest for ultrasensitive fluorescence bio-sensing, especially for detecting single molecules at biologically-relevant micromolar concentrations. During the course of experimental measurements, the microscope coverslip containing these planar “antenna-in-box” structures is first rinsed with water-ethanol mixture and then cleaned with UV-Ozone treatment for 2 minutes to remove organic impurities. This optimized cleaning procedure is carried out once before and after every fluorescence experiment in order to increase the durability of these antennas. However, exposing the antenna to the UV-ozone atmosphere for a repeatedly long time can potentially damage the polymer thereby influencing the dimer position and the desired gap sizes.

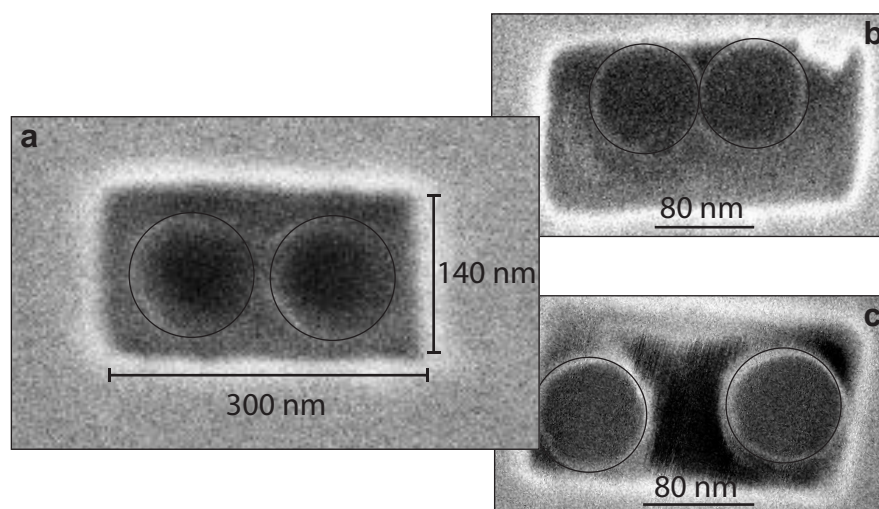


**FIGURE 5.17: Affect of UV-Ozone cleaning on the durability of nanoantennas.** Scanning electron microscope images of a representative structure imaged after 5× cleaning procedure each of them involving 5 minutes of UV exposure followed by water-ethanol rinsing (a). The same sample with addition 10× cleaning procedure shows significant damage in the polymer leading to displacement of the dimers within the box and eventually changing the desired gap dimensions. The SEM images are acquired at 1 kV to prevent further damage to the polymer and thereby the low SNR in the acquired images.

We repeatedly carried out this cleaning procedure involving UV-Ozone treatment and performed successive SEM image analysis to study the effect of the UV-Ozone treatment on the polymer stability. Figure 5.17a shows a representative structure imaged after 5× cleaning procedure (each of them involving 5 mins of UV exposure followed by water-ethanol rinsing). As seen in the SEM image (a), the 5× cleaning procedure indicates no

major troubles and the dimers are placed at the center of the box aperture. However the same coverslip when exposed to 10× cleaning procedure shows significant displacement of the dimers (Figure 5.17b,c). Although the UV-Ozone treatment is important just before the experiments to renders the gold surface hydrophilic and to remove any residual dyes after each fluorescence experiment, one should be aware that an excessive UV-Ozone treatment may eventually lead to significant damage to the polymer in which the dimers are embedded after template stripping. This etching rate (1-2 nm/min of UV-exposure), if not paid proper care will lead to displacement of the dimers within the box changing the desire gap dimensions and thereby misleading observations of the optical performance.

## 5.7 Summary

We have described the combination of electron beam lithography and template stripping as a reliable method to fabricate nanoantennas with direct accessibility of the hotspot region, large-scale availability, and gap sizes as small as 10 nm with sharp edges. Fluorescence burst analysis on single diffusing fluorophore resulted on impressive 15,000-fold fluorescence enhancement with micro second transit time in 10 nm gap antennas. Moreover we demonstrated the potential of these devices for single-molecule detection at very high 26  $\mu\text{M}$  concentrations and realized a 30,000-fold volume reduction (20 zL) as compared to 0.5  $\mu\text{m}^3$  diffraction-limited confocal volume. Moreover using TCSPC experiments, we measured a 100-fold LDOS enhancement for fluorophores diffusing within these nanometric gaps.

Several additional test experiments confirmed the near-field origin of the fluorescence signal. First, all the relevant observables, fluorescence enhancement, nanoscale volume confinement and lifetime reduction disappeared when the excitation laser was oriented perpendicular to the antenna's dimer axis or when the gap size was increased. Experiments with an extra 8 nm thick silica layer deposited on top of the antennas showed neither enhancement in the fluorescence signal and nor any correlation in FCS analysis. This confirmed that the near field volume is confined within a few-nm and with an addition layer on top, prevents the diffusing molecules from accessing the hotspot region.

Finally, we compared template-stripped electron beam lithography based nanoantenna's performance with FIB milled structures. Using fluorescence burst analysis, FCS and TCSPC measurements we demonstrated that the template-stripped E-beam lithography provides higher fluorescence enhancement factors in smaller detection volumes. The fabrication method is fully scalable and adaptable to a broad wide range of antenna designs. We foresee broad applications of these in-plane antenna geometries ranging from

large-scale ultra-sensitive sensor chips, to microfluidics and live cell membrane investigations. In next chapter, we will exploit the surface planarity of these devices to investigate the diffusion dynamics of membranes lipids in living cells.

## Chapter 6

# Planar optical antenna for nanospectroscopy in living cells

In this chapter, we investigate the nanoscopic organization of the plasma membrane of living cells combining FCS with resonant optical nanoantennas. Using planar “antenna-in-box” devices with gap separation down to 10 nm, we investigate the diffusion dynamics of phosphoethanolamine (PE) and sphingomyelin (SM) on the membranes of living Chinese hamster ovary (CHO) cells. Together with cholesterol depletion experiments, we provide compelling evidence of cholesterol-induced nanodomain partitioning in plasma membranes and discuss the impact of these results in the context of *lipid rafts*.

This project was carried out in collaboration with the team of Prof. Jürgen Brugger (EFPL, Switzerland).

### 6.1 Plasma membrane structure and FCS diffusion laws

The plasma membrane plays a major role in cell physiology and is thus of fundamental importance to living systems. The spatial organization and diffusion dynamics of its constituents (lipids and proteins) occurring at the nanoscale largely influence cellular processes: from transmembrane signaling, intracellular trafficking to the cell adhesion

---

The contents of this chapter have been published in:

**R. Regmi**, P. Winkler, V. Flauraud, K. J. E. Borgman, C. Manzo, J. Brugger, H. Rigneault, J. Wenger & M. F. García-Parajo, “Planar optical nanoantennas resolve cholesterol-dependent nanoscale heterogeneities in the plasma membrane of living cells,” **Nano Letters**, 17 (10), 6295-6302 (2017).

P. Winkler, **R. Regmi**, V. Flauraud, H. Rigneault, J. Brugger, J. Wenger & M. F. García-Parajo, “Transient nanoscopic phase separation in biological lipid membranes resolved by planar plasmonic antennas,” **ACS Nano**, 11 (7), 7241-7250 (2017).

[153, 154]. Recent advances in cell biology have shown that the plasma membrane is much more complex than just a continuous fluidic system [155, 156, 157]. It has been postulated that sphingolipids, cholesterol and certain types of proteins can be enriched into dynamic nanoscale assemblies or nanodomains, also termed *lipid rafts* [158, 159]. Lipid rafts have been defined as highly dynamic and fluctuating nanoscale assemblies of cholesterol and sphingolipids that in the presence of lipid- or protein-mediated activation events become stabilized to compartmentalize cellular processes [160]. However, the true nature of these nanodomains remains debated with many conflicting evidences and predicted domain sizes in the broad range of 10-200 nm [161, 162, 163, 164, 165, 166]. This can be understood as the direct observation of these transient and nanoscopic features are restricted by the diffraction limit in the conventional optical microscopy techniques.

Early investigations on membrane organization were mostly based on fluorescence recovery after photobleaching (FRAP) [167] and single particle tracking (SPT) [155, 168]. Both techniques are limited either in space (with  $\mu\text{m}^2$  probe area in FRAP) or in time (with millisecond temporal resolution in SPT). In addition, the conventional FCS measurements on the plasma membranes were limited to  $\sim 300$  nm spatial resolution set by the diffraction limit [162, 163, 169]. FCS is a widely adopted alternative for studying dynamics and biomolecular interactions [170] because of its high temporal resolution and a rather straightforward data analysis procedure [171, 172].

Various illumination strategies combined with FCS have been implemented over the past decade to achieve high spatial and temporal resolution, but membrane studies have so far remained above a  $\sim 40$  nm detection size. Stimulated emission depletion microscopy (STED) constrains the excitation spot down to  $\sim 40$  nm [173] and has been combined with FCS to explore the nanoscale dynamics occurring in lipid membranes on living cells [174, 175, 176, 177]. An alternative strategy takes advantage of nanophotonic structures to engineer the light intensity distribution at the nanoscale [8]. As summarized in Chapter 1, other notable designs include zero-mode waveguides [51, 52, 178, 179, 180, 181], bowtie structures [31, 147, 182], gold nanorods [55] and sub-wavelength tip based NSOM probes [10, 29]. These various approaches allow to confine the illumination light in the range of 50 to 100 nm. In recent years, resonant optical nanogap antennas have shown great potential to further constrain the laser light on a sub-20 nm scale [11] and greatly enhance the light-matter interactions [18, 60, 89]. However, so far the applications of such resonant nanogap antennas have been mostly employed to probe fluorescent molecules in solutions at high micromolar concentration.

In this project, we take advantage of recent advances in the nanofabrication to produce arrays of nanoantennas with controlled gap sizes, sharp edges and planar hotspots facing the upper surface of the sample (as introduced in earlier Chapter 5). We carried out

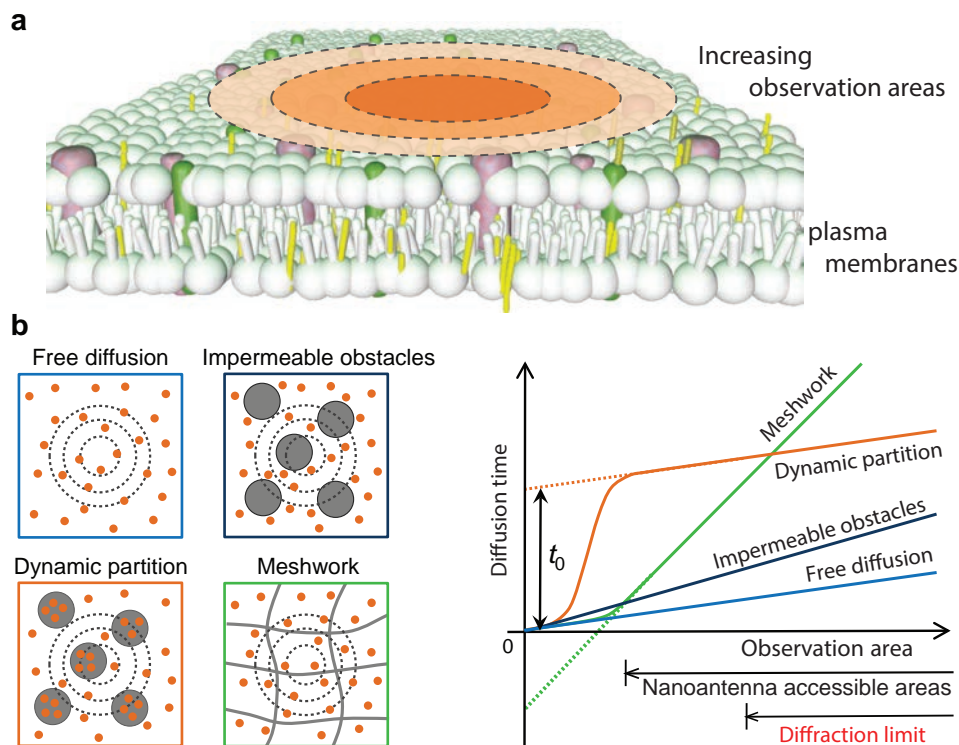


**FIGURE 6.1: Principles of FCS diffusion laws.** (a) FCS diffusion laws are constructed by measuring the average diffusion time across the increasing observation areas on a membrane. (b) Different diffusion models depending on the membrane organization lead to noticeable changes in the extrapolation of the curves through the y-axis intercept  $t_0$ , revealing the nature of the diffusion process. Free diffusion and impermeable obstacles are characterized by  $t_0 = 0$ , while a positive  $t_0$  intercept indicates the presence of nanodomains transiently trapping the molecular probe. A negative  $t_0$  intercept relates to a mesh-work of barriers separating adjacent domains.

FCS experiments on nanantennas with different gap sizes (see Figure 6.1a) to record the evolution of the diffusion time as a function of the illumination probe area. This essentially allows us to assess the nanoscale heterogeneities in the plasma membranes that would hinder the diffusion dynamics of the dye.

First introduced by Lenne *et al* [162, 169], this so called “FCS diffusion law” approach, allows to determine the nature of the diffusion process and the underlying membrane organization at scales smaller than the accessible experimental observation areas (see Figure 6.1b). The slope of the diffusion plot *vs* probe area essentially represents the effective diffusion coefficient describing the long-range mobility of the molecule, while the y-intercept  $t_0$  on the time axis indicates the underlying membrane organization principle at small scales. Mathematically, the overall diffusion time ( $t$ ) for a molecule passing through the focal spot can be expressed as [169, 183]:

$$t = t_0 + \frac{\omega^2}{4D_{\text{eff}}}$$

where  $t_0$  is the offset derived from the FCS diffusion laws,  $\omega$  being the FCS beam waist that essentially defines the probe area, and  $D_{\text{eff}}$  being the effective mobility diffusion constant that depends on the probability of crossing the barriers, and the microscopic diffusion coefficients. This mobility constant also depends upon the density of domains in the case of isolated microdomains.

Free diffusion is characterized by a near zero y-intercept (*i.e.*,  $t_0 = 0$ ) for vanishing probe area as the curve crosses the origin. The presence of impermeable obstacles hinders the effective diffusion of the molecules and thus increases the transit time to cross through a given probe area. The slope of the FCS diffusion curve in such a case is higher, but still crossing through the origin. In contrast, the dynamic partitioning into nanodomains is characterized by a deviation of the y-intercept on the time axis from the origin (*i.e.*,  $t_0 > 0$ ), while a trapping into in a molecular mesh-work is revealed by a negative y-intercept (*i.e.*,  $t_0 < 0$ ) [172]. Using this approach, spot variation FCS (sv-FCS) have been demonstrated to study the transient confinement times of mobile tracers in the plasma membrane with minimum attainable spot size being the diffraction limit of the excitation light [183].

In this Chapter, we taking advantage of the nanoscale spatial resolution achieved by the nanogap antenna to establish the FCS diffusion laws with spatial resolution being as small as 10 nm. Combining FCS with resonant planar nanoantennas, we investigate the diffusion dynamics of phosphoethanolamine (PE) and sphingomyelin (SM) on the membranes of living Chinese hamster ovary (CHO) cells. The nanoantenna approach is straightforward to implement on any confocal microscope equipped with FCS as contrarily to STED, it does not require adding any supplementary illumination beam. Moreover, the need for high power density laser beams in order to push the minimum resolution achievable in STED makes it prone to photophysical damage and interfering with the dynamic biochemical processes in living cells. Using the extreme near field localization and superior optical performance achieved for fluorescence experiments, we now exploit the planar “antenna-in-box” devices for investigating plasma membrane organization in living cells.

Prior to the experiments with living cells, we discuss the FCS calibration experiments for planar nanoantenna by using a free dye Alexa647 using a 3D model. Nanoantenna calibration with model lipid bilayers (2D-diffusion) is also discussed, validating the use of the planar “antenna-in-box” devices for biological systems [62].

## 6.2 Diffusion time analysis: Free dye Alexa647 on planar “antenna-in-box”

In this section, we discuss the FCS calibration experiments with planar “antenna-in-box” devices by using the Alexa647 molecules with a known diffusion constant. As we will demonstrate, using a physically relevant model supported by the FDTD simulations, it is possible to describe the diffusion properties of Alexa647 molecules in the nanogap and retrieve the diffusion coefficient.

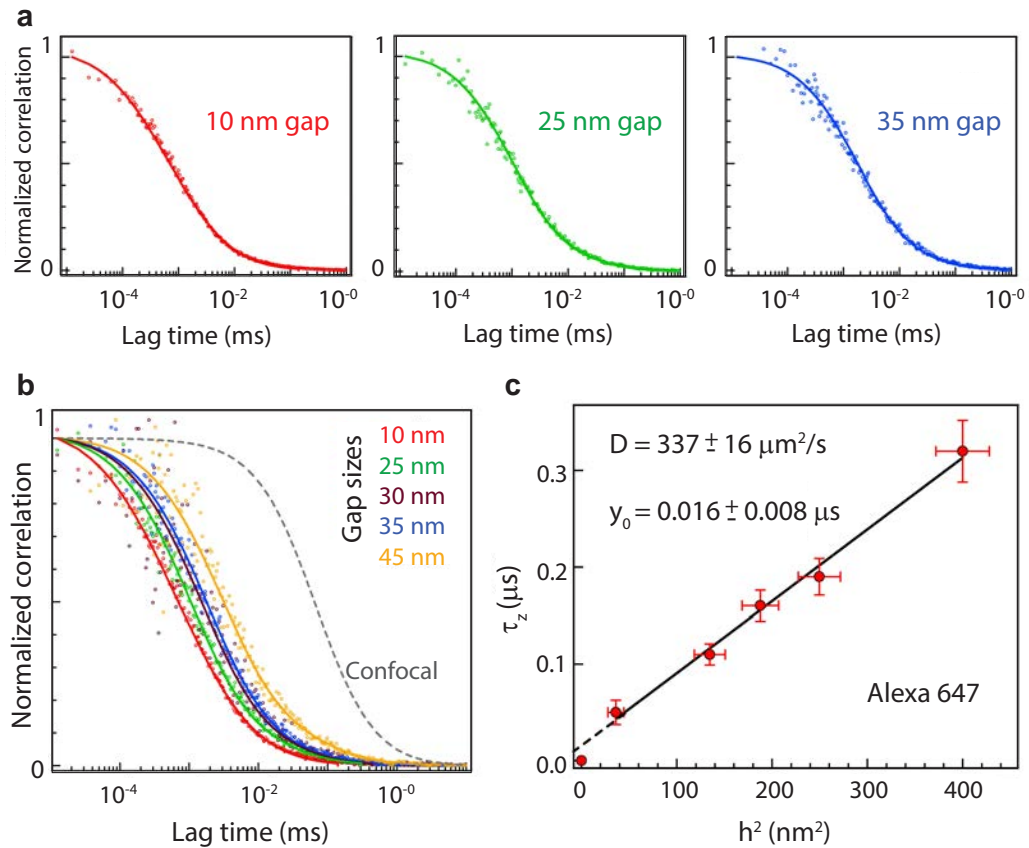


**FIGURE 6.2: FCS calibration diffusion time vs probe area for 3D diffusion of Alexa647.** (a) FCS correlation functions for three representative gap sizes (from left: 10 nm, 25 nm and 35 nm gap separation). Dots are the experimental data and lines being the two-component fit modeled by the Equation 6.1. (b) Normalized ACF’s showing the evolution in diffusion time scales for Alexa647 molecules with increasing gap separations. The confocal diffusion (in gray dotted line) is also shown for direct comparison. (c) FCS diffusion law for Alexa647 molecules shows negligible y-intercept at the origin, in agreement with unhindered Brownian diffusion. The linear fit retrieves the confocal diffusion constant  $D = 337 \pm 16 \mu\text{m}^2/\text{s}$  with linear correlation coefficient of 0.99649 very close to unity. The uncertainty on  $h^2$  considers a 0.7 nm uncertainty in the determination of the decay length (the mesh size is 1 nm for gaps 25-45 nm and 0.5 nm for gap 10 nm gap antenna)

Correlation curves from the FCS experiments presented in earlier Chapter 5, are further analyzed to study the evolution of the diffusion time with different gap antennas. In

brief, 26  $\mu\text{M}$  concentration of Alexa647 along with 200 mM methyl viologen in PBS solution are probed with excitation light along the dimer axis. Figure 6.2a shows raw (dots) and the fit (solid lines) for three different gap sizes (from left: 10 nm, 25 nm and 35 nm gap separations). The ACFs fitting involves a two-species model to take into account the tail component appearing at lag times  $> 10 \mu\text{s}$ :

$$G(\tau) = A \times G_{\text{TIRF}}(\tau) + (1 - A) \times G_{\text{3D}}(\tau) \quad (6.1)$$

where  $A$  is the amplitude of the main component,  $G_{\text{TIRF}}$  is the TIRF-FCS model and  $G_{\text{3D}}$  is the model for Brownian 3D free diffusion. We use the  $G_{\text{TIRF}}$  model as it accounts for the contribution from the nanogap with exponentially decaying intensity profile. The second  $G_{\text{3D}}$  component takes into account the residual fluorescence contribution from the surrounding box region.

$G_{\text{TIRF}}$  considers exponential decaying illumination profile along the  $z$  axis and lateral detection volume confinement with a confocal pinhole. Following the works by Starr [184] and Hassler [33, 185],  $G_{\text{TIRF}}(\tau)$  is derived as:

$$= \frac{1}{1 + (\tau/S_z^2 \tau_z)} \times \left[ (1 - \tau/2\tau_z) \times \exp(\tau/4\tau_z) \times \text{erfc}\sqrt{\tau/4\tau_z} + \sqrt{\tau/\pi\tau_z} \right] \quad (6.2)$$

where  $\tau/S_z = h^2/4D$  is the vertical diffusion time and  $S_z = d_{xy}/h$  is the shape parameter.  $h$  indicates decay length at  $1/e$  of the illumination intensity profile,  $D$  is the diffusion constant and  $d_{xy}$  is the lateral half-width at  $1/e^2$  of the illumination intensity profile.  $G_{\text{3D}}(\tau)$  is the regular model for Brownian free diffusion:

$$G_{\text{3D}}(\tau) = \frac{1}{1 + \tau/\tau_d} \times \frac{1}{\sqrt{1 + S_{xy}^2 \tau/\tau_d}}$$

where  $\tau_d = W_{xy}^2/4D$  is the lateral diffusion time,  $S_{xy} = W_{xy}^2/W_z$  is the shape parameter.  $D$  is the diffusion coefficient and the waist  $W_{xy}$  is half-width at  $1/e^2$  of the Gaussian detection volume.

During the ACF fitting procedure as modeled by the Equation 6.1,  $A$  is fixed to 0.9. This means that the amplitude of the 3D component (second component in the same equation) is at maximum only 10%. The shape parameter  $S_z$  for TIRF is fixed to  $S_z = 6$  except for the smallest gap (10 nm nominal) which requires  $S_z = 10$ . These values derived after empirical optimization of the fits are in correct agreement with the FDTD profiles (discussed in Chapter 5). The shape parameter for 3D diffusion is kept to the standard value for confocal  $S_{xy} = 0.2$  and has negligible influence on the fit result for

the TIRF component which is the main interest. Hence the remaining free parameters for optimization are  $\tau_z$  for  $G_{\text{TIRF}}$  and  $\tau_d$  for  $G_{3\text{D}}$ .

Figure 6.2b displays the raw correlation data (dots) and their corresponding fits (solid lines) for various gap size nanoantennas. Using the fit model that incorporates the TIRF component as the dominating factor in the diffusion of Alexa647 molecules in solution shows a very good fit to the experimental data. The detail fit results for all five different gap size nanoantennas is summarized in Table 6.1.

Gap size	$\tau_z$	$S_z$	$\tau_{xy}$	$S_{xy}$	A	h
10 nm	0.05 $\mu\text{s}$	10	10 $\mu\text{s}$	0.2	0.9	6 nm
25 nm	0.11 $\mu\text{s}$	6	26 $\mu\text{s}$	0.2	0.9	11.6 nm
30 nm	0.16 $\mu\text{s}$	6	32 $\mu\text{s}$	0.2	0.9	13.7 nm
35 nm	0.19 $\mu\text{s}$	6	31 $\mu\text{s}$	0.2	0.9	15.8 nm
45 nm	0.32 $\mu\text{s}$	6	90 $\mu\text{s}$	0.2	0.9	20 nm

TABLE 6.1: **FCS calibration results with Alexa647 diffusing in solution probed with increasing nanoantenna gap size.** Fitting of the ACF curves displayed in Figure 6.2 using Equation 6.1 with Alexa647 molecules probed with increasing gap sizes.  $\tau_z$  for the  $G_{\text{TIRF}}$  component and  $\tau_{xy}$  for the  $G_{3\text{D}}$  component are the only free parameters.

Finally from the results of the fit, we derive the ‘‘FCS diffusion law’’ representing  $\tau_z$  as a function of the decay length at  $1/e$  of the illumination intensity profile  $h$ . This represents the main contribution from the nanogap region (TIRF model). It is important to note that with  $S_z = 6$  (or 10), the contribution from the lateral diffusion along x and y (term  $\frac{1}{1+(\tau/S_z^2 \tau_z)}$ , the first term in Equation 6.2 for  $G_{\text{TIRF}}$  has a rather weak contribution, exemplified by its lateral diffusion time  $S_z^2 \tau_z$  which is  $6^2 = 36\times$  (or  $100\times$ ) longer than the  $\tau_z$ .

Figure 6.2c summarizes the calibration results on Alexa647 using this TIRF model.  $\tau_z$  (in y-axis) and probe area ( $h^2$  in x-axis) follow linearity with linear correlation coefficient being very close to unity ( $r = 0.99649$ ). The diffusion coefficient  $D$  is then determined from the slope of this ‘‘FCS diffusion law’’ using  $\tau_z = h^2/4D$ , with decay length ( $h$ ) at  $1/e$  (and not at  $1/e^2$ ) of the illumination intensity profile [33, 184, 185].  $h$  is deduced from the FDTD simulations, it’s not a free parameter. The derived diffusion coefficient  $D = 337 \pm 16 \mu\text{m}^2/\text{s}$  is in excellent agreement with the calibrated value for Alexa647 [186]. The linearity and near-zero intercept  $y_0$  confirm the nanoantenna is not introducing artifacts in the diffusion dynamics of the Alexa647 molecules.

It should be noted that for the smallest gap (desired 10 nm gap), the FDTD calculations are taken with 12 nm gap separations (instead of 10 nm) as this provides a better match and is consistent with the TEM characterization. In all the analysis hereafter (experiments with model lipid bilayers and living cells), the area for the smallest gap

nanoantennas will be thereby fixed at  $300 \text{ nm}^2$  (as we will further validate with model membranes).

### 6.3 Nanoantennas calibration with model lipid membrane

In addition to the experimental calibration of the probe areas by means of individual Alexa647 dyes diffusing in solution (3D-model), we now study the evolution in the diffusion time scales with increasing probe areas on pure model lipid bilayers (2D-model). This will independently validate the probe area calibration before the live cell experiments with full biological complexity.

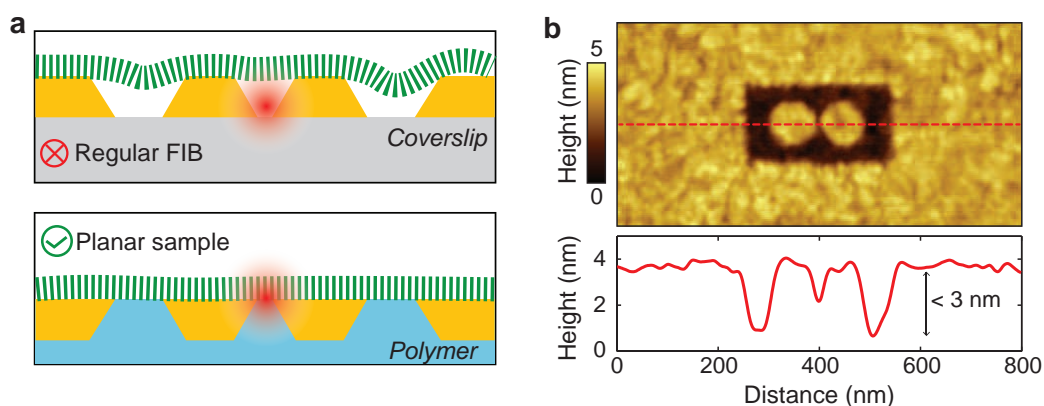


**FIGURE 6.3: Planar nanoantennas for membrane investigations.** (a) Schematic representations of the antenna geometry and cell membrane interface depicted without (as in conventional FIB) and with template stripping. The planar geometry allows easier access to the narrow and bright hotspot region and minimizes unwanted membrane curvature and distortion. (b) Detailed AFM image of a representative planar “antenna-in-box” with 10 nm nominal gap width and line profile showing a 3 nm total residual topography.

The fluorescence experiments with model lipid bilayer labeled deposited on top of the planar nanoantennas are depicted in Figure 6.3a. A highly confined nanometric illumination hotspot is created on the top surface of the nanogap region, which is in direct contact with the membrane region. Importantly, the planarization strategy avoids possible curvature induced effects on the cell membrane providing an ideal platform for live cell membrane research when compared to those structures obtained *via* FIB milling [179, 180]. Further, the AFM image in Figure 6.3b indicates a planarity better than 3 nm for the top surface of the nanoantennas.

Lipid bilayers are prepared by mixing unsaturated phospholipid 1,2-dioleoyl-*sn*-glycerol-3-phosphocholine (DOPC) dissolved at 1 mg/mL in chloroform:methanol (9:1) together with 0.01 mol% of the fluorescent dye DiD. The mixture of DOPC and fluorescence

dye is stored in small glass tubes at 4° C and is deposited on the clean nanoantenna substrates only prior to the fluorescence experiments. The fluorescently labeled DOPC is then allowed to dry for an hour in presence of a weak nitrogen flow which is then stored in vacuum for another additional hour. The samples are finally hydrated in PBS (pH 7.4), carefully rinsed to remove excess lipids and then immediately probed by FCS at room temperature. Nanoantennas are excited by focusing the excitation laser light ( $\lambda = 640 \text{ nm}$ ,  $\sim 2 \text{ kW/cm}^2$ ) into individual antennas using a water-immersion objective (NA = 1.2). Excitation along the dimer axis is used to achieve maximum field enhancement and ultra confined electromagnetic hotspot.

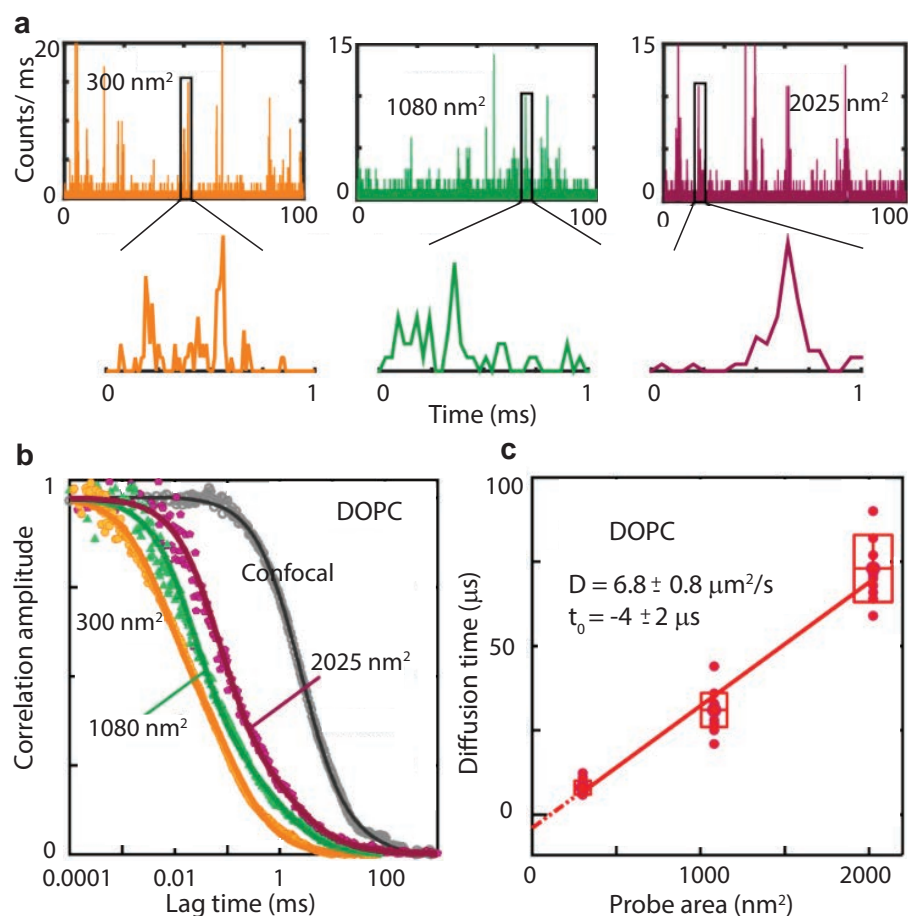


**FIGURE 6.4: Planar nanoantennas for model lipid bilayer.** (a) Representative fluorescence intensity time traces of DiD embedded in a pure DOPC bilayer for three different antenna gap areas together with enlarged views of representative bursts. (b) Normalized ACF curves as obtained with different nanoantenna probe areas and with confocal excitation. (c) Diffusion times as extracted from the ACF fitting as a function of the antenna gap area. Each dot corresponds to an individual ACF measurement in a single antenna. Number of measurements: 13, 8 and 12 for 300 nm<sup>2</sup>, 1080 nm<sup>2</sup> and 2025 nm<sup>2</sup> antenna probe areas respectively.

Figure 6.4 shows the representative fluorescent intensity time traces (a) and the corresponding normalized ACFs (b) of DiD diffusion in a pure DOPC membrane over three

probe area	1 <sup>st</sup> component		2 <sup>nd</sup> component	
	time ( $t_1$ )	amplitude ( $\rho_1$ in %)	time ( $t_2$ )	amplitude ( $\rho_2$ in %)
300 nm <sup>2</sup>	6 ± 1 μs	67 ± 3	170 ± 150 μs	33 ± 8
1080 nm <sup>2</sup>	25 ± 3 μs	79 ± 8	1.4 ± 0.2 ms	21 ± 7
2025 nm <sup>2</sup>	71 ± 25 μs	75 ± 9	1.6 ± 0.3 ms	25 ± 10

TABLE 6.2: **Fitting of the ACF curves on DOPC bilayers for different antenna gap areas.** Fitting of the ACF curves on DOPC bilayers for different antenna gap areas. The shortest times ( $t_1$ ) correspond to the diffusion times of DiD through the antenna hotspot regions while  $t_2$  corresponds to residual excitation of the dye inside the box-aperture.

different antenna probe areas. The probe areas are estimated by using the product of the gap size (as measured with TEM characterization) by the full width at half maximum for the intensity profile along the direction perpendicular to the nanoantenna major axis. Thus, the nanoantennas with 10, 30 and 45 nm nominal gap sizes correspond to the illumination areas of  $300 \pm 50$  nm<sup>2</sup>,  $1080 \pm 80$  nm<sup>2</sup> and  $2025 \pm 110$  nm<sup>2</sup>. The estimated probe areas were also validated by using a free dye Alexa647 molecules.

As shown in Figure 6.4a, the fluorescence burst duration increases with gap area, confirming that the detected signal arises from the excitation of the dye diffusing at the nanometric gap regions. The normalized ACFs in Figure 6.4b shows the evolution of the diffusion timescale for different gap nanoantennas (colored lines) and compares with the confocal case (in gray). The characteristic diffusion times for nanoantenna experiments are derived by fitting the ACF curves following the equation [62]:

$$G(\tau) = \sum_{i=1}^{n_{\text{diff}}} \frac{\rho(i)}{1 + \left[ \frac{\tau}{\tau_{\text{diff}}(i)} \right]} \quad (6.3)$$

where  $\tau_{\text{diff}}(i)$  the average residence time of the  $i^{\text{th}}$  diffusing modality,  $\rho(i)$  denotes the respective amplitude contribution. As the diffusion in lipid bilayers is 2D, we do not need to follow the same procedure as used for 3D diffusion of Alexa647 molecules in solution. The complete derivation of the correlation function for both 3D and 2D diffusion cases are already discussed in Chapter 2.

Consistence with our earlier experiments with nanoantennas, we adopt two-component 2D Brownian fittings to account for both, direct excitation from the gap region and residual excitation of DiD diffusing through the box-aperture. Using Equation 6.3, the main component of the fitted curves displayed in Figure 6.4b, render diffusion time scale of  $(6 \pm 1)$  μs,  $(25 \pm 3)$  μs and  $(71 \pm 25)$  μs respectively for 300, 1080 and 2025 nm<sup>2</sup> and should be compared with the 3.5 ms diffusion time for confocal excitation (gray

circles). The detailed results of the fitting procedure and relative contributions of each component (from the gap and box-aperture excitation) are listed in Table 6.2.

Figure 6.4c shows the diffusion times obtained from multiple measurements on individual nanoantenna as a function of the probe area. The diffusion times versus probe areas is well-fitted to a straight line with an intercept close to the zero-origin point, indicating that  $\tau_{\text{DOPC}}$  scales linearly with the probe area, consistent with free Brownian diffusion of the dye in the pure DOPC membrane. It also confirms that the DOPC bilayers are homogenous down to the nanoscale and the slope of the fitting rendered a diffusion coefficient of  $(6.8 \pm 0.5) \mu\text{m}^2/\text{s}$  compares well to our confocal measurements and values reported elsewhere [187]. These results on pure DOPC validate the application of planar plasmonic nanoantennas to record the diffusion of individual molecules in lipid bilayers with microsecond time resolution.

## 6.4 Atto647N-labeling and experimental strategy on living cells

After the calibration experiments with freely diffusing Alexa647 molecules (3D model) and the validation with a mimetic system (DOPC bilayers as a 2D model), we now perform live cell experiments with Chinese hamster ovary (CHO) cells. CHO cells are seeded on a coverslip containing arrays of nanoantennas with two different gaps: 10 nm and 35 nm (see Figure 6.5). As the experiments on living cells membranes are very time consuming (for both data recording and subsequent time trace analysis), we decide to focus our attention on two specific gap sizes and record many different antennas and cells. All the live cell experiments are complete within the first 30 minutes from the time of incorporation of fluorescent lipid analogs into the plasma membranes to avoid artifacts arising from dye internalization in living cells.

Lipid conjugates are separately prepared by labeling 1,2-dipalmitoyl-sn-glycero-3-phosphoethanolamine (PE) and sphingomyelin (SM) with the organic dye Atto647N (from Invitrogen) following the protocol described in Ref. [174]. The fluorescence spectrum of Atto647N is displayed in Figure 6.6 along with the nanoantenna resonance measured by dark field spectroscopy. The excellent spectral overlap is desired to achieve maximize fluorescence enhancement. The cells are incubated on the nanoantenna substrates at 37° C in a controlled atmosphere with 5% of CO<sub>2</sub> for nearly 48 hours prior to the experiments to allow them to freely grow and adhere onto the antenna platform (see Figure 6.7). The planar antenna platform contains multiple gold nanoantenna arrays with nominal gap sizes of 10 nm and 35 nm on which a circular cell culture well is

mounted for live CHO cell culturing. Figure 6.7a depicts the strategy chosen for the fluorescence live cell experiment conducted on the nanoantenna platform.

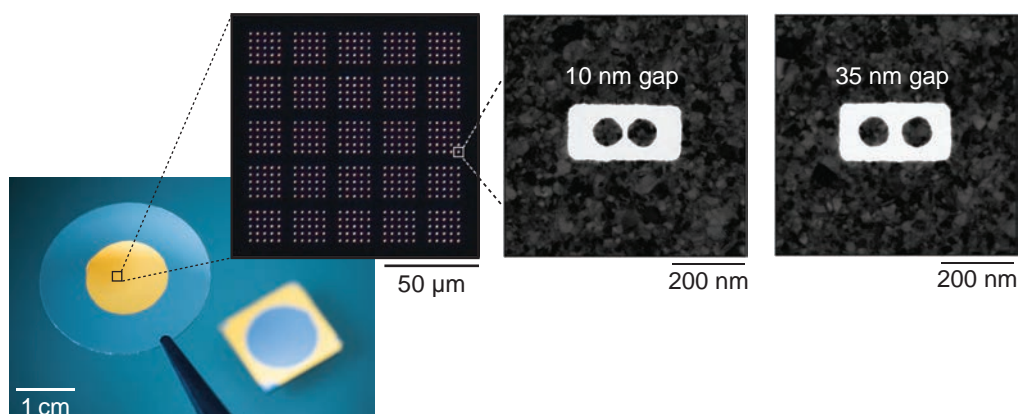


**FIGURE 6.5: Large-scale antenna arrays and TEM images.** From left to right: macro-photograph of a coverslip with a stripped Au film with large-scale planar antenna arrays; dark field optical micrograph of a small portion of the antenna arrays showing here 625 antennas with 10 nm nominal gap size; transmission electron microscope (TEM) images of antennas with 10 and 35 nm gap size.

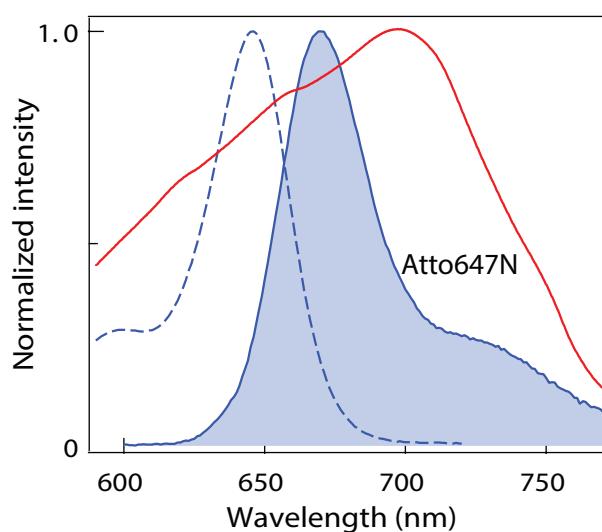


**FIGURE 6.6: Overlap between antenna's resonance and Atto647N fluorescence spectra.** Overlap of the dark-field scattering spectrum recorded for a 10 nm gap antenna (red line, illumination polarization along the nanoantenna dimer major axis) with the fluorescence spectra for Atto647N (blue lines). The excitation spectrum is displayed in with a dashed line and the solid shaded line represents the emission spectrum.

Prior to the fluorescence experiments, separately prepared lipid analogues (either PE or SM with the organic dye Atto647N) are incorporated in the cell membrane during a 3 minute incubation period at room temperature, dissolved in the corresponding medium for CHO cells (Ham's F12 nutrient mixture). Stained cell cultures are rinsed to remove

residual dye molecules before placing the sample coverslip on the piezo-stage of an inverted microscope to carry out the measurements as in the case of model lipid membranes. All fluorescence staining are performed at a  $\sim 300$  nM concentration of Atto647N and the measurements being completed within 30 minutes after the incorporation of the fluorescent analogs into the plasma membranes. Due to the incorporation within the limited 3 minutes time and subsequent washing step, the concentration of fluorescent lipids in the cell membrane is significantly less. From the number of detected fluorescence bursts and the FCS amplitude (as we will show in next section), we estimate that the density of fluorescent lipids for the nanoantenna experiments is on the order of 20 - 80 probes per  $\mu\text{m}^2$ . Figure 6.7b shows a representative confocal image of the morphology of the CHO cells adhered on a glass coverslip taken after the incorporation of the fluorescent lipid analogs.

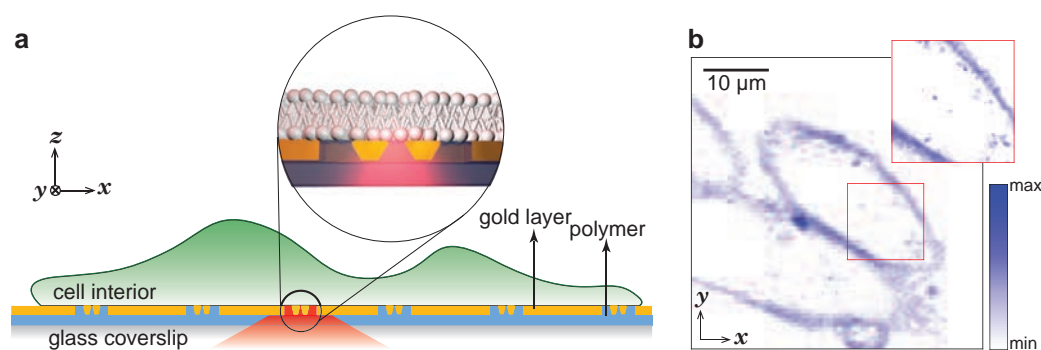


**FIGURE 6.7: Planar nanoantennas for investigating membrane dynamics in living cells.** (a) CHO cells are seeded onto a microscope coverslip containing multiple planar nanoantennas with 10 and 35 nm gap sizes. The inset shows the cross section of the “antenna-in-box” stripped and embedded into a polymer, bringing the region of maximum electromagnetic field intensity onto the surface in direct contact with the plasma membrane of living cells. (b) Confocal image of CHO cells showing the morphology after incorporating the fluorescent SM lipid analog labeled with Atto647N.

## 6.5 Experiment and results: Membrane dynamics in living cells

The fluorescence experiments are performed with a commercial MicroTime 200 setup equipped with an inverted confocal microscope (Olympus 60 $\times$ , 1.2 NA water-immersion objective) and a three-axis piezoelectric stage (PhysikInstrumente, Germany) allowing to select individual nanoantennas. A linearly polarized 640 nm picosecond laser diode (Pico-Quant LDH-D-C-640) in continuous wave mode is used to resonantly excite individual nanoantennas. The emitted fluorescence signal is collected in epi-detection mode through a dichroic mirror and the signal is finally split into two avalanche photodiodes

(PicoQuant MPD-50CT). An emission filter and a band pass 650-690 nm filter just before each detectors eliminate the scattered light by the excitation laser. A 30  $\mu\text{m}$  pinhole in the detection arm yields a 0.5 fL confocal detection volume at the sample plane. The fluorescence time traces are recorded on a fast time-correlated single photon counting module in the time-tagged time-resolved mode (PicoQuant MPD-50CT). All the fluorescence measurements are performed by illuminating the sample at an excitation power density of  $\sim 2\text{-}3 \text{ kW/cm}^2$ . The measurements are acquired for a typical run time of 50 s and the correlation amplitudes computed for  $\sim 20$  s windows with the commercial software package SymPhoTime 64. The detailed optical setup for the FCS experiments with cells (performed at ICFO, Barcelona) is described in Chapter 2.

### 6.5.1 Burst analysis of PE and SM on living cells

Single-molecule fluorescence time traces are acquired in the Tagged Time-Resolved (TTTR) mode (recording each event at its arrival time) with 4 ps temporal resolution. Figure 6.8 shows representative single-molecule fluorescence time traces for PE and SM in the confocal (a,b) and in the nanoantenna configuration (c,d). The spatial resolution set by the diffraction limited spot in the confocal scheme (usually 300 nm) does not allow to resolve heterogeneities that may occur at the nanometric spatial scale. Hence we observe the indistinguishable time traces for both PE and SM. In contrast, the highly confined surface hotspot originating from the 10 nm gap antenna clearly reveals the difference in the characteristic diffusion dynamics of PE and SM (c,d). As shown in Figure 6.8c, PE displays sharp peaks in the fluorescence time trace as a result of the sub-diffraction excitation hotspot created by the planar nanogap antenna. Unlike PE, the signature of SM is discernibly different at the nanoscale: the short bursts (hallmark of free diffusion in ultra-small detection areas) are accompanied by high intensity bursts of significantly longer durations. This is a direct indication that the nanoscopic diffusion of SM on the plasma membrane is deviating from free Brownian diffusion as compared to larger macroscopic scales.

To provide more quantitative information about the fluorescence time traces, we perform fluorescence burst analysis to represent the distributions of burst duration versus burst intensity. Fluorescence bursts analysis is carried out with a likelihood-based algorithm to test the null hypothesis (no burst, recording compatible with background noise) against the hypothesis that a single-molecule burst arises as a consequence of a molecule crossing the excitation area. The background threshold is set to 20-30 counts/ms following an empirical optimization [147, 188].

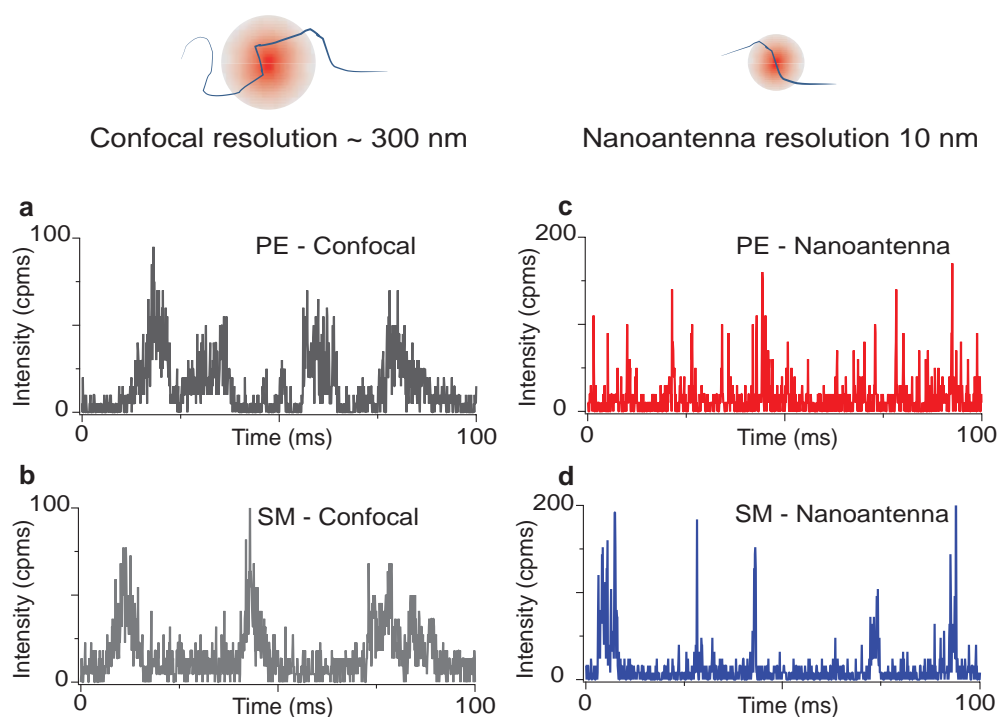


**FIGURE 6.8: Single-molecule fluorescence time traces in living CHO cells.** Fluorescence time traces for phosphoethanolamine (PE: a,c) and sphingomyelin (SM: b,d) labeled with Atto647N recorded with confocal (left) and with a 10 nm gap planar nanoantenna (right). The binning time is 0.1 ms for all traces. The diffraction-limited spot in the confocal configuration cannot resolve the nanoscopic and heterogeneous membrane organization, this results in indistinguishable fluorescence time traces for both PE and SM (a,b). In contrast, the confined nanoantenna hotspot reveals clear differences in the diffusion dynamics of PE and SM (c,d).

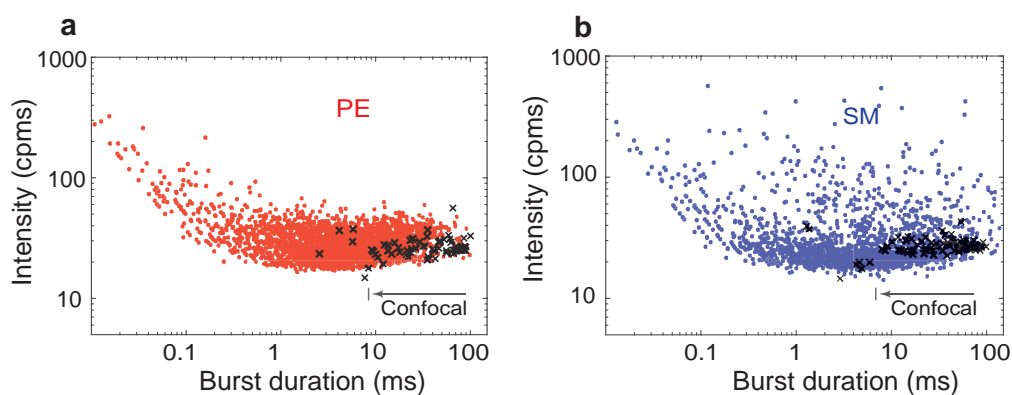


**FIGURE 6.9: Single-molecule burst analysis for PE and SM.** The fluorescence time traces are analyzed to produce scatter plots showing the distribution of fluorescence burst intensity versus burst duration. Single-molecule events (PE in a and SM in b) in sub-ms time scales are observed with nanoantennas (color dots) as the confined electromagnetic hotspots allow to probe the dynamics occurring beyond the diffraction limit. Single-molecule events obtained with confocal illumination are displayed for comparison (black dots).

Figure 6.9 shows the results for both PE (a) and SM (b) for the 10 nm nanogap antenna (colored dots) compared to the confocal configuration (black cross). The scatter plots for PE and SM in the confocal configuration show no visible differences with burst durations in the range 5-100 ms and intensities around 20-30 counts/ms. However, in stark contrast, the distributions obtained on the nanoantennas show clear differences between PE and SM. Diffusion events in sub-ms time scales are notably observed with the nanoantennas exhibiting burst durations as short as 10  $\mu$ s. Such short events are more than two orders of magnitude faster than in the confocal reference. Regarding the diffusion dynamics for PE (red dots) probed with the nanogap antennas a general trend can be deduced, namely, brighter events arise at shorter timescales. These can be understood as the detection of a “best burst event” directly resulting as a consequence of an individual molecule diffusing through the hotspot in the optimal position and orientation for maximum enhancement. The tighter the excitation beam confinement, the higher is the local intensity which leads to high fluorescence counts with short burst duration. We thus relate the events with burst durations  $< 1$  ms to the trajectories occurring within the nanogap region [147]. In the case of PE, the bursts with durations above 1 ms feature a lower intensity in the range of 20-70 counts/ms, which is only slightly increased as compared to the confocal case (black cross). We assign these longer burst duration events to the residual excitation of diffusing molecules within the larger  $300 \times 140$  nm<sup>2</sup> box aperture region where the electromagnetic field intensity enhancement is negligible and is thus comparable to the confocal reference.

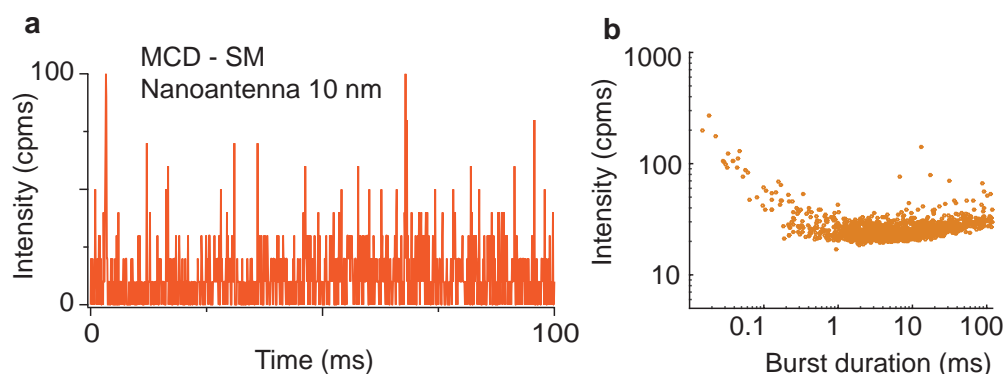


**FIGURE 6.10: Representative time trace of SM after cholesterol depletion.** (a) Representative single-molecule time trace of Atto647N for SM after cholesterol depletion with 10 nm gap planar “antenna-in-box” platform (binning time 0.1 ms). (b) The scatter plots showing the distribution of representative bursts (#1587) recorded for the same is shown alongside. Cholesterol induced hindrance in diffusion of SM molecules is avoided with incorporation of the MCD in the plasma membranes.

In contrast to PE, SM probed with the nanoantenna arrays shows a significantly broader

distribution of burst lengths against peak burst intensities (Figure 6.8d). High intensities are also observed for burst durations above 1 ms. Since these events are not observed for PE, we relate their occurrence to nanoscopic heterogeneities such as transient molecular complexes on the cell membrane hindering the diffusion of SM. To support this conclusion, next we perturb the cholesterol composition in the cell membrane with methyl- $\beta$ -cyclodextrin (MCD) as cholesterol is expected to play a significant role in the formation and stability of the lipid nanodomains. For cholesterol depletion, the CHO cells are incubated in serum free buffer with 10 mM methyl- $\beta$ -cyclodextrin (MCD) for 30 minutes at 37°C, and the fluorescent labeling is then carried out as described previously. The result of the burst analysis for SM after MCD treatment (Figure 6.10) recovers a distribution which closely resembles the one for PE (see Figure 6.9a). In other words, the intense bursts of duration between 0.1 and 10 ms disappear after cholesterol depletion, consistent with the loss of nanodomains. Altogether, the results from the fluorescence burst analysis demonstrate the benefits of planar nanogap antennas to explore the nanoscopic organization of lipids in live cell membranes. Clear differences between PE and SM diffusion dynamics are unveiled that otherwise would remain hidden in the confocal measurements.

### 6.5.2 FCS in ultra confined illumination hotspots

To further support the burst analysis results, we performed fluorescence correlation spectroscopy analysis. We use two different gap sizes (10 and 35 nm) to quantify the lipid dynamics for increasing detection areas in the plasma membranes of living CHO cells. The mobility of molecules shows strong dependence on the local environment and thus in living systems the concept of ideal Brownian diffusion may not always hold true. Considering possible anomalous diffusion in living cells, the temporal correlation of the fluorescence intensity  $F$  can be written as [171]:

$$G(\tau) = \sum_{i=1}^{n_{\text{diff}}} \frac{\rho(i)}{1 + \left[ \frac{\tau}{\tau_{\text{diff}}(i)} \right]^{\alpha(i)}} \quad (6.4)$$

where  $\tau_{\text{diff}}(i)$  the average residence time of the  $i^{\text{th}}$  diffusing modality,  $\rho(i)$  denotes the respective amplitude contribution and  $\alpha(i)$  being the anomaly parameter of the same. We find that the FCS curves recorded with nanoscopic illumination can only be fitted with a model assuming two different diffusion modalities (*i.e.*,  $n_{\text{diff}} = 2$ ). Two-species model is important to fit the FCS data in order to account for the fluorescence contributions stemming from the nanogap and from the residual excitation stemming from the surrounding box-aperture. A key feature in FCS is that the molecules contribute to the correlation amplitude in proportion to the square of their fluorescence brightness, hence

the signal from molecules in the nanogap experiencing maximum enhancement will have a dominating contribution in the FCS curves [151].

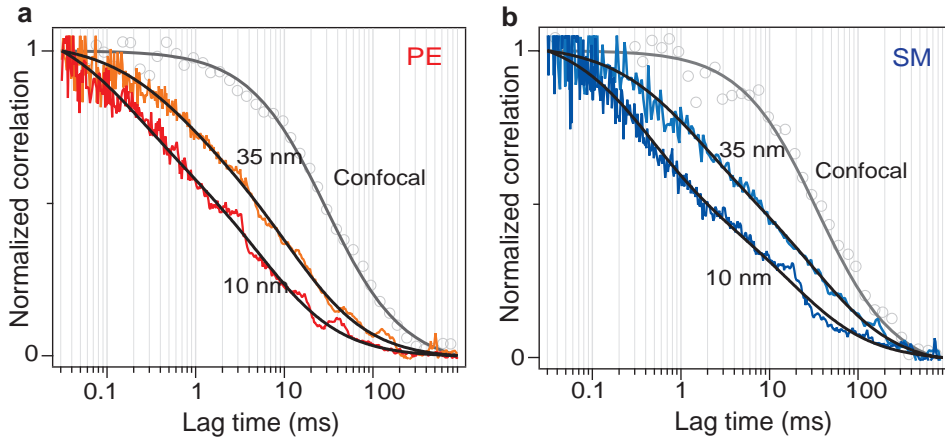


**FIGURE 6.11: Nanoantenna FCS with varying gap sizes on living cell membranes.** Normalized fluorescence correlation curves for Atto647N labeled PE (a) and SM (b) lipid analogs probed with nanoantennas of varying gap size. The color lines are experimental data and the black curves are numerical fits. The diffraction-limited confocal measurements are shown in gray for direct comparison.

component	PE - 10 nm		PE - 35 nm	
	1 <sup>st</sup>	2 <sup>nd</sup>	1 <sup>st</sup>	2 <sup>nd</sup>
time (t)	$0.25 \pm 0.06$ ms	8 ms	$0.75 \pm 0.15$ ms	16 ms
anomaly ( $\alpha$ )	0.85	1	0.8	1
amplitude ( $\rho$ in %)	$53 \pm 4$	$47 \pm 5$	$50 \pm 3$	$50 \pm 5$

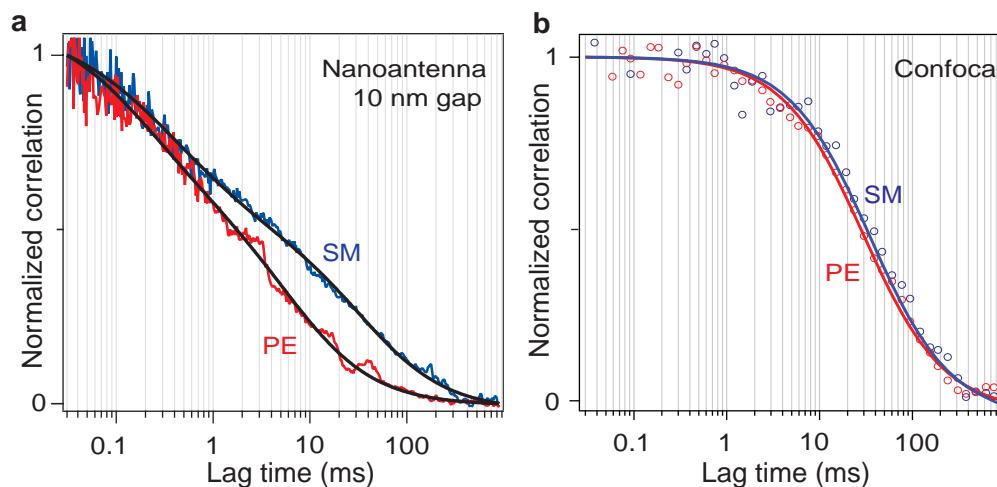
**TABLE 6.3: Fitting parameter results for PE in Figure 6.11a for two different gap sizes.**

component	SM - 10 nm		SM - 35 nm	
	1 <sup>st</sup>	2 <sup>nd</sup>	1 <sup>st</sup>	2 <sup>nd</sup>
time (t)	$0.35 \pm 0.04$ ms	17 ms	$1.4 \pm 0.2$ ms	45 ms
anomaly ( $\alpha$ )	0.65	1	0.85	1
amplitude ( $\rho$ in %)	$80 \pm 2$	$20 \pm 1$	$55 \pm 5$	$45 \pm 6$

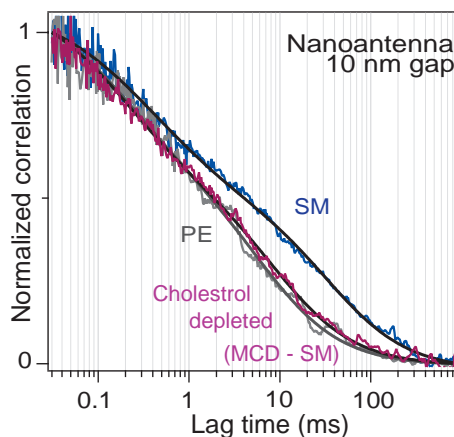
**TABLE 6.4: Fitting parameter results for SM in Figure 6.11b for two different gap sizes.**

Figure 6.11 shows the normalized correlation curves for PE (a) and SM (b) in case of the nanoantennas and the confocal reference. Similar to the burst analysis, we find no significant differences between the FCS curves for PE and SM for the confocal reference, yielding comparable diffusion times of  $25 \pm 4$  ms (PE) and  $30 \pm 4$  ms (SM), respectively. In the case of the nanoantennas, we observe that decreasing the gap size leads to a faster diffusion, confirming that the fluorescence signal stems from the nanogap region.

The differences between PE and SM diffusion dynamics are highlighted in Figure 6.12a where a direct comparison of the FCS data for the 10 nm gap antenna is shown for



**FIGURE 6.12: Hindered diffusion in SM as revealed by the nanoantenna-FCS.** (a) Comparison of FCS curves for PE and SM for a 10 nm gap antenna reveals clear differences between the dynamics of PE and SM at the nanoscale. (b) The confocal reference however shows no significant differences between the FCS curves for PE and SM yielding comparable diffusion times of  $25 \pm 4$  ms (PE) and  $30 \pm 4$  ms (SM), respectively. The color circles are experimental data and the lines are numerical fits described with single species Brownian diffusion.



**FIGURE 6.13: Cholesterol depleted SM indicates loss of nanodomains.** Normalized fluorescence correlation curves for Atto647N labeled SM (blue) and cholesterol depleted SM (Purple) for a 10 nm gap antenna. After cholesterol depletion, the SM diffusion dynamics are significantly faster and resemble the PE case (overlay in gray).

10 nm	1 <sup>st</sup> component			2 <sup>nd</sup> component		
	time (t)	anomaly ( $\alpha$ )	amplitude ( $\rho$ in %)	time (t)	anomaly ( $\alpha$ )	amplitude ( $\rho$ in %)
PE	$0.25 \pm 0.06$ ms	0.85	$53 \pm 4$	8 ms	1	$47 \pm 5$
SM	$0.35 \pm 0.04$ ms	0.7	$59 \pm 4$	38 ms	1	$41 \pm 5$
MCD-SM	$0.19 \pm 0.03$ ms	0.85	$53 \pm 4$	10 ms	1	$47 \pm 4$

**TABLE 6.5: Fitting results for PE, SM and MCD-SM with 10 nm gap antenna displayed in Figure 6.13**

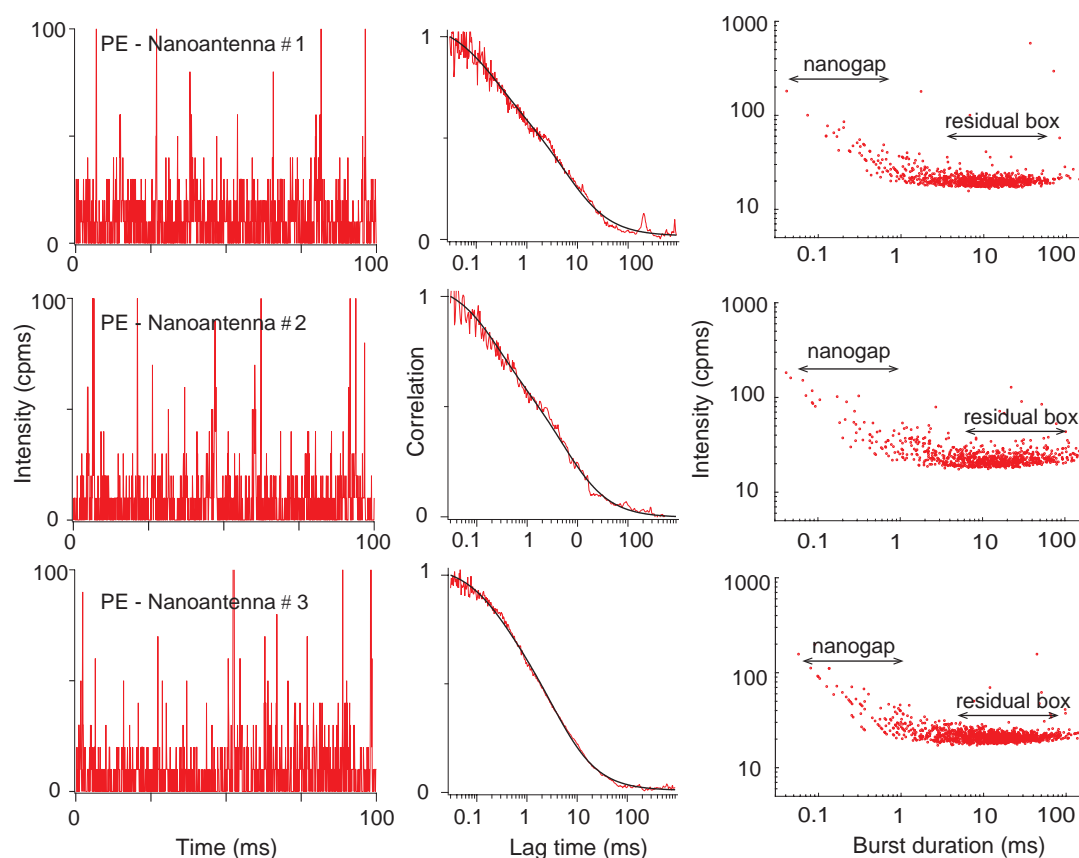


**FIGURE 6.14: Examples of PE-nanoantenna showing excellent reproducibility.** The representative time traces (binning time 0.1 ms), correlation curves and the scatter plots for three different 10 nm gap antenna is shown. In all cases Atto647N with PE is recorded with excitation light along the dimer axis. The correlation curves shows sub-ms diffusion dynamics and the scatter plots (#866 for Nanoantenna-1, #834 for Nanoantenna-2, #1364 for Nanoantenna-3) further indicate no hindrance.

both the fluorescent lipid analogs. Contrary to the confocal case (see Figure 6.12b), the difference in diffusion times between the two lipids becomes more prominent at the nanoscale, with PE exhibiting diffusion times of  $0.25 \pm 0.06$  ms and SM of  $0.35 \pm 0.04$  ms. The complete results and values for the FCS fits are detailed in Table 6.3 and Table 6.4. Moreover, after MCD treatment, the diffusion dynamics for cholesterol-depleted SM closely resembles that of PE with a diffusion time of  $0.19 \pm 0.03$  ms (Figure 6.13, and see Table 6.5). These FCS results confirm the presence of cholesterol-enriched nanodomains hindering the diffusion of SM, in agreement with the results found for the fluorescence burst analysis.

In addition, the anomaly parameter ( $\alpha$  in Equation 6.4) retrieved for SM depends on the probe area, deviating from unity as the illumination area reduced, from a  $\sim 0.85$  (for the 35 nm gap) to a  $\sim 0.65$  (for the 10 nm gap), which is again consistent with hindered diffusion (see Tables 6.3, 6.4, and 6.5). In contrast, the  $\alpha$  values are large and

close to unity for both the PE and cholesterol depleted SM cases ( $\alpha = 0.85$ ), display no dependency with the probe areas, as one would expect for unhindered diffusion scenario.

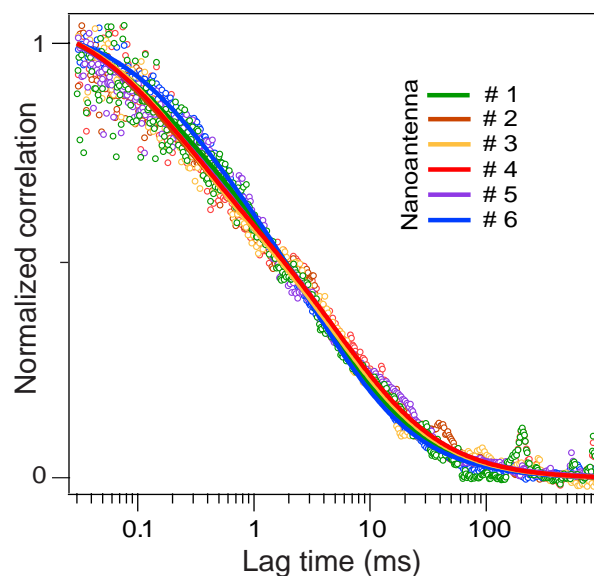


**FIGURE 6.15: Correlation curves recorded for PE-nanoantenna on different cells.** The FCS correlation curves for six different 10 nm gap antenna and different cells is shown. In all cases Atto647N with PE are recorded with excitation light along the dimer axis and the correlation curves indicate sub-ms diffusion dynamics.

Moreover, these planar nanoantennas show excellent reproducibility in terms of optical performance. Figure 6.14 shows some additional fluorescent time traces, burst analysis and the corresponding correlation curves for PE case when probed with 10 nm gap planar “antenna-in-box” devices. Moreover, Figure 6.15 displays the FCS curves recorded for PE and overlaid for six different nanoantennas and different cells confirming sub-ms temporal resolution achieved with 10 nm gap antennas.

### 6.5.3 Extending FCS diffusion laws at the nanoscale

To further analyze and exploit the FCS data we take advantage of the large number of planar nanoantennas with controlled gaps to carry out a FCS analysis over many different antennas and cells. As discussed earlier for Alexa647 molecules (3D) and DOPC bilayers (2D), this approach follows the so-called FCS diffusion law, which is a representation of the diffusion time versus the detection area [52, 169]. Extrapolation of the experimental curve to the intercept with the time axis provides information on the type of diffusion exhibited by the molecule, *i.e.*, free diffusion is characterized by a linear curve crossing the origin (0,0), while hindered diffusion due to the occurrence of nanodomains leads to a positive intercept on the time axis [52, 169].

Figure 6.16 summarizes the characteristic diffusion times for PE, SM and SM after cholesterol depletion for two antenna probe areas. From these graphs we derive the following three values plot in Figure 6.17: the diffusion coefficient (from the slope), the time axis intercept (by extrapolating the linear fit for vanishing probe area) and the normalized spread in the data points (defined as the width of upper and lower quartiles divided by the median value). As the diffusion time proportionally scales with the detection area, the diffusion coefficient  $D$  is retrieved from the slope of the linear fit matching the measured transient diffusion times obtained from the FCS curves versus the effective detection areas according to the relation  $D = \text{probe area}/4 \times \tau_{\text{diff}}$  [171].

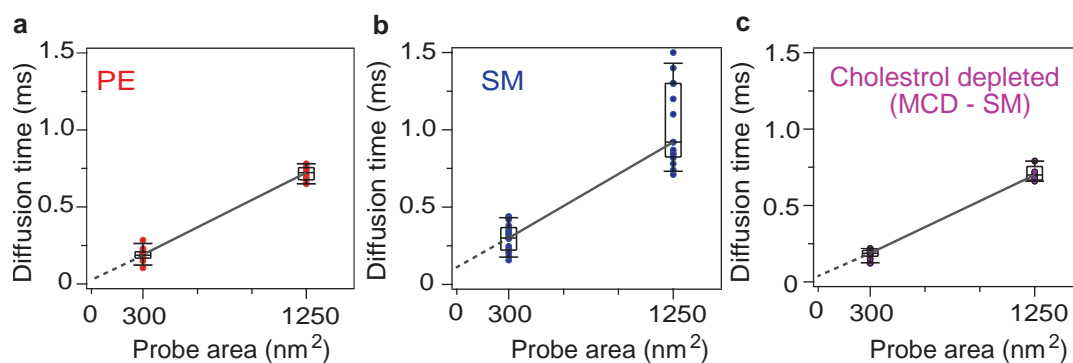


**FIGURE 6.16: Characteristic diffusion dynamics of membrane lipids probed with ultra-confined nanoantenna hotspots.** The diffusion time measured by FCS (for 60 different nanoantennas) is plotted as a function of the probe area for PE (a), SM (b), and SM after MCD treatment (c). The solid lines are linear fits through the median values. In the case of free diffusion, the origin (0, 0) is aligned with the expected line, while a positive intercept at the y-axis denotes hindered diffusion due to nanodomains.

The diffusion coefficients derived from nanoantenna measurements are  $D_{\text{PE}} = 0.44 \pm 0.07 \mu\text{m}^2/\text{s}$ ,  $D_{\text{SM}} = 0.38 \pm 0.19 \mu\text{m}^2/\text{s}$  and  $D_{\text{MCD-SM}} = 0.46 \pm 0.07 \mu\text{m}^2/\text{s}$  (Figure 6.17a) and they are consistent with the confocal measurements and values reported independently using STED-FCS [174]. It should be noted that these diffusion coefficients represent the diffusion time in the lipidic region between the nanodomains, with an additional contribution from diffusion within the nanodomains. In addition, diffusion of the nanodomains and the contributions for the membrane height fluctuations might also have some contribution in the measured time-scales.

Extrapolating the fits in Figure 6.16a-c towards diminishing probe area leads to the intercepts with the time axis as summarized in Figure 6.17b. The almost zero intercept hitting the origin observed for PE confirms the expected free Brownian motion diffusion mode. In contrast, SM features a positive y-intercept of about  $100 \mu\text{s}$ , which highlights a significant deviation from free Brownian diffusion and the occurrence of nanoscopic domains hindering SM diffusion. Depletion of cholesterol results in SM diffusion with a close-to-zero time intercept, demonstrating the crucial role of cholesterol establishing

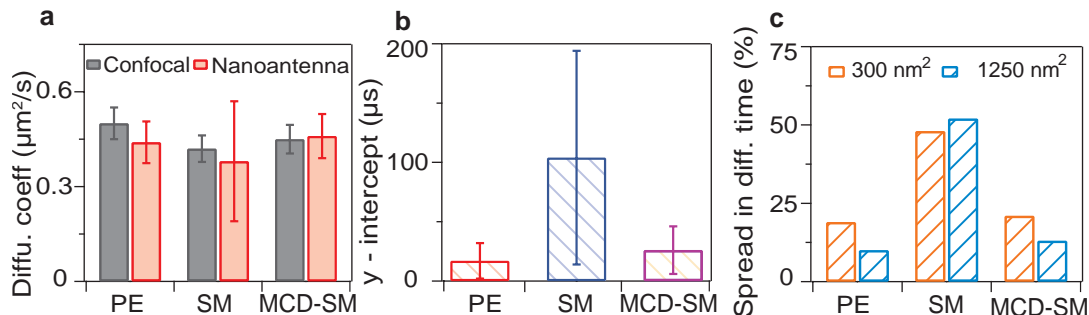


**FIGURE 6.17: Diffusion laws discussion at the nanoscale.** (a) The diffusion coefficients computed from the slopes in Figure 6.16 are compared with confocal results. (b) y-axis intercept deduced from the linear fits in the Figure 6.16a-c. PE and MCD-treated SM show near-zero y-intercept consistent with free diffusion, while the significant y-intercept for SM indicates that the diffusion is constrained by nanodomains. (c) Normalized spread in diffusion time (width of upper and lower quartiles / median) in each case. The large dispersion observed in SM is another indication that sphingolipids are preferentially recruited into transient nanoscopic domains.

the nanodomains and hindering SM diffusion. Such small nanoscale heterogeneities have never been detected so far with confocal microscopy, although STED-FCS down to 1000 nm<sup>2</sup> detection area could indicate clues about their occurrence. Our results are fully aligned with these previous findings and importantly, we further reduce the detection areas down to 300 nm<sup>2</sup>.

Lastly, we take a closer look at the degree of statistical dispersion of the obtained transient trapping times scattered around the median value for each probe area (Figure 6.17c). The spread in diffusion times for PE and SM after MCD treatment remains well under 25% and can be partially explained by variations of the gap size stemming from the nanofabrication process [62]. However, we observe for SM diffusion a significantly higher dispersion of the data (around 50%) which is specific to this lipid analog. These results are fully consistent with the presence of transient cholesterol-enriched nanodomains affecting SM diffusion. To further support these conclusions, we take advantage of the confocal data to represent a third point (see Figure 6.18) and show nice alignment with the nanoantenna data.

Altogether, our results provide compelling evidence for the existence of highly transient and fluctuating nanoscale assemblies of sterol and sphingolipids in living cell membranes. These experimental observations stand in excellent agreement with the notion that without stabilizing proteins, lipid rafts can be viewed as intrinsic nanoscale membrane heterogeneities that are small and highly transient [154, 158, 159, 161]. We estimate the characteristic residence time of the fluorescent SM lipid analogs in the nanodomain from the y-intercept in Figure 6.16b and Figure 6.17b, and find a value  $\sim 100 \mu\text{s}$ . The typical size of the nanodomains could in principle also be deduced from the FCS diffusion

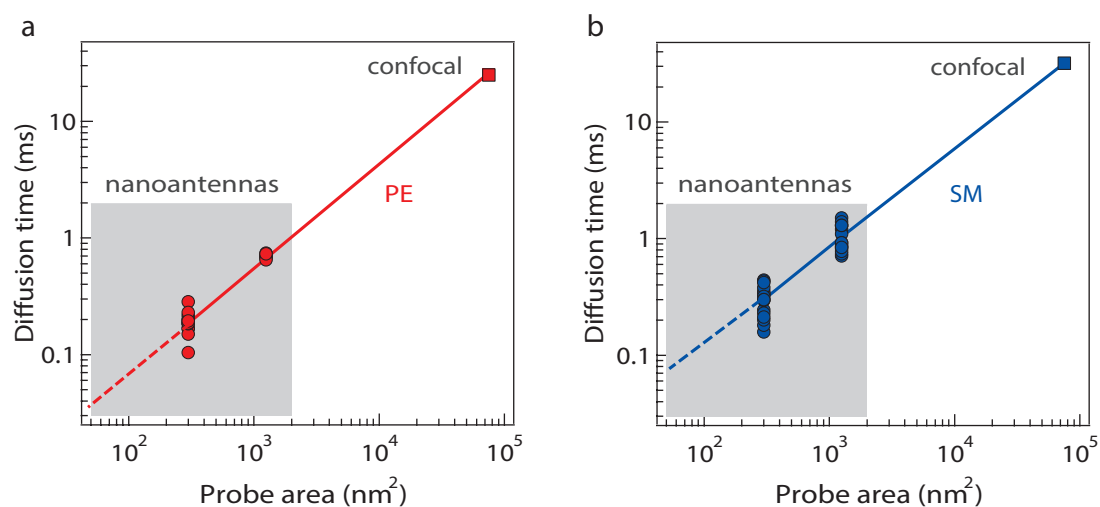


**FIGURE 6.18: FCS diffusion laws with confocal data.** FCS diffusion laws extended to include the confocal data for PE (a) and SM (b). The nanoantenna data is identical to Figure 6.16.

laws which should feature a characteristic transition from confined to normal diffusion [52, 169]. As we do not observe this characteristic transition in our data, we conclude that the typical size of the nanodomain is smaller than the nominal gap size of our nanoantenna, that is 10 nm. Both the typical nanodomain size about 10 nm and the transient time about 100  $\mu$ s stand in good agreement with the predictions from stochastic models [189], and from the earlier experiments with STED-FCS [174, 175, 176] and recent high-speed interferometric scattering (iSCAT) measurements on mimetic lipid bilayers containing cholesterol [164, 190, 191].

## 6.6 Summary

We demonstrate the promising approach of exploiting planar optical nanoantennas with accessible surface nanogaps to investigate the nanoscale architecture of live cell membranes. The key strengths of our approach rely on the 10 nm spatial resolution combined with a microsecond time resolution on a (nearly) perfectly flat substrate compatible with live cell culturing. The single-molecule data on nanoantennas reveal striking differences between PE and SM diffusion dynamics that remain hidden in confocal measurements. Fluorescence burst and correlation spectroscopy analysis for PE are consistent with a free Brownian diffusion model. In contrast, the diffusion dynamics of SM at the nanoscale show heterogeneities in both time and space which are cholesterol dependent. Further, removal of cholesterol leads to a recovery of free Brownian diffusion for SM, consistent with the loss of nanodomains. Our results show the existence of dynamic nanodomains on the plasma membranes of living cells of  $\sim$ 10 nm diameter which is comparable to our

measurement gap size. The corresponding transient trapping times are short of about  $\sim 100 \mu\text{s}$ . We believe that the combination of optical nanoantennas with fluorescence microscopy is a powerful tool to investigate the dynamics and interactions of raft associated proteins and their recruitment into molecular complexes on the plasma membrane of living cells. The proposed technique is fully bio-compatible and thus provides ample opportunities for biophysics and live cell research with single-molecule sensitivity at nanometric and (sub)microsecond spatiotemporal resolution, far beyond the diffraction limit of light.



# Conclusion and Perspective

In this thesis, we explored various nanoantenna designs to achieve optimum optical performance with single-molecule sensitivity at molecular concentrations exceeding  $20 \mu\text{M}$ . The enhanced near field intensity, increased quantum yield of the emitter in the vicinity of the nanoantenna together with high Purcell effects collectively result in giant fluorescence enhancements within very small mode volumes (up to 30k-fold below the diffraction-limited confocal scheme). The near field confinement of the excitation intensity together with the polarization sensitivity of these nanostructures were then demonstrated for (i) detecting single-molecules diffusing in solution and (ii) investigating nanoscale membrane architecture of the plasma membrane in the living cells.

As the fluorescence strongly depends upon the local environment to which an single emitter is exposed, the emission can be tailored by varying the shapes, dimensions or even the composition of the nanostructures. In Chapter 3, we explored double nanoholes antenna design for enhanced single-molecule fluorescence detection. Using fluorescence correlation spectroscopy, we measured a 70 zL near field apex volume, realizing a volume reduction of 7000-fold as compared to the diffraction-limited confocal configuration. The high intensity confinement goes with fluorescence enhancement up to 100-fold, together with microsecond transit time, 30-fold LDOS enhancement and single molecule sensitivity at concentrations exceeding  $20 \mu\text{M}$ . The DNH provides an efficient design to reach nanometric confinement of light, with a much simpler nanofabrication as compared to other designs such as “antenna-in-box” or bowtie structures. The DNH spectral resonance occurs in the range 550-700 nm therefore enables a better spectral overlap with the emission band of most common red fluorescent dyes. We also point out that much room remains for a thorough optimization of the DNH design. In this regard, we further demonstrated higher enhancement factors above 300-fold achieved with DNH bearing sharp apex tips fabricated *via* stencil lithography. Reaching sub-10 nm apex sizes with modern fabrication tools (such as He ion source FIB), mass fabrication of DNH structures with sharp apex tips will significantly upgrade the caliber of DNH structures with single-molecule sensitivity at much higher molecular concentrations.

Single molecule fluorescence sensors based on plasmonic nanostructures are currently limited by the nonradiative energy transfer (between emitters and free electron gas), and by the Joule heating caused by the excitation laser beam. Silicon based all-dielectric nanoantennas overcome these limitations, and thus are potential cost effective alternative for realizing molecular sensors with on-chip and CMOS compatibility. In Chapter 4, we

demonstrated the first proof-of-principle all-dielectric nanoantennas with single-molecule sensitivity and explained the fluorescence enhancement mechanism by a combination of excitation intensity enhancement and radiative rate enhancement with near similar strengths. For an all-silicon dimer nanoantenna with 20 nm nominal gap fabricated on glass substrates, we quantify fluorescence enhancement factors above 200-fold, together with 3600-fold volume reduction as compared to the diffraction-limited confocal schemes. At present, the maximum fluorophore concentration to reach single-molecule sensitivity is limited to around 10  $\mu\text{M}$ , which can be further improved either by reducing the dimer gap separations, or *via* introducing a surrounding box-aperture to keep-out the fluorescence light originating from the background molecules (similar to the “antenna-in-box” geometry). Since all-dielectric nanoantenna has negligible losses, sub-nm gaps can be conceived for single-molecule experiments. Moreover, as the scattering spectrum of the silicon nanoantenna shows higher efficiency in the near-IR, optimized experimental strategy (with proper dye selection and reduced gap sizes) could significantly improve the detection of individual molecules at higher molecular concentrations using dielectric materials only.

Further, meeting the broad expectations of biologically-inspired experiments require nanoantennas featuring narrow gap sizes, full accessibility to the electromagnetic hotspot and high fabrication throughput. Our planar “antenna-in-box” design (Chapter 5, 6) address this concerns with an innovative fabrication approach combining e-beam lithography with planarization, etch back and template stripping. We present large sets of fully flat gold nanoantennas arrays featuring 10 nm nominal gaps with sharp edges and direct surface accessibility of the hotspots. We demonstrate the superior performance of these in-plane nanoantennas by probing single fluorescent molecules, and reach fluorescence enhancement factors up to 15,000-fold, outperforming any previous plasmonic realizations. In excellent agreement with numerical simulations, we relate this performance increase to the optimized position of the plasmonic hotspot which are accessible and exposed directly at the surface. The fabrication approach is scalable with excellent reproducibility, and can be applied to any nanoantenna designs. This provides a highly efficient platform for biochemical assays analysis with single molecule sensitivity at physiological conditions. The “antenna-in-box” shows spectral resonance occurring in the near-infrared regime, thus optimizing the nanoantenna geometry for the excitation wavelength, can further boost the fluorescence enhancement factors and the nanoantenna efficiency.

In Chapter 6, we explored planar nanoantennas to investigate the cholesterol-dependent nanoscale heterogeneities in the plasma membrane of living cells. Combining FCS with resonant planar nanoantenna with different gap sizes we could assess the dynamic nanoscale organization of phosphoethanolamine (PE) and sphingomyelin (SM) in the

living plasma membranes. Our approach takes advantage of the highly confined excitation light provided by dimer nanoantennas together with their outstanding planarity to investigate membrane regions as small as 10 nm in size with sub-ms temporal resolution. Fluorescence correlation spectroscopy and burst analysis show free 2D Brownian diffusion for PE (with both confocal and nanoantenna). However the diffusion dynamics of SM at the nanoscale indicates extremely heterogeneous behavior which were otherwise hidden in the ensemble averaging. Together with cholesterol depletion experiments, we demonstrate the existence of dynamic nanodomains (diameter less than 10 nm) with characteristic trapping times as short as 100  $\mu$ s. These findings are crucial to understand the spatiotemporal and heterogeneous organization of live cell membranes at the nanoscale. This planar nanoantenna design with full access of the hotspot opens up the possibility of exploiting the physical properties of plasmonic antennas for a broad range of applications, such as biosensing in nano/microfluidic channels, light harvesting, photocatalysis *etc.* As an immediate extension, one could possibly think of investigating the raft-associated GPI anchored protein and their co-localization with SM (and cholesterol) in the plasma membranes. This could possibly provide complementary insights into the local organization of the plasma membrane in living cells. The proposed technique is bio-compatible and thus provides ample opportunities in biophysics and live cell experiments. To further increase the flexibility of these planar nanoantenna platforms, designing hybrid nanoantenna for broadband excitation, and time-gated detection for further reduction in spatial resolution remain as some of the immediate experimental strategies.

Altogether, using FCS, TCSPC, FDTD modeling and numerical simulations, this thesis provides a thorough investigation on different optical nanoantenna designs (double nanohole, nanogap dimer antennas and planar “antenna-in-box”) along with the discussion on their respective merits. Probing emitters with different intrinsic quantum yields (Alexa Fluor 647, CV and Atto647N) we discussed the origin of fluorescence in the nanoantenna mediated single-molecule experiments. The high optical performance achieved with the robust designs open up promising perspectives to study complex biochemical dynamics at physiological expression levels. In addition, the nanoantenna approach is quite straightforward to implement on any confocal setup, as it does not require supplementary illumination beam (or optics). For now, the race for the higher enhancement factors should be only secondary to the potential applications of these nanoantennas in biophysics and live cell research.



## Publications based on the Thesis

**Regmi, R.**, Winkler, P.M., Flauraud, V., Borgman, K.J.E., Manzo, C., Brugger, J., Rigneault, H., Wenger, J. and García-Parajo, M.F., 2017. Planar optical nanoantennas resolve cholesterol-dependent nanoscale heterogeneities in the plasma membrane of living cells. *Nano Letters*, 17 (10), pp.6295-6302.

Winkler, P.M., **Regmi, R.**, Flauraud, V., Brugger, J., Rigneault, H., Wenger, J. and García-Parajo, M.F., 2017. Transient nanoscopic phase separation in biological lipid membranes resolved by planar plasmonic antennas. *ACS Nano*, 11(7), pp.7241-7250.

Flauraud, V., **Regmi, R.**, Winkler, P.M., Alexander, D.T., Rigneault, H., van Hulst, N.F., García-Parajo, M.F., Wenger, J. and Brugger, J., 2017. In-plane plasmonic antenna arrays with surface nanogaps for giant fluorescence enhancement. *Nano Letters*, 17(3), pp.1703-1710.

**Regmi, R.**, Berthelot, J., Winkler, P.M., Mivelle, M., Proust, J., Bedu, F., Ozerov, I., Begou, T., Lumeau, J., Rigneault, H., García-Parajo, M.F., Bidault, S., Wenger, J. and Bonod, N., 2016. All-dielectric silicon nanogap antennas to enhance the fluorescence of single molecules. *Nano Letters*, 16(8), pp.5143-5151.

Wenger, J., **Regmi, R.**, and Rigneault, H., 2016. Plasmonic-enhanced fluorescence detection of single molecules at high concentrations, in Roadmap article edited by E. Di Fabrizio, *Journal of Optics*, 18(6), p.063003.

**Regmi, R.**, Al Balushi, A.A., Rigneault, H., Gordon, R. and Wenger, J., 2015. Nanoscale volume confinement and fluorescence enhancement with double nanohole aperture. *Scientific Reports*, 5.

Punj, D., **Regmi, R.**, Devilez, A., Plauchu, R., Moparthi, S.B., Stout, B., Bonod, N., Rigneault, H. and Wenger, J., 2015. Self-assembled nanoparticle dimer antennas for plasmonic-enhanced single-molecule fluorescence detection at micromolar concentrations. *ACS Photonics*, 2(8), pp.1099-1107.



# Bibliography

- [1] Betzig, E., Hell, S.W. and Moerner, W.E., 2015. The Nobel Prize in Chemistry 2014. *Nobelprize.org/nobel\_prizes/chemistry/laureates/2014/* (Accessed September 13, 2017)
- [2] Moerner, W.E., 2015. Nobel Lecture: Single-molecule spectroscopy, imaging, and photocontrol: Foundations for super-resolution microscopy. *Reviews of Modern Physics*, 87, pp.1183-1212.
- [3] Moerner, W.E. and Kador, L., 1989. Optical detection and spectroscopy of single molecules in a solid. *Physical Review Letters*, 62(21), p.2535.
- [4] Orrit, M. and Bernard, J., 1990. Single pentacene molecules detected by fluorescence excitation in a p-terphenyl crystal. *Physical Review Letters*, 65(21), p.2716.
- [5] Moerner, W.E. and Orrit, M., 1999. Illuminating single molecules in condensed matter. *Science*, 283(5408), pp.1670-1676.
- [6] Abbe, E., 1873. Beiträge zur Theorie des Mikroskops und der mikroskopischen Wahrnehmung. *Archiv für mikroskopische Anatomie*, 9(1), pp.413-418.
- [7] Di Fabrizio, E., Schlücker, S., Wenger, J., Regmi, R., Rigneault, H., Calafiore, G., West, M., Cabrini, S., Fleischer, M., Van Hulst, N.F. and García-Parajo, M.F., 2016. Roadmap on biosensing and photonics with advanced nano-optical methods. *Journal of Optics*, 18(6), p.063003.
- [8] Punj, D., Ghenuche, P., Moparthi, S.B., de Torres, J., Grigoriev, V., Rigneault, H. and Wenger, J., 2014. Plasmonic antennas and zeromode waveguides to enhance single molecule fluorescence detection and fluorescence correlation spectroscopy toward physiological concentrations. *Wiley Interdisciplinary Reviews: Nanomedicine and Nanobiotechnology*, 6(3), pp.268-282.
- [9] Wenger, J. and Rigneault, H., 2010. Photonic methods to enhance fluorescence correlation spectroscopy and single molecule fluorescence detection. *International Journal of Molecular Sciences*, 11(1), pp.206-221.

- 
- [10] García-Parajo, M.F., 2008. Optical antennas focus in on biology. *Nature Photonics*, 2(4), pp.201-203.
- [11] Novotny, L. and Van Hulst, N., 2011. Antennas for light. *Nature Photonics*, 5(2), pp.83-90.
- [12] Wientjes, E., Renger, J., Curto, A.G., Cogdell, R. and Van Hulst, N.F., 2014. Strong antenna-enhanced fluorescence of a single light-harvesting complex shows photon antibunching. *Nature Communications*, 5.
- [13] Pang, Y. and Gordon, R., 2011. Optical trapping of a single protein. *Nano Letters*, 12(1), pp.402-406.
- [14] Anger, P., Bharadwaj, P. and Novotny, L., 2006. Enhancement and quenching of single-molecule fluorescence. *Physical Review Letters*, 96(11), p.113002.
- [15] Punj, D., de Torres, J., Rigneault, H. and Wenger, J., 2013. Gold nanoparticles for enhanced single molecule fluorescence analysis at micromolar concentration. *Optics Express*, 21(22), pp.27338-27343.
- [16] Yuan, H., Khatua, S., Zijlstra, P., Yorulmaz, M. and Orrit, M., 2013. Thousand-fold Enhancement of SingleMolecule Fluorescence Near a Single Gold Nanorod. *Angewandte Chemie International Edition*, 52(4), pp.1217-1221.
- [17] Khatua, S., Paulo, P.M., Yuan, H., Gupta, A., Zijlstra, P. and Orrit, M., 2014. Resonant plasmonic enhancement of single-molecule fluorescence by individual gold nanorods. *ACS Nano*, 8(5), pp.4440-4449.
- [18] Kinkhabwala, A., Yu, Z., Fan, S., Avlasevich, Y., Müllen, K. and Moerner, W.E., 2009. Large single-molecule fluorescence enhancements produced by a bowtie nanoantenna. *Nature Photonics*, 3(11), pp.654-657.
- [19] Acuna, G.P., Möller, F.M., Holzmeister, P., Beater, S., Lalkens, B. and Tinnefeld, P., 2012. Fluorescence enhancement at docking sites of DNA-directed self-assembled nanoantennas. *Science*, 338(6106), pp.506-510.
- [20] Ureña, E.B., Kreuzer, M.P., Itzhakov, S., Rigneault, H., Quidant, R., Oron, D. and Wenger, J., 2012. Excitation enhancement of a quantum dot coupled to a plasmonic antenna. *Advanced Materials*, 24(44).
- [21] Punj, D., Regmi, R., Devilez, A., Plauchu, R., Moparthi, S.B., Stout, B., Bonod, N., Rigneault, H. and Wenger, J., 2015. Self-assembled nanoparticle dimer antennas for plasmonic-enhanced single-molecule fluorescence detection at micromolar concentrations. *ACS Photonics*, 2(8), pp.1099-1107.

- [22] Holzmeister, P., Acuna, G.P., Grohmann, D. and Tinnefeld, P., 2014. Breaking the concentration limit of optical single-molecule detection. *Chemical Society Reviews*, 43(4), pp.1014-1028.
- [23] Hell, S.W., 2007. Far-field optical nanoscopy. *Science*, 316(5828), pp.1153-1158.
- [24] Eid, J., Fehr, A., Gray, J., Luong, K., Lyle, J., Otto, G., Peluso, P., Rank, D., Baybayan, P., Bettman, B. and Bibillo, A., 2009. Real-time DNA sequencing from single polymerase molecules. *Science*, 323(5910), pp.133-138.
- [25] Lee, S.A., Ponjavic, A., Siv, C., Lee, S.F. and Biteen, J.S., 2016. Nanoscopic cellular imaging: confinement broadens understanding. *ACS Nano*, 10(9), pp.8143-8153.
- [26] Punj, D., 2014. *Optical antennas for single molecule fluorescence detection at physiological concentration* (Doctoral dissertation, Aix Marseille université).
- [27] Betzig, E. and Trautman, J.K., 1991. Breaking the diffraction barrier: optical microscopy on a nanometric scale. *Science*, 251(5000), p.1468.
- [28] Trautman, J.K., Macklin, J.J., Brus, L.E. and Betzig, E., 1994. Near-field spectroscopy of single molecules at room temperature. *Nature*, 369(6475), pp.40-42.
- [29] Manzo, C., van Zanten, T.S. and García-Parajo, M.F., 2011. Nanoscale fluorescence correlation spectroscopy on intact living cell membranes with NSOM probes. *Biophysical Journal*, 100(2), pp.L8-L10.
- [30] Ruitter, A.G.T., Veerman, J.A., García-Parajo, M.F. and Van Hulst, N.F., 1997. Single molecule rotational and translational diffusion observed by near-field scanning optical microscopy. *The Journal of Physical Chemistry A*, 101(40), pp.7318-7323.
- [31] Mivelle, M., van Zanten, T.S., Neumann, L., van Hulst, N.F. and García-Parajo, M.F., 2012. Ultrabright bowtie nanoaperture antenna probes studied by single molecule fluorescence. *Nano Letters*, 12(11), pp.5972-5978.
- [32] Fish, K.N., 2009. Total internal reflection fluorescence (TIRF) microscopy. *Current Protocols in Cytometry*, pp.12-18.
- [33] Hassler, K., Leutenegger, M., Rigler, P., Rao, R., Rigler, R., Gösch, M. and Lasser, T., 2005. Total internal reflection fluorescence correlation spectroscopy (TIR-FCS) with low background and high count-rate per molecule. *Optics Express*, 13(19), pp.7415-7423.
- [34] Hell, S.W. and Wichmann, J., 1994. Breaking the diffraction resolution limit by stimulated emission: stimulated-emission-depletion fluorescence microscopy. *Optics Letters*, 19(11), pp.780-782.

- [35] Klar, T.A., Jakobs, S., Dyba, M., Egner, A. and Hell, S.W., 2000. Fluorescence microscopy with diffraction resolution barrier broken by stimulated emission. *Proceedings of the National Academy of Sciences*, 97(15), pp.8206-8210.
- [36] Ahrens, M.B., Orger, M.B., Robson, D.N., Li, J.M. and Keller, P.J., 2013. Whole-brain functional imaging at cellular resolution using light-sheet microscopy. *Nature Methods*, 10(5), pp.413-420.
- [37] Singh, A.P., Krieger, J.W., Buchholz, J., Charbon, E., Langowski, J. and Wohland, T., 2013. The performance of 2D array detectors for light sheet based fluorescence correlation spectroscopy. *Optics express*, 21(7), pp.8652-8668.
- [38] Krieger, J.W., Singh, A.P., Garbe, C.S., Wohland, T. and Langowski, J., 2014. Dual-color fluorescence cross-correlation spectroscopy on a single plane illumination microscope (SPIM-FCCS). *Optics Express*, 22(3), pp.2358-2375.
- [39] Giannini, V., Sánchez-Gil, J.A., Muskens, O.L. and Rivas, J.G., 2009. Electrodynamic calculations of spontaneous emission coupled to metal nanostructures of arbitrary shape: nanoantenna-enhanced fluorescence. *JOSA B*, 26(8), pp.1569-1577.
- [40] Berman, P.R., 1994. Cavity quantum electrodynamics.
- [41] Giannini, V., FernándezDomínguez, A.I., Sonnefraud, Y., Roschuk, T., FernándezGarcía, R. and Maier, S.A., 2010. Controlling light localization and light-matter interactions with nanoplasmonics. *Small*, 6(22), pp.2498-2507.
- [42] Zander, C., Enderlein, J. and Keller, R. A., 2002. *Single-Molecule Detection in Solution - Methods and Applications*. VCH-Wiley, Berlin/New York.
- [43] Taylor, A. and Zijlstra, P., 2017. Single-molecule plasmon sensing: current status and future prospects. *ACS Sensors*.
- [44] Park, J.E., Kim, J. and Nam, J.M., 2017. Emerging plasmonic nanostructures for controlling and enhancing photoluminescence. *Chemical Science*, 8(7), pp.4696-4704.
- [45] Gérard, D., Wenger, J., Bonod, N., Popov, E., Rigneault, H., Mahdavi, F., Blair, S., Dintinger, J. and Ebbesen, T.W., 2008. Nanoaperture-enhanced fluorescence: Towards higher detection rates with plasmonic metals. *Physical Review B*, 77(4), p.045413.
- [46] Levene, M.J., Korlach, J., Turner, S.W., Foquet, M., Craighead, H.G. and Webb, W.W., 2003. Zero-mode waveguides for single-molecule analysis at high concentrations. *Science*, 299(5607), pp.682-686.

- [47] Aouani, H., Itzhakov, S., Gachet, D., Devaux, E., Ebbesen, T.W., Rigneault, H., Oron, D. and Wenger, J., 2010. Colloidal quantum dots as probes of excitation field enhancement in photonic antennas. *ACS Nano*, 4(8), pp.4571-4578.
- [48] Aouani, H., Mahboub, O., Devaux, E., Rigneault, H., Ebbesen, T.W. and Wenger, J., 2011. Large molecular fluorescence enhancement by a nanoaperture with plasmonic corrugations. *Optics Express*, 19(14), pp.13056-13062.
- [49] Rigneault, H., Capoulade, J., Dintinger, J., Wenger, J., Bonod, N., Popov, E., Ebbesen, T.W. and Lenne, P.F., 2005. Enhancement of single-molecule fluorescence detection in subwavelength apertures. *Physical Review Letters*, 95(11), p.117401.
- [50] Popov, E., Nevière, M., Wenger, J., Lenne, P.F., Rigneault, H., Chaumet, P., Bonod, N., Dintinger, J. and Ebbesen, T., 2006. Field enhancement in single sub-wavelength apertures. *JOSA A*, 23(9), pp.2342-2348.
- [51] Moran-Mirabal, J.M., Torres, A.J., Samiee, K.T., Baird, B.A. and Craighead, H.G., 2007. Cell investigation of nanostructures: zero-mode waveguides for plasma membrane studies with single molecule resolution. *Nanotechnology*, 18(19), p.195101.
- [52] Wenger, J., Conchonaud, F., Dintinger, J., Wawrezynieck, L., Ebbesen, T.W., Rigneault, H., Marguet, D. and Lenne, P.F., 2007. Diffusion analysis within single nanometric apertures reveals the ultrafine cell membrane organization. *Biophysical Journal*, 92(3), pp.913-919.
- [53] Wenger J, Rigneault H, Dintinger J, Marguet D, Lenne PF. Single-fluorophore diffusion in a lipid membrane over a subwavelength aperture. *Journal of Biological Physics*. 2006 Jan 8;32(1):SN1-4.
- [54] Wenger, J., Cluzel, B., Dintinger, J., Bonod, N., Fehrembach, A.L., Popov, E., Lenne, P.F., Ebbesen, T.W. and Rigneault, H., 2007. Radiative and nonradiative photokinetics alteration inside a single metallic nanometric aperture. *The Journal of Physical Chemistry C*, 111(30), pp.11469-11474.
- [55] Pradhan, B., Khatua, S., Gupta, A., Aartsma, T., Canters, G. and Orrit, M., 2016. Gold-Nanorod-Enhanced Fluorescence Correlation Spectroscopy of Fluorophores with High Quantum Yield in Lipid Bilayers. *The Journal of Physical Chemistry C*, 120(45), pp.25996-26003.
- [56] Zijlstra, P., Paulo, P.M. and Orrit, M., 2012. Optical detection of single non-absorbing molecules using the surface plasmon resonance of a gold nanorod. *Nature Nanotechnology*, 7(6), pp.379-382.

- [57] Akselrod, G.M., Argyropoulos, C., Hoang, T.B., Ciraci, C., Fang, C., Huang, J., Smith, D.R. and Mikkelsen, M.H., 2014. Probing the mechanisms of large Purcell enhancement in plasmonic nanoantennas. *Nature Photonics*, 8(11), pp.835-840.
- [58] Rose, A., Hoang, T.B., McGuire, F., Mock, J.J., Ciraci, C., Smith, D.R. and Mikkelsen, M.H., 2014. Control of radiative processes using tunable plasmonic nanopatch antennas. *Nano Letters*, 14(8), pp.4797-4802.
- [59] Yi, M., Zhang, D., Wang, P., Jiao, X., Blair, S., Wen, X., Fu, Q., Lu, Y. and Ming, H., 2011. Plasmonic interaction between silver nano-cubes and a silver ground plane studied by surface-enhanced Raman scattering. *Plasmonics*, 6(3), pp.515-519.
- [60] Puchkova, A., Vietz, C., Pibiri, E., Wunsch, B., Sanz Paz, M., Acuna, G.P. and Tinnefeld, P., 2015. DNA origami nanoantennas with over 5000-fold fluorescence enhancement and single-molecule detection at 25  $\mu\text{M}$ . *Nano Letters*, 15(12), pp.8354-8359.
- [61] Flauraud, V., Regmi, R., Winkler, P.M., Alexander, D.T., Rigneault, H., Van Hulst, N.F., García-Parajo, M.F., Wenger, J. and Brugger, J., 2017. In-plane plasmonic antenna arrays with surface nanogaps for giant fluorescence enhancement. *Nano Letters*, 17(3), pp.1703-1710.
- [62] Winkler, P.M., Regmi, R., Flauraud, V., Brugger, J., Rigneault, H., Wenger, J. and García-Parajo, M.F., 2017. Transient nanoscopic phase separation in biological lipid membranes resolved by planar plasmonic antennas. *ACS Nano*, 11(7), pp.7241-7250.
- [63] Regmi, R., Winkler, P.M., Flauraud, V., Borgman, K.J.E., Manzo, C., Brugger, J., Rigneault, H., Wenger, J. and García-Parajo, M.F., 2017. Planar optical nanoantennas resolve cholesterol-dependent nanoscale heterogeneities in the plasma membrane of living cells. *Nano Letters*, 17(10), pp.6295-6302.
- [64] Regmi, R., Al Balushi, A.A., Rigneault, H., Gordon, R. and Wenger, J., 2015. Nanoscale volume confinement and fluorescence enhancement with double nanohole aperture. *Scientific Reports*, 5.
- [65] Wenger, J., Lenne, P.F., Popov, E., Rigneault, H., Dintinger, J. and Ebbesen, T.W., 2005. Single molecule fluorescence in rectangular nano-apertures. *Optics Express*, 13(18), pp.7035-7044.
- [66] Acuna, G., Grohmann, D. and Tinnefeld, P., 2014. Enhancing singlemolecule fluorescence with nanophotonics. *FEBS Letters*, 588(19), pp.3547-3552.

- [67] Regmi, R., Berthelot, J., Winkler, P.M., Mivelle, M., Proust, J., Bedu, F., Ozerov, I., Begou, T., Lumeau, J., Rigneault, H., García-Parajo, M.F., Wenger, J., and Bonod, N., 2016. All-dielectric silicon nanogap antennas to enhance the fluorescence of single molecules. *Nano Letters*, 16(8), pp.5143-5151.
- [68] Maiti, S., Haupts, U. and Webb, W.W., 1997. Fluorescence correlation spectroscopy: diagnostics for sparse molecules. *Proceedings of the National Academy of Sciences*, 94(22), pp.11753-11757.
- [69] Magde, D., Elson, E. and Webb, W.W., 1972. Thermodynamic fluctuations in a reacting system measurement by fluorescence correlation spectroscopy. *Physical Review Letters*, 29(11), p.705.
- [70] Wenger, J., Gérard, D., Lenne, P.F., Rigneault, H., Dintinger, J., Ebbesen, T.W., Boned, A., Conchonaud, F. and Marguet, D., 2006. Dual-color fluorescence cross-correlation spectroscopy in a single nanoaperture: towards rapid multicomponent screening at high concentrations. *Optics Express*, 14(25), pp.12206-12216.
- [71] Haustein, E. and Schwille, P., 2004. Fluorescence correlation spectroscopy: an introduction to its concepts and applications. *Biophysics Textbook Online*.
- [72] Rigler, R. and Elson, E.S. eds., 2001. *Fluorescence correlation spectroscopy: theory and applications* (Vol. 65). Springer Science & Business Media.
- [73] Wahl, M., 2002. Time-Correlated Photon Counting Tech Note TCSPC1. 2. *Pico-Quant GmbH*.
- [74] Grecco, H.E. and Verveer, P.J., 2011. FRET in Cell Biology: Still Shining in the Age of Super-Resolution?. *ChemPhysChem*, 12(3), pp.484-490.
- [75] Elson, D., Requejo-Isidro, J., Munro, I., Reavell, F., Siegel, J., Suhling, K., Tadrous, P., Benninger, R., Lanigan, P., McGinty, J. and Talbot, C., 2004. Time-domain fluorescence lifetime imaging applied to biological tissue. *Photochemical & Photobiological Sciences*, 3(8), pp.795-801.
- [76] Koppel, D.E., 1974. Statistical accuracy in fluorescence correlation spectroscopy. *Physical Review A*, 10(6), p.1938.
- [77] Wenger, J., Gerard, D., Aouani, H., Rigneault, H., Lowder, B., Blair, S., Devaux, E. and Ebbesen, T.W., 2008. Nanoaperture-enhanced signal-to-noise ratio in fluorescence correlation spectroscopy. *Analytical Chemistry*, 81(2), pp.834-839.
- [78] Pang, Y. and Gordon, R., 2011. Optical trapping of 12 nm dielectric spheres using double-nanoholes in a gold film. *Nano Letters*, 11(9), pp.3763-3767.

- [79] Kotnala, A., DePaoli, D. and Gordon, R., 2013. Sensing nanoparticles using a double nanohole optical trap. *Lab on a Chip*, 13(20), pp.4142-4146.
- [80] Gelfand, R.M., Wheaton, S. and Gordon, R., 2014. Cleaved fiber optic double nanohole optical tweezers for trapping nanoparticles. *Optics Letters*, 39(22), pp.6415-6417.
- [81] Al Balushi, A.A., Zehtabi-Oskuie, A. and Gordon, R., 2013. Observing single protein binding by optical transmission through a double nanohole aperture in a metal film. *Biomedical Optics Express*, 4(9), pp.1504-1511.
- [82] Al Balushi, A.A. and Gordon, R., 2014. A label-free untethered approach to single-molecule protein binding kinetics. *Nano Letters*, 14(10), pp.5787-5791.
- [83] Al Balushi, A.A. and Gordon, R., 2014. Label-free free-solution single-molecule proteinsmall molecule interaction observed by double-nanohole plasmonic trapping. *ACS Photonics*, 1(5), pp.389-393.
- [84] Lesuffleur, A., Kumar, L.K.S., Brolo, A.G., Kavanagh, K.L. and Gordon, R., 2007. Apex-enhanced Raman spectroscopy using double-hole arrays in a gold film. *The Journal of Physical Chemistry C*, 111(6), pp.2347-2350.
- [85] Lesuffleur, A., Kumar, L.K.S. and Gordon, R., 2007. Apex-enhanced second-harmonic generation by using double-hole arrays in a gold film. *Physical Review B*, 75(4), p.045423.
- [86] Fromm, D.P., Sundaramurthy, A., Schuck, P.J., Kino, G. and Moerner, W.E., 2004. Gap-dependent optical coupling of single “bowtie” nanoantennas resonant in the visible. *Nano Letters*, 4(5), pp.957-961.
- [87] Lu, G., Li, W., Zhang, T., Yue, S., Liu, J., Hou, L., Li, Z. and Gong, Q., 2012. Plasmonic-enhanced molecular fluorescence within isolated bowtie nano-apertures. *Acs Nano*, 6(2), pp.1438-1448.
- [88] Berthelot, J., Acímović, S.S., Juan, M.L., Kreuzer, M.P., Renger, J. and Quidant, R., 2014. Three-dimensional manipulation with scanning near-field optical nanotweezers. *Nature Nanotechnology*, 9(4), pp.295-299.
- [89] Punj, D., Mivelle, M., Moparthi, S.B., Van Zanten, T.S., Rigneault, H., Van Hulst, N.F., García-Parajo, M.F. and Wenger, J., 2013. A plasmonic “antenna-in-box” platform for enhanced single-molecule analysis at micromolar concentrations. *Nature Nanotechnology*, 8(7), pp.512-516.
- [90] Johnson, P.B. and Christy, R.W., 1972. Optical constants of the noble metals. *Physical Review B*, 6(12), p.4370.

- [91] Wenger, J., Gérard, D., Dintinger, J., Mahboub, O., Bonod, N., Popov, E., Ebbesen, T.W. and Rigneault, H., 2008. Emission and excitation contributions to enhanced single molecule fluorescence by gold nanometric apertures. *Optics Express*, 16(5), pp.3008-3020.
- [92] Aouani, H., Mahboub, O., Bonod, N., Devaux, E., Popov, E., Rigneault, H., Ebbesen, T.W. and Wenger, J., 2011. Bright unidirectional fluorescence emission of molecules in a nanoaperture with plasmonic corrugations. *Nano Letters*, 11(2), pp.637-644.
- [93] Bharadwaj, P. and Novotny, L., 2007. Spectral dependence of single molecule fluorescence enhancement. *Optics Express*, 15(21), pp.14266-14274.
- [94] Ghenuche, P., de Torres, J., Moparthi, S.B., Grigoriev, V. and Wenger, J., 2014. Nanophotonic enhancement of the Förster resonance energy-transfer rate with single nanoapertures. *Nano Letters*, 14(8), pp.4707-4714.
- [95] Novotny, L., Hecht, B., 2006. *Principles of Nano-Optics*. Cambridge University press.
- [96] De Torres, J., 2016. *Nanophotonic control of Förster Resonance Energy Transfer* (Doctoral dissertation, Aix Marseille université).
- [97] Chowdhury, M.H., Pond, J., Gray, S.K. and Lakowicz, J.R., 2008. Systematic computational study of the effect of silver nanoparticle dimers on the coupled emission from nearby fluorophores. *The Journal of Physical Chemistry C*, 112(30), pp.11236-11249.
- [98] Lakowicz, J.R. and Fu, Y., 2009. Modification of single molecule fluorescence near metallic nanostructures. *Laser & Photonics Reviews*, 3(12), pp.221-232.
- [99] Biagioni, P., Huang, J.S. and Hecht, B., 2012. Nanoantennas for visible and infrared radiation. *Reports on Progress in Physics*, 75(2), p.024402.
- [100] Bidault, S., Devilez, A., Maillard, V., Lermusiaux, L., Guigner, J.M., Bonod, N. and Wenger, J., 2016. Picosecond lifetimes with high quantum yields from single-photon-emitting colloidal nanostructures at room temperature. *ACS Nano*, 10(4), pp.4806-4815.
- [101] Curto, A.G., Volpe, G., Taminiau, T.H., Kreuzer, M.P., Quidant, R. and van Hulst, N.F., 2010. Unidirectional emission of a quantum dot coupled to a nanoantenna. *Science*, 329(5994), pp.930-933.
- [102] Baffou, G. and Quidant, R., 2013. Thermo-plasmonics: using metallic nanostructures as nanosources of heat. *Laser & Photonics Reviews*, 7(2), pp.171-187.

- [103] Abadeer, N.S. and Murphy, C.J., 2016. Recent progress in cancer thermal therapy using gold nanoparticles. *The Journal of Physical Chemistry C*, 120(9), pp.4691-4716.
- [104] Zhu, M., Baffou, G., Meyerbröcker, N. and Polleux, J., 2012. Micropatterning thermoplasmonic gold nanoarrays to manipulate cell adhesion. *ACS nano*, 6(8), pp.7227-7233.
- [105] García-Etxarri, A., Gómez-Medina, R., Froufe-Prez, L.S., López, C., Chantada, L., Scheffold, F., Aizpurua, J., Nieto-Vesperinas, M. and Senz, J.J., 2011. Strong magnetic response of submicron silicon particles in the infrared. *Optics express*, 19(6), pp.4815-4826.
- [106] Evlyukhin, A.B., Novikov, S.M., Zywiets, U., Eriksen, R.L., Reinhardt, C., Bozhevolnyi, S.I. and Chichkov, B.N., 2012. Demonstration of magnetic dipole resonances of dielectric nanospheres in the visible region. *Nano Letters*, 12(7), pp.3749-3755.
- [107] Kuznetsov, A.I., Miroshnichenko, A.E., Fu, Y.H., Zhang, J. and Luk'yanchuk, B., 2012. Magnetic light. *Scientific Reports*, 2, p.srep00492.
- [108] <http://refractiveindex.info/>(accessed July 12, 2016)
- [109] Mie, G., 1908. Beiträge zur Optik trüber Medien, speziell kolloidaler Metallösungen. *Annalen der Physik*, 330(3), pp.377-445.
- [110] Sigalas, M.M., Fattal, D.A., Williams, R.S., Wang, S.Y. and Beausoleil, R.G., 2007. Electric field enhancement between two Si microdisks. *Optics Express*, 15(22), pp.14711-14716.
- [111] Rolly, B., Bebey, B., Bidault, S., Stout, B. and Bonod, N., 2012. Promoting magnetic dipolar transition in trivalent lanthanide ions with lossless Mie resonances. *Physical Review B*, 85(24), p.245432.
- [112] Albella, P., Poyli, M.A., Schmidt, M.K., Maier, S.A., Moreno, F., Saenz, J.J. and Aizpurua, J., 2013. Low-loss electric and magnetic field-enhanced spectroscopy with subwavelength silicon dimers. *The Journal of Physical Chemistry C*, 117(26), pp.13573-13584.
- [113] Boudarham, G., Abdeddaim, R. and Bonod, N., 2014. Enhancing the magnetic field intensity with a dielectric gap antenna. *Applied Physics Letters*, 104(2), p.021117.

- [114] Bakker, R.M., Permyakov, D., Yu, Y.F., Markovich, D., Paniagua-Domnguez, R., Gonzaga, L., Samusev, A., Kivshar, Y., Luk'yanchuk, B. and Kuznetsov, A.I., 2015. Magnetic and electric hotspots with silicon nanodimers. *Nano Letters*, 15(3), pp.2137-2142.
- [115] Vahala, K.J., 2003. Optical microcavities. *Nature* 424(6950), p.839.
- [116] Lodahl, P., Mahmoodian, S. and Stobbe, S., 2015. Interfacing single photons and single quantum dots with photonic nanostructures. *Reviews of Modern Physics*, 87(2), p.347.
- [117] Armani, D.K., Kippenberg, T.J., Spillane, S.M. and Vahala, K.J., 2003. Ultra-high-Q toroid microcavity on a chip. *Nature*, 421(6926), p.925.
- [118] Armani, A.M., Kulkarni, R.P., Fraser, S.E., Flagan, R.C. and Vahala, K.J., 2007. Label-free, single-molecule detection with optical microcavities. *Science*, 317(5839), pp.783-787.
- [119] Lee, K.G., Chen, X.W., Eghlidi, H., Kukura, P., Lettow, R., Renn, A., Sandoghdar, V. and Göttinger, S., 2011. A planar dielectric antenna for directional single-photon emission and near-unity collection efficiency. *Nature Photonics*, 5(3), pp.166-169.
- [120] Chu, X.L., Brenner, T.J., Chen, X.W., Ghosh, Y., Hollingsworth, J.A., Sandoghdar, V. and Göttinger, S., 2014. Experimental realization of an optical antenna designed for collecting 99% of photons from a quantum emitter. *Optica*, 1(4), pp.203-208.
- [121] Zambrana-Puyalto, X. and Bonod, N., 2015. Purcell factor of spherical Mie resonators. *Physical Review B*, 91(19), p.195422.
- [122] Zywietz, U., Evlyukhin, A.B., Reinhardt, C. and Chichkov, B.N., 2014. Laser printing of silicon nanoparticles with resonant optical electric and magnetic responses. *Nature Communications*, 5, p.3402.
- [123] Andres-Arroyo, A., Gupta, B., Wang, F., Gooding, J.J. and Reece, P.J., 2016. Optical manipulation and spectroscopy of silicon nanoparticles exhibiting dielectric resonances. *Nano Letters*, 16(3), pp.1903-1910.
- [124] van de Groep, J., Coenen, T., Mann, S.A. and Polman, A., 2016. Direct imaging of hybridized eigenmodes in coupled silicon nanoparticles. *Optica*, 3(1), pp.93-99.
- [125] Zambrana-Puyalto, X. and Bonod, N., 2016. Tailoring the chirality of light emission with spherical Si-based antennas. *Nanoscale*, 8(19), pp.10441-10452.

- [126] Dodson, C.M. and Zia, R., 2012. Magnetic dipole and electric quadrupole transitions in the trivalent lanthanide series: Calculated emission rates and oscillator strengths. *Physical Review B*, 86(12), p.125102.
- [127] Schmidt, M.K., Esteban, R., Senz, J., Surez-Lacalle, I., Mackowski, S. and Aizpuru, J., 2012. Dielectric antennas-a suitable platform for controlling magnetic dipolar emission. *Optics Express*, 20(13), pp.13636-13650.
- [128] Devilez, A., Stout, B. and Bonod, N., 2010. Compact metallo-dielectric optical antenna for ultra directional and enhanced radiative emission. *ACS Nano*, 4(6), pp.3390-3396.
- [129] Caldarola, M., Albella, P., Cortés, E., Rahmani, M., Roschuk, T., Grinblat, G., Oulton, R.F., Bragas, A.V. and Maier, S.A., 2015. Non-plasmonic nanoantennas for surface enhanced spectroscopies with ultra-low heat conversion. *Nature Communications*, 6.
- [130] Dmitriev, P.A., Baranov, D.G., Milichko, V.A., Makarov, S.V., Mukhin, I.S., Samusev, A.K., Krasnok, A.E., Belov, P.A. and Kivshar, Y.S., 2016. Resonant Raman scattering from silicon nanoparticles enhanced by magnetic response. *Nanoscale*, 8(18), pp.9721-9726.
- [131] Devilez, A., Bonod, N., Wenger, J., Gérard, D., Stout, B., Rigneault, H. and Popov, E., 2009. Three-dimensional subwavelength confinement of light with dielectric microspheres. *Optics Express*, 17(4), pp.2089-2094.
- [132] Gérard, D., Devilez, A., Aouani, H., Stout, B., Bonod, N., Wenger, J., Popov, E. and Rigneault, H., 2009. Efficient excitation and collection of single-molecule fluorescence close to a dielectric microsphere. *JOSA B*, 26(7), pp.1473-1478.
- [133] Ferrand, P., Wenger, J., Devilez, A., Pianta, M., Stout, B., Bonod, N., Popov, E. and Rigneault, H., 2008. Direct imaging of photonic nanojets. *Optics Express*, 16(10), pp.6930-6940.
- [134] Ghenuche, P., Rigneault, H. and Wenger, J., 2012. Photonic nanojet focusing for hollow-core photonic crystal fiber probes. *Applied Optics*, 51(36), pp.8637-8640.
- [135] Yang, H. and Gijs, M.A., 2013. Microtextured substrates and microparticles used as in situ lenses for on-chip immunofluorescence amplification. *Analytical Chemistry*, 85(4), pp.2064-2071.
- [136] Yang, H., Cornaglia, M. and Gijs, M.A., 2015. Photonic nanojet array for fast detection of single nanoparticles in a flow. *Nano Letters*, 15(3), pp.1730-1735.

- [137] Nobis, T., Kaidashev, E.M., Rahm, A., Lorenz, M. and Grundmann, M., 2004. Whispering gallery modes in nanosized dielectric resonators with hexagonal cross section. *Physical Review Letters*, 93(10), p.103903.
- [138] Teraoka, I. and Arnold, S., 2006. Enhancing the sensitivity of a whispering-gallery mode microsphere sensor by a high-refractive-index surface layer. *JOSA B*, 23(7), pp.1434-1441.
- [139] Scherer, M., Pistner, J. and Lehnert, W., 2010, June. UV-and VIS filter coatings by plasma assisted reactive magnetron sputtering (PARMS). In Optical Interference Coatings (p. MA7). *Optical Society of America*.
- [140] Pierce, D.T. and Spicer, W.E., 1972. Electronic structure of amorphous Si from photoemission and optical studies. *Physical Review B*, 5(8), p.3017.
- [141] Cao, D., Cazé, A., Calabrese, M., Pierrat, R., Bardou, N., Collin, S., Carminati, R., Krachmalnicoff, V. and De Wilde, Y., 2015. Mapping the radiative and the apparent nonradiative local density of states in the near field of a metallic nanoantenna. *ACS Photonics*, 2(2), pp.189-193.
- [142] Oubre, C. and Nordlander, P., 2004. Optical properties of metallodielectric nanostructures calculated using the finite difference time domain method. *The Journal of Physical Chemistry B*, 108(46), pp.17740-17747.
- [143] Devilez, A., Zambrana-Puyalto, X., Stout, B. and Bonod, N., 2015. Mimicking localized surface plasmons with dielectric particles. *Physical Review B*, 92(24), p.241412.
- [144] Duan, H., Hu, H., Kumar, K., Shen, Z. and Yang, J.K., 2011. Direct and reliable patterning of plasmonic nanostructures with sub-10-nm gaps. *ACS Nano*, 5(9), pp.7593-7600.
- [145] Kollmann, H., Piao, X., Esmann, M., Becker, S.F., Hou, D., Huynh, C., Kautschor, L.O., Bösker, G., Vieker, H., Beyer, A. and Götzhäuser, A., 2014. Toward plasmonics with nanometer precision: nonlinear optics of helium-ion milled gold nanoantennas. *Nano Letters*, 14(8), pp.4778-4784.
- [146] Wang, Y.M., Lu, L., Srinivasan, B.M., Asbahi, M., Zhang, Y.W. and Yang, J.K., 2015. High aspect ratio 10-nm-scale nanoaperture arrays with template-guided metal dewetting. *Scientific Reports*, 5, p.9654.
- [147] Flauraud, V., van Zanten, T.S., Mivelle, M., Manzo, C., García-Parajo, M.F. and Brugger, J., 2015. Large-scale arrays of bowtie nanoaperture antennas for nanoscale dynamics in living cell membranes. *Nano Letters*, 15(6), pp.4176-4182.

- [148] De Torres, J., Mivelle, M., Moparthi, S.B., Rigneault, H., Van Hulst, N.F., García-Parajo, M.F., Margeat, E. and Wenger, J., 2016. Plasmonic Nanoantennas Enable Forbidden Förster Dipole-Dipole Energy Transfer and Enhance the FRET Efficiency. *Nano Letters*, 16(10), pp.6222-6230.
- [149] Aouani, H., Wenger, J., Gérard, D., Rigneault, H., Devaux, E., Ebbesen, T.W., Mahdavi, F., Xu, T. and Blair, S., 2009. Crucial role of the adhesion layer on the plasmonic fluorescence enhancement. *ACS Nano*, 3(7), pp.2043-2048.
- [150] McPeak, K.M., Jayanti, S.V., Kress, S.J., Meyer, S., Iotti, S., Rossinelli, A. and Norris, D.J., 2015. Plasmonic films can easily be better: Rules and recipes. *ACS Photonics*, 2(3), pp.326-333.
- [151] Langguth, L. and Koenderink, A.F., 2014. Simple model for plasmon enhanced fluorescence correlation spectroscopy. *Optics Express*, 22(13), pp.15397-15409.
- [152] Kinkhabwala, A.A., Yu, Z., Fan, S. and Moerner, W.E., 2012. Fluorescence correlation spectroscopy at high concentrations using gold bowtie nanoantennas. *Chemical Physics*, 406, pp.3-8.
- [153] Brown, D.A. and London, E., 2000. Structure and function of sphingolipid- and cholesterol-rich membrane rafts. *Journal of Biological Chemistry*, 275(23), pp.17221-17224.
- [154] Lingwood, D. and Simons, K., 2010. Lipid rafts as a membrane-organizing principle. *Science*, 327(5961), pp.46-50.
- [155] Kusumi, A., Nakada, C., Ritchie, K., Murase, K., Suzuki, K., Murakoshi, H., Kasai, R.S., Kondo, J. and Fujiwara, T., 2005. Paradigm shift of the plasma membrane concept from the two-dimensional continuum fluid to the partitioned fluid: high-speed single-molecule tracking of membrane molecules. *Annu. Rev. Biophys. Biomol. Struct.*, 34, pp.351-378.
- [156] Gowrishankar, K., Ghosh, S., Saha, S., Rumamol, C., Mayor, S. and Rao, M., 2012. Active remodeling of cortical actin regulates spatiotemporal organization of cell surface molecules. *Cell*, 149(6), pp.1353-1367.
- [157] Sezgin, E., Levental, I., Mayor, S. and Eggeling, C., 2017. The mystery of membrane organization: composition, regulation and roles of lipid rafts. *Nat. Rev. Mol. Cell Biol.*, 18, pp.361-374.
- [158] Mayor, S. and Rao, M., 2004. Rafts: scaledependent, active lipid organization at the cell surface. *Traffic*, 5(4), pp.231-240.

- [159] Simons, K. and Gerl, M.J., 2010. Revitalizing membrane rafts: new tools and insights. *Nat. Rev. Mol. Cell Biol.*, 11(10), pp.688-699.
- [160] Pike, L.J., 2006. Rafts defined: a report on the Keystone Symposium on Lipid Rafts and Cell Function. *Journal of Lipid Research*, 47(7), pp.1597-1598.
- [161] Hancock, J.F., 2006. Lipid rafts: contentious only from simplistic standpoints. *Nature reviews. Molecular cell biology*, 7(6), p.456.
- [162] Lenne, P.F., Wawrezynieck, L., Conchonaud, F., Wurtz, O., Boned, A., Guo, X.J., Rigneault, H., He, H.T. and Marguet, D., 2006. Dynamic molecular confinement in the plasma membrane by microdomains and the cytoskeleton meshwork. *The EMBO Journal*, 25(14), pp.3245-3256.
- [163] Marguet, D., Lenne, P.F., Rigneault, H. and He, H.T., 2006. Dynamics in the plasma membrane: how to combine fluidity and order. *The EMBO journal*, 25(15), pp.3446-3457.
- [164] Wu, H.M., Lin, Y.H., Yen, T.C. and Hsieh, C.L., 2016. Nanoscopic substructures of raft-mimetic liquid-ordered membrane domains revealed by high-speed single-particle tracking. *Scientific Reports*, 6, p.20542.
- [165] van Zanten, T.S., Cambi, A., Koopman, M., Joosten, B., Figdor, C.G. and García-Parajo, M.F., 2009. Hotspots of GPI-anchored proteins and integrin nanoclusters function as nucleation sites for cell adhesion. *Proceedings of the National Academy of Sciences*, 106(44), pp.18557-18562.
- [166] van Zanten, T.S., Gómez, J., Manzo, C., Cambi, A., Buceta, J., Reigada, R. and García-Parajo, M.F., 2010. Direct mapping of nanoscale compositional connectivity on intact cell membranes. *Proceedings of the National Academy of Sciences*, 107(35), pp.15437-15442.
- [167] Meder, D., Moreno, M.J., Verkade, P., Vaz, W.L. and Simons, K., 2006. Phase coexistence and connectivity in the apical membrane of polarized epithelial cells. *Proceedings of the National Academy of Sciences of the United States of America*, 103(2), pp.329-334.
- [168] Dietrich, C., Yang, B., Fujiwara, T., Kusumi, A. and Jacobson, K., 2002. Relationship of lipid rafts to transient confinement zones detected by single particle tracking. *Biophysical Journal*, 82(1), pp.274-284.
- [169] Wawrezynieck, L., Rigneault, H., Marguet, D. and Lenne, P.F., 2005. Fluorescence correlation spectroscopy diffusion laws to probe the submicron cell membrane organization. *Biophysical Journal*, 89(6), pp.4029-4042.

- [170] Maiti, S., Haupts, U. and Webb, W.W., 1997. Fluorescence correlation spectroscopy: diagnostics for sparse molecules. *Proceedings of the National Academy of Sciences*, 94(22), pp.11753-11757.
- [171] Bacia, K., Kim, S.A. and Schwille, P., 2006. Fluorescence cross-correlation spectroscopy in living cells. *Nature Methods*, 3(2), p.83.
- [172] He, H.T. and Marguet, D., 2011. Detecting nanodomains in living cell membrane by fluorescence correlation spectroscopy. *Annual Review of Physical Chemistry*, 62, pp.417-436.
- [173] Kastrop, L., Blom, H., Eggeling, C. and Hell, S.W., 2005. Fluorescence fluctuation spectroscopy in subdiffraction focal volumes. *Physical Review Letters*, 94(17), p.178104.
- [174] Eggeling, C., Ringemann, C., Medda, R., Schwarzmann, G., Sandhoff, K., Polyakova, S., Belov, V.N., Hein, B., von Middendorff, C., Schönle, A. and Hell, S.W., 2009. Direct observation of the nanoscale dynamics of membrane lipids in a living cell. *Nature*, 457(7233), p.1159.
- [175] Mueller, V., Ringemann, C., Honigmann, A., Schwarzmann, G., Medda, R., Leutenegger, M., Polyakova, S., Belov, V.N., Hell, S.W. and Eggeling, C., 2011. STED nanoscopy reveals molecular details of cholesterol-and cytoskeleton-modulated lipid interactions in living cells. *Biophysical Journal*, 101(7), pp.1651-1660.
- [176] Honigmann, A., Mueller, V., Ta, H., Schoenle, A., Sezgin, E., Hell, S.W. and Eggeling, C., 2014. Scanning STED-FCS reveals spatiotemporal heterogeneity of lipid interaction in the plasma membrane of living cells. *Nature communications*, 5, p.5412.
- [177] Vicidomini, G., Ta, H., Honigmann, A., Mueller, V., Clausen, M.P., Waithe, D., Galiani, S., Sezgin, E., Diaspro, A., Hell, S.W. and Eggeling, C., 2015. STED-FLCS: an advanced tool to reveal spatiotemporal heterogeneity of molecular membrane dynamics. *Nano Letters*, 15(9), pp.5912-5918.
- [178] Edel, J.B., Wu, M., Baird, B. and Craighead, H.G., 2005. High spatial resolution observation of single-molecule dynamics in living cell membranes. *Biophysical Journal*, 88(6), pp.L43-L45.
- [179] Kelly, C.V., Baird, B.A. and Craighead, H.G., 2011. An array of planar apertures for near-field fluorescence correlation spectroscopy. *Biophysical Journal*, 100(7), pp.L34-L36.

- [180] Kelly, C.V., Wakefield, D.L., Holowka, D.A., Craighead, H.G. and Baird, B.A., 2014. Near-field fluorescence cross-correlation spectroscopy on planar membranes. *ACS Nano*, 8(7), pp.7392-7404.
- [181] Richards, C.I., Luong, K., Srinivasan, R., Turner, S.W., Dougherty, D.A., Korlach, J. and Lester, H.A., 2012. Live-cell imaging of single receptor composition using zero-mode waveguide nanostructures. *Nano Letters*, 12(7), pp.3690-3694.
- [182] Lohmüller, T., Iversen, L., Schmidt, M., Rhodes, C., Tu, H.L., Lin, W.C. and Groves, J.T., 2012. Single molecule tracking on supported membranes with arrays of optical nanoantennas. *Nano Letters*, 12(3), pp.1717-1721.
- [183] Ruprecht, V., Wieser, S., Marguet, D. and Schütz, G.J., 2011. Spot variation fluorescence correlation spectroscopy allows for superresolution chronoscopy of confinement times in membranes. *Biophysical Journal*, 100(11), pp.2839-2845.
- [184] Starr, T.E. and Thompson, N.L., 2001. Total internal reflection with fluorescence correlation spectroscopy: combined surface reaction and solution diffusion. *Biophysical Journal*, 80(3), pp.1575-1584.
- [185] Hassler, K., Anhut, T., Rigler, R., Gösch, M. and Lasser, T., 2005. High count rates with total internal reflection fluorescence correlation spectroscopy. *Biophysical Journal*, 88(1), pp.L01-L03.
- [186] Kapusta, P., 2010. Absolute diffusion coefficients: compilation of reference data for FCS calibration. *Application note*.
- [187] Kahya, N., Scherfeld, D., Bacia, K., Poolman, B. and Schwille, P., 2003. Probing lipid mobility of raft-exhibiting model membranes by fluorescence correlation spectroscopy. *Journal of Biological Chemistry*, 278(30), pp.28109-28115.
- [188] Zhang, K. and Yang, H., 2005. Photon-by-photon determination of emission bursts from diffusing single chromophores. *The Journal of Physical Chemistry B*, 109(46), pp.21930-21937.
- [189] Nicolau, D.V., Burrage, K., Parton, R.G. and Hancock, J.F., 2006. Identifying optimal lipid raft characteristics required to promote nanoscale protein-protein interactions on the plasma membrane. *Molecular and Cellular Biology*, 26(1), pp.313-323.
- [190] Spillane, K.M., Ortega-Arroyo, J., de Wit, G., Eggeling, C., Ewers, H., Wallace, M.I. and Kukura, P., 2014. High-speed single-particle tracking of GM1 in model membranes reveals anomalous diffusion due to interleaflet coupling and molecular pinning. *Nano Letters*, 14(9), pp.5390-5397.

- 
- [191] Spindler, S., Ehrig, J., König, K., Nowak, T., Piliarik, M., Stein, H.E., Taylor, R.W., Garanger, E., Lecommandoux, S., Alves, I.D. and Sandoghdar, V., 2016. Visualization of lipids and proteins at high spatial and temporal resolution *via* interferometric scattering (iSCAT) microscopy. *Journal of Physics D: Applied Physics*, 49, p.274002.